CHALMERS
UNIVERSITY OF TECHNOLOGY

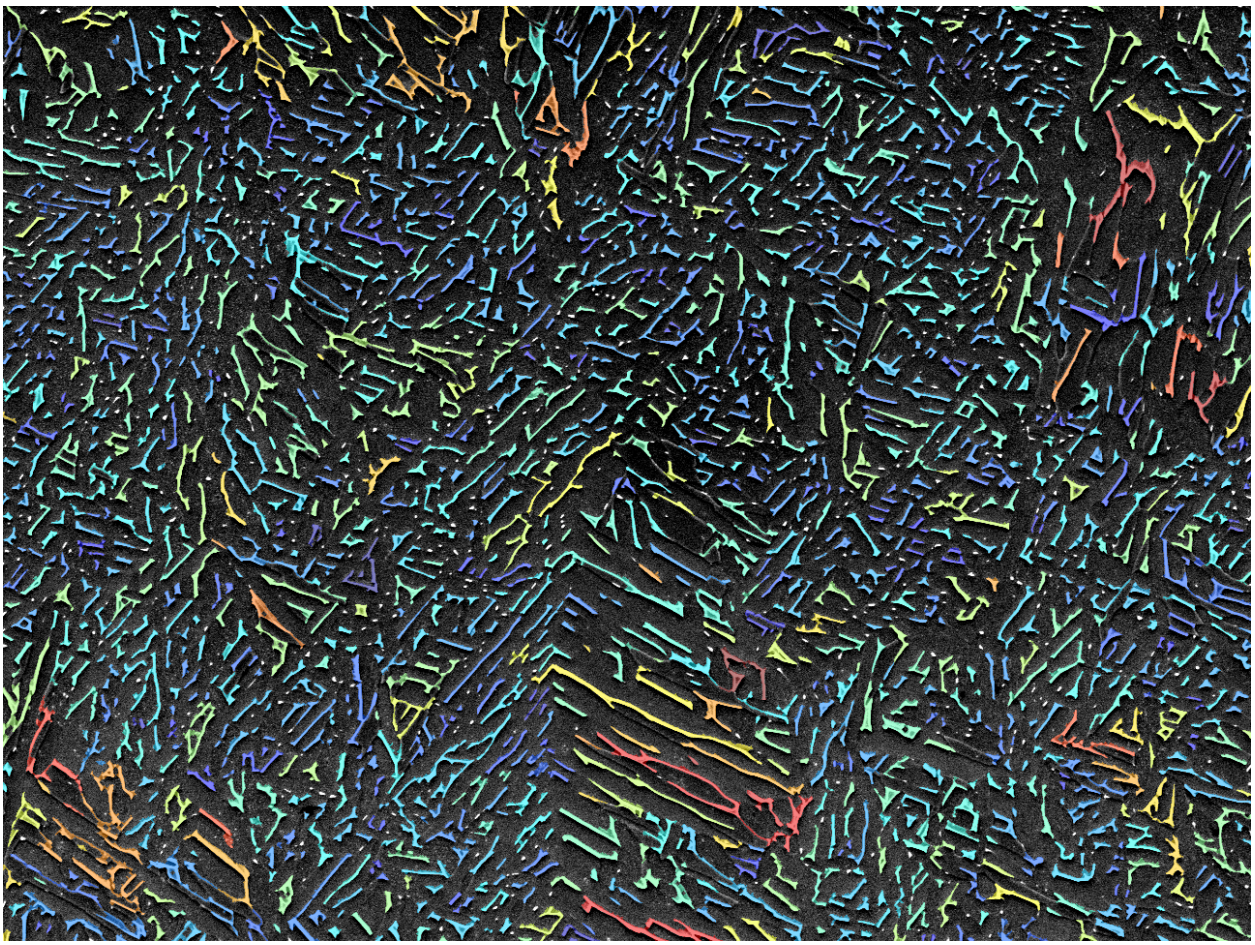

Microstructure Evolution of EBM Fabricated Ti-6Al-4V

Master's Thesis Work in Materials Engineering

SEBASTIAN DUDA

DEPARTMENT OF INDUSTRIAL AND MATERIALS SCIENCE

CHALMERS UNIVERSITY OF TECHNOLOGY
Gothenburg, Sweden 2020
www.chalmers.se

DEPARTMENT OF INDUSTRIAL
AND MATERIALS SCIENCE
CHALMERS UNIVERSITY OF TECHNOLOGY
Gothenburg, Sweden
www.chalmers.se

MASTER'S THESIS 2020

Microstructure Evolution of EBM Fabricated Ti-6Al-4V

SEBASTIAN DUDA

CHALMERS
UNIVERSITY OF TECHNOLOGY

Department of Industrial and Materials Science
CHALMERS UNIVERSITY OF TECHNOLOGY
Gothenburg, Sweden 2020

Microstructure Evolution of EBM Fabricated Ti-6Al-4V
SEBASTIAN DUDA

Supervisor/Examiner: Prof. Dr. Yu Cao, Department of Industrial and Materials Science, Chalmers University of Technology

Master's Thesis 2020
Department of Industrial and Materials Science
Chalmers University of Technology
SE-412 96 Gothenburg
Sweden
Telephone +46 31 772 1000

Cover: Scanning electron microscope image of EBM fabricated Ti-6Al-4V's microstructure processed by the image analysis software Mipar to define the β-phase (colored) and their distance to their nearest neighbors as measure of α-lamellae thickness (increasing spacing: blue → green →yellow →orange →red). The specimen was post-processed after the EBM process.

Gothenburg, Sweden 2020

Abstract

Electron beam melting (EBM) is an emerging additive manufacturing technology in the recent years, providing new opportunities for fast and sustainable production on industrial scale for key components in fields like the aerospace sector. Ti-6Al-4V offers outstanding mechanical properties, corrosion resistance and high temperature stability as well as low density. Hence, the EBM fabrication of Ti-6Al-4V components is of great interest for the aerospace industry. EBM is a complex thermal process and it is of tremendous significance to understand its effect on the microstructure and porosity of Ti-6Al-4V since they define the mechanical properties of the produced component.

This master thesis was executed in cooperation with GKN Aerospace, a company developing and supplying key components to the aerospace industry. The objective of this project was to understand how two different layer thicknesses in the printing and post-processing including hot isostatic pressing (HIP) and heat treatments (HT) affect the microstructure and porosity of EBM fabricated Ti-6Al-4V components. Furthermore, the effect of powder recycling on the powder's microstructure was investigated.

In this work optical and electron microscopy as well as energy dispersive X-ray spectroscopy (EDS) were used to identify the phases and morphologies in the microstructure of the components and the powders. Image analysis techniques were applied for quantitative analysis of the microstructure in terms of lamellae thicknesses and porosity. To support the results Vickers hardness measurements of the components were also conducted.

It has been found that all components featured an elongated prior β-grain structure parallel to the build direction with α-phase at the grain boundaries. The as-built sample with lower layer thicknesses possesses a slightly finer microstructure and post-processing makes it three times coarser. Finer microstructures resulted in higher hardnesses for every component due to the Hall-Petch effect. The microstructural features of the as-built samples at different layer thicknesses are similar but differ from the ones of the post-processed component. Besides the fully lamellar structure consisting of Widmannstetten α- and β-phase, martensite has been observed in the as-built state. A few additional features are detected in all specimen such as large feature-less regions consisting of α-phase. In all components the entire α-phase contains nano-sized particles which could be Ti_3Al precipitates. No correlation between porosity and layer thickness has been clarified. Post-processing reduces the porosity significantly, however, it does not close all pores. Furthermore, it has been found that the virgin Ti-6Al-4V powder has a fully martensitic structure whereas all the recycled ones exhibit a microstructure similar to that of the as-built samples, which almost does not change after ten times recycling.

Keywords: Additive manufacturing, electron beam melting, titanium alloy, Ti-6Al-4V, microstructure, porosity, hardness, hot isostatic pressing, powder recycling

Acknowledgements

First of all I would like to thank my supervisor and examiner Yu Cao that she gave me the great opportunity to work on this project. Moreover I'm thankful for her trust in me and that I was allowed to work very independently. However, when I needed advice she always spend time to help me. Also I want to thank my co-worker Hanna Karlsson for a good teamwork and lots of helpful discussions about questions we faced during our closely related work. Furthermore I'm thankful for the contribution of the company GKN Aerospace, especially Fredrik Kullenberg and Mats Delin, for providing the samples for this project and all their help during the meetings as well as via email contact. In addition I would like to thank Joakim Algardh from Arcam for all his help and lots of useful information. Along, I want to thank all the PhD students for their training and help in the lab. In the end I especially want to thank my family and all my friends for providing moral support in difficult times.

Content pages

List of Figures

List of Tables

1 Introduction

1.1 Background and problem description

The company GKN Aerospace who develops and supplies key components for the civil aerospace industry is planning to implement EBM-fabricated Ti-6Al-4V in different parts of jet engines such as the fitting for the outlet guide vanes (OGV's) located between the fan blades and the combustor. In aerospace applications the tolerances are very narrow and unpredicted failures must be avoided by all means.

Ti-6Al-4V is the ideal material to fulfill the challenging requirements in the aerospace sector for high performance parts like the OGV fittings. It exhibits outstanding properties such as low density, high strength even at elevated temperatures, high ductility, high fracture toughness as well as excellent corrosion resistance. However, Ti-6Al-4V has a low thermal conductivity and a strong tendency to undergo strain hardening making it a difficult-to-machine material by conventional methods. [1], [2]

A solution to manufacture these thin walled Ti-6Al-4V components is the relatively new Additive Manufacturing (AM) technique called Electron Beam Melting (EBM). AM techniques are currently an emerging technology and have gained more and more interest in the industry for the sustainable production of complex shaped components and the processing of difficult-to-machine materials. Especially in the aerospace and the biomedical sector the demand is continuously increasing due to its numerous advantages compared to conventional production methods, including short leading times, low material consumption, high design freedom, low tooling costs, less process steps and the production capability of near-net shape geometries. The new AM technique EBM opens even more opportunities by its advantages compared to the competing technique Selective Laser Melting (SLM). During an EBM process a sliced CAD model is printed layer-by-layer via melting of metallic powders by an electron beam in vacuum at high temperatures to achieve the final component. It can produce metallic components in significantly shorter processing time, having a higher energy efficiency and the capability to print reactive and stress prone materials. [3]–[5]

EBM is a complex thermal process which is not fully understood yet. Since the mechanical properties of a metal alloy component are determined by its microstructure, the influence of the EBM process on Ti-6Al-4V has to be investigated and well understood. It is known that strongly heterogeneous graded microstructures are established during EBM of Ti-6Al-4V. There is a lack of knowledge regarding how different EBM parameters like layer thicknesses affect the alloy's microstructure at specific sites within one component. Furthermore, one primary disadvantage of all AM manufactured components is a high degree of porosity which diminishes the mechanical performance of the component. The porosity is considered to be minimized by Hot Isostatic Pressing (HIP) after the EBM process. [4], [6]

For a better understanding of the EBM process, the microstructure, the porosity and the mechanical properties of as-built and post-processed EBM fabricated Ti-6Al-4V components have to be examined thoroughly to obtain an overview on how to predict and tune their performance.

1.2 Scope of the project

In this thesis three EBM fabricated Ti-6Al-4V components in shape of bars provided by GKN Aerospace are investigated. The focus was on the microstructure, porosity and the hardness. One of them is post-processed after the EBM fabrication and the other two are in the as-built state. The as-built components however differ in the layer thickness in each building step. The available characterization methods are optical microscopy (OM), scanning electron microscopy (SEM), energy dispersive X-ray spectroscopy (EDS), Vickers indentation (HV) and image analysis by means of the softwares Mipar and ImageJ.

The first question to be answered is which phases are formed and their morphologies in the microstructure. The second question is how the microstructure, porosity and hardness change within one component with increasing building height. To do so, samples taken from the components at the bottom, mid and top-section of the components were analyzed and compared. Then the third question is how the different processing histories of the three components affect the microstructure, porosity and hardness.
In the second part of this thesis four different Ti-6Al-4V powders are analyzed including fresh virgin powder and cycled powders exposed to the environment in the EBM chamber during a build for different number of times. The original plan was to analyze the semi-sintered structure of the cycled powders. Due to limited time and resources in the end the research question was adapted to how the microstructure and the porosity of the powders develop when they are exposed to the elevated EBM chamber temperatures.

2 Background/theory

2.1 Titanium and its alloys

Titanium is a transition metal element of group IVB in the periodic table having the atomic number of 22 and a melting point of 1668 °C [7]. It is the ninth most frequent element on earth and the forth frequent structural material in the Earth's crust after aluminum, iron and magnesium. Since the 20th century, when the first titanium alloys have been developed, their demand as well as the relevant research are continuously increasing. Nowadays, as one of the most advanced materials, they have a wide variety of applications due to their numerous advantages. Pure titanium has a tensile strength of 241 MPa [7], which is comparatively lower with respect to steels, however by proper alloying, which will be further addressed in section 2.1.1, titanium can have the same strength as steel while exhibiting a low density of 4.51 g/cm³[7], as illustrated in Figure 1a. This density is only 60% of the ones for steel leading to a high strength to weight ratio even at elevated temperatures as shown in Figure 1b. [7]–[10]

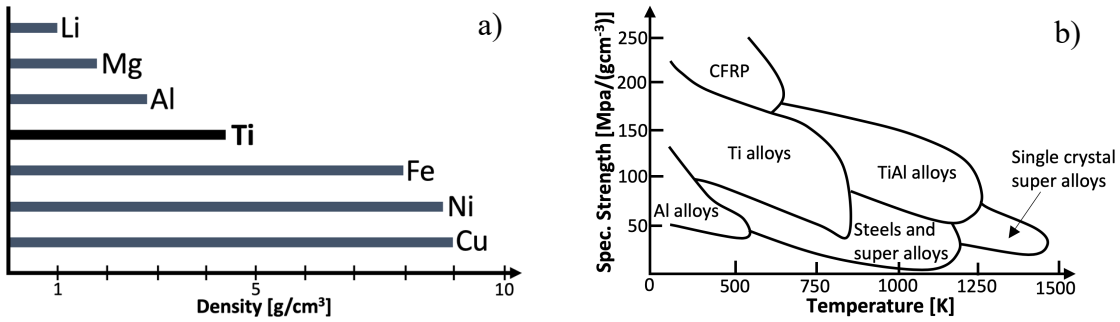

Figure 1: a) Density of titanium compared to other metals; b) specific strength of different kinds of alloys versus the temperature. Adapted from [8].

Beside the low density and the high temperature strength, titanium alloys also possess high ductility, outstanding corrosion resistance because of a protective oxide layer formed at the surface as well as high biocompatibility. Their applications range from jet engines and air frames in aerospace over human bone implants up to the chemical industry. [7]–[10]

2.1.1 Phase stabilization and alloy classification

Titanium has two allotropic modifications, which is the β-phase at high temperatures and the α-phase at low temperatures. The transition temperature, also called "transus", for pure titanium is 882.5 °C [10]. Because both the allotropic modifications can be stabilized by proper alloying, a large possible variety of alloys can be obtained. Different types of stabilization are depicted schematically in Figure 2.

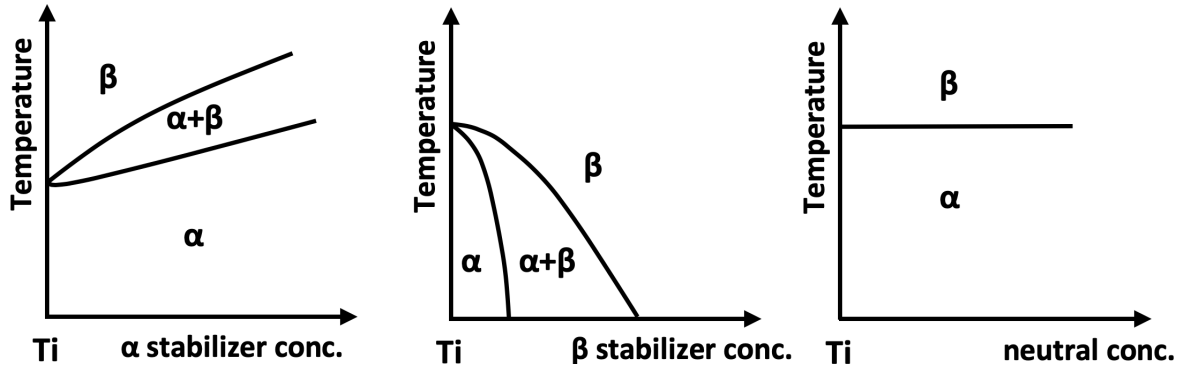

Figure 2: Schematically stabilization of the allotropic modifications of titanium. Inspired from [10].

Two different types of stabilizers exist for titanium. α-stabilizers (e.g. Al, O, N or C) increase the transus with increasing concentration to stabilize the α-phase at temperatures above 882.5 °C [10]. β-stabilizers (e.g. V, Mo, Fe or Nb) stabilize the β-phase at temperatures below the transus, making the β-phase stable possibly even at room temperature. Besides stabilization, the stabilizer elements also act as solid solution strengtheners for the respective parent phase. [7]–[10]

Depending on the type of Ti-phases present in the alloy and the volume fraction of each phase, the properties of the respective alloy may change significantly. Hence it is important to explicitly distinguish between the different kinds of alloys.

Table 1: Comparison of general properties for the three different kinds of titanium alloys. [8]

	α-alloys	**α+β-alloys**	**β-alloys**
Density	Low	Low	High
Strength	Low	High	Very high
Ductility	Medium	High	Medium
Fracture toughness	High	Medium	Medium
Creep strength	High	Medium	Low
Corrosion resistance	Very high	High	Medium
Oxidation resistance	Very high	Medium	Low
Weldability	High	Medium	Low
Cold formability	Very low	Low	Medium

As depicted in Table 1, titanium alloys are divided into three different categories, namely α-alloys, β-alloys and α+β-alloys. In α-alloys like Ti-5Al-2.5Sn, the α-phase is the most predominant phase. In β-alloys like Ti-11.5Mo-6Zr-4.5Sn, the β-phase is the most predominant one. α+β-alloys like Ti-6Al-4V consist of both of α- and β-phase and each phase is stabilized by their respective stabilizer. α+β-alloys are the most commonly used titanium alloys owing to the combination of high strength and ductility while still having a low density. In Table 1 the general properties of the main types of alloys are compared to each other.

2.1.2 Ti-6Al-4V

50 % of all used α+β-alloys are Ti-6Al-4V and it is the most intensively developed material among all types of titanium alloys. It contains 6 wt% aluminum as α-stabilizer and 4 wt% vanadium as β-stabilizer. The mechanical properties of Ti-6Al-4V can vary significantly by choosing different processing routes or subsequent heat treatments. Some typical mechanical properties are listed in Table 2 together with their variation. [7], [8]

Table 2: Characteristic values for mechanical properties of Ti-6Al-4V. [8]

Hardness	**Young's modulus**	**Yield strength**	**Tensile Strength**	**Elongation**	**Fracture toughness**
300-400 HV	110-140 GPa	800-1100 MPa	900-1200 MPa	13-16 %	33-110 $MPam^{1/2}$

As already stated in 2.1, titanium alloys can maintain their strength even at high temperatures. However the strength of Ti-6Al-4V is clearly decreasing at approximately 700 °C and at 1000 °C the yield strength is only 10 MPa according to a study in [11].
Despite of the numerous advantages in mechanical properties, Ti-6Al-4V also has several drawbacks. It has a poor thermal conductivity of 7 $Wm^{-1}K^{-1}$ at room temperature [12] and a strong tendency to undergo strain hardening. Hence it is difficult to machine using conventional machining methods such as forging, casting or rolling. During the mentioned operations an excessive amount of material is wasted which is neither environmentally nor economically friendly since titanium is very expensive. One promising alternative way to produce this titanium alloy with less waste material is AM such as EBM. [8], [9], [13]

2.1.3 Allotropic modifications and phase transformations

As explained earlier, titanium has two allotropic modifications. At temperatures below 882.5 °C [10] for pure titanium and 994°C [14] for Ti-6Al-4V, it crystallizes as α-phase with a hexagonal closed packed (hcp) crystal structure. For temperatures above the transus, it crystallizes as β-phase with a body centered cubic (bcc) structure. The unit cells of both phases are shown in Figure 3 and a schematic phase diagram of Ti-6Al-4V is illustrated in Figure 4.

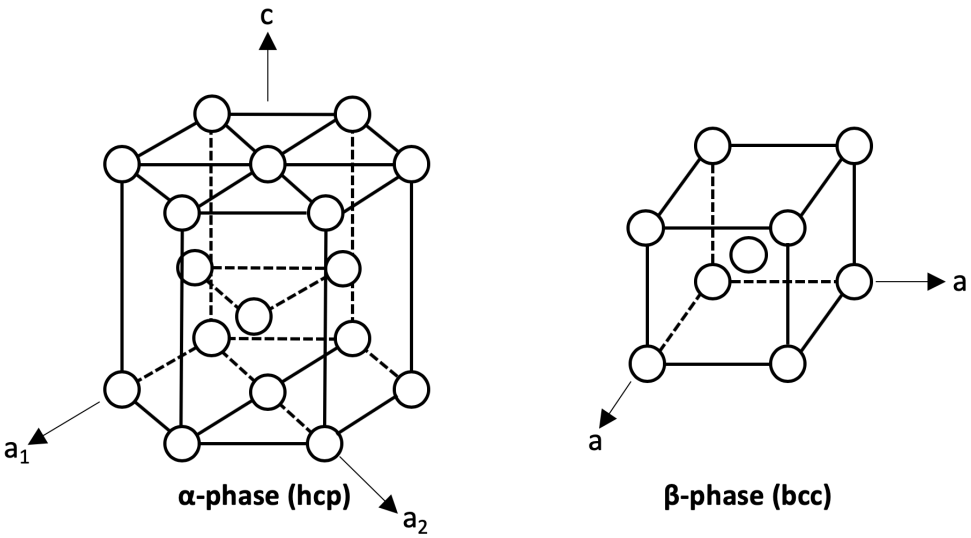

Figure 3: Allotropic modifications of titanium and their unit cells. Inspired from [10].

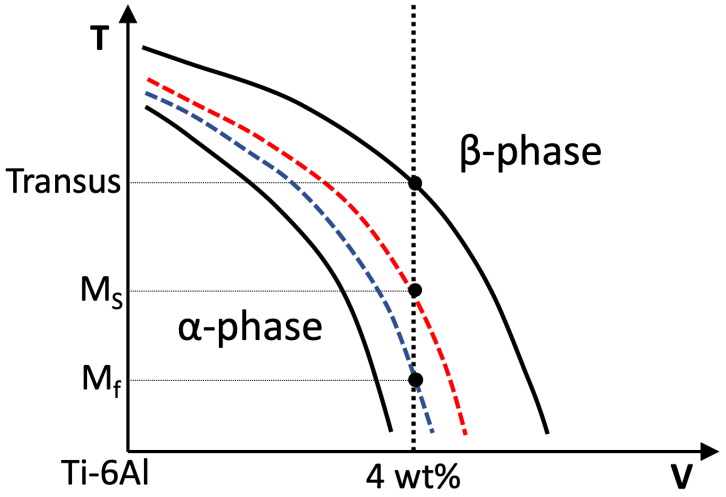

Figure 4: Schematic phase diagram of Ti-6Al-4V. Adapted from [15].

During cooling of the β-phase below the transus with cooling rates smaller than 20°C/s, it is conveyed into the α-phase by transforming the bcc closed packed planes {110} into the hcp basal planes {0001} by a diffusion process, where the vanadium diffusion is the rate-limiting step. Thereby, the lattice parameters change from $a_{bcc} = 0.332$ nm to $a_{hcp} = 0.295$ nm and $c_{hcp} = 0.468$ nm. However, interstitially dissolved atoms like oxygen or substitutional atoms like aluminum might change the lattice parameters to some extent. An orientation-relationship, also called Burgers-relationship, for the slip planes as well as slip directions for hcp and bcc is the key point for the transformation mentioned above and is defined as following: [2],[4],[16]

$$\{110\}_\beta // \{0001\}_\alpha$$
$$\langle 111\rangle_\beta // \langle 1120\rangle_\alpha$$

This relationship dictates that the bcc crystal will be transformed into one of 12 hexagonal variants regarding orientation with respect to the former bcc crystal. The number 12 arises from six slip planes and two slip directions on each slip plane in bcc crystals. The hcp phase grown by following this Burgers-relationship relationship is inclined by angles of $n \times 30°$ with respect to each other, where n is a natural number. [2],[4],[17]

During the phase transformation the α-phase preferentially nucleates at the β-grain boundaries and grows diffusion controlled along these specific planes into the β-grain whereby the β-phase is consumed. Since Ti-6Al-4V is an α-β-alloy, a certain volume fraction of β-phase remains below the transus which is illustrated as two phase region in the schematic phase diagram in Figure 4. Hence the transformation is designated as $\beta \rightarrow \alpha + \beta$. The resulting lamellar structure is called Widmanstätten structure and the alloying elements exhibit a significant partitioning behavior after this phase transformation. The α-stabilizer preferably diffuses into the α-phase, whereas the β-stabilizer diffuses into the β-phase. Different types of microstructures resulting from this diffusional controlled phase transformation will be perpetuated in 2.1.4. [8], [10], [14], [18]

When the β-phase is cooled below the transus with higher cooling rates exceeding the critical value determined by the amount and type of alloying elements, the time is insufficient for the diffusion controlled $\beta \rightarrow \alpha + \beta$ transformation. Instead, α'-martensite is nucleated by a diffusion-less cooperative movement and shear type process of atoms designated as $\beta \rightarrow \alpha'$ as soon as the temperature is fallen below the martensite start temperature M_S. M_S depends on the cooling rate and can range from 575 °C to 800°C [9] for Ti-6Al-4V. The critical cooling rate to produce a fully martensitic structure is 410 °C/s. However, when the cooling rate is between 410 °C/s and 20°C/s, martensite is partially formed whereas its volume fraction is decreased with decreasing cooling rate. Similar to the α-phase, the α'-martensite crystallizes in the hcp structure following the Burgers-relationship for orientation. During the martensitic transformation dislocations and twins are induced into the lattice. Since the martensite is developed by a diffusion-less transformation from the β-phase, it exhibits the same chemical composition as the parent β-phase. Hence compared to the α-phase it is enriched in vanadium. [6], [14], [15], [19]

The martensitic phase is thermodynamically metastable, hence it can be decomposed during heating. In this case, fine α-crystals are heterogeneously nucleated at the martensite boundaries or at internal features like twins. Since the martensite compared to the α-phase is enriched in vanadium, these excess V atoms are released during the nucleation and growth of new α-crystals, leading to the formation of β-crystals at the α-phase boundary. The decomposition of α'-martensite is therefore designated as $\alpha' \rightarrow \alpha + \beta$ which is a diffusion-controlled process. For a full decomposition the tempering must be done at temperatures above 800 °C [20]. The holding time for a full decomposition is strongly dependent on temperature as well as the size of the specimen. [20]–[22]

Besides the diffusion-controlled transformation and the martensitic transformation a third type of transformation, named massive transformation is possible when the cooling rate is between 410 °C/s and 20 °C/s or when the temperature is between the transus and M_S. The mechanism is a short-range atomic movement through the parent-product interface. The resulting phase is then called "massive martensite" or α_m, which has the same chemical composition and crystal structure as the α'-martensite. However, this type of transformation is not intensively studied for Ti-6Al-4V. [14], [23], [24]

According to the Ti-Al phase diagram in Appendix 1, nanometer sized Ti_3Al particles can be precipitated densely and homogeneously within the α-phase, when the alloy is aged at temperatures slightly below the solvus for Ti_3Al at 550°C.[10], [25]

2.1.4 Influence of heat treatments and processing parameters on the microstructure

The microstructure can be modified by adjusting the temperatures, holding times as well as the cooling rates of the heat treatment. To understand the influence of different heat treatment parameters on the microstructure, it is helpful to first highlight how the microstructures are typically produced in Ti-6Al-4V. There are two different main types of microstructures namely fully lamellar structure and bi-modal structure.

The fully lamellar microstructure consists of an α-phase layer at the grain boundary of the prior β-grains and a lamellar structure of α-and β-phase inside the grains. To achieve this microstructure, first a homogenization treatment is done above the transus to form pure β-grains. Afterwards the alloy is cooled down from above the transus where α-nuclei are crystallizing at the grain boundaries of the β-crystal and then growing diffusion-controlled into the β-grains following the Burger's relationship. A third step might be added for stress relieving and precipitation hardening at elevated temperatures, typically at 545 °C [26], by precipitating Ti_3Al particles. When the aging is done at temperatures above the solvus, no Ti_3Al precipitates are formed and only stress relieve is accomplished. [8], [10], [25], [27], [28]

The second type of microstructures is the bi-modal microstructure. It consists of equiaxed α-grains embedded in a lamellar $\alpha+\beta$ matrix which is generally finer than a fully lamellar structure. To generate the bi-modal microstructure the first step is a homogenization treatment above the transus to establish the pure β-phase. During the subsequent cooling the α-phase nucleates and grows to a grain boundary layer and a lamellar structure. Subsequently the alloy is deformed plastically to induce a large number of dislocations into the lattice. Now the temperature is increased again but is kept below the transus to initiate recrystallization. The necessary recrystallization temperature T_R is not a fixed value and strongly depends on several factors. Increasing recrystallization times and increasing degrees of deformation decrease T_R. However, as an approximate guidance for metal alloys generally half the melting temperature T_m in Kelvin is taken as T_R, which would be $T_R \approx 966.5$ K or 693.4 °C for Ti-6Al-4V since its T_m is 1933 K [29]. Normally the recrystallization is done at above 800 °C. During the recrystallization, both new α- and β-crystals nucleate and grow to equiaxed grains whereas the α-phase is nucleated at β-grain boundaries. The new recrystallized grains do not follow the Burgers-relationship. Afterwards, when the alloy is cooled again, new α-lamellae are formed within the recrystallized β-grains and the bi-modal microstructure is formed. In the end, an aging step might be added for precipitation hardening or to remove possible residual stresses generated by fast cooling rates. [8], [10], [25], [28], [30]

The first microstructural parameter which can be manipulated is the grain size. When the heat treatment temperature above the transus is set high, for example during homogenization, the β-grains grow and become larger. The same effect is achieved by longer holding times at these temperatures. [10]

The morphology of α-phase can be modified by varying the cooling rate which changes nucleation rate and diffusion time. High cooling rates increase the driving force for nucleation but lower the available time for the thermal activated diffusion. When the cooling rate is low, the alpha lamellae grow from the grain boundary into the grain until they meet other lamellae, forming a colony structure. Each lamella has the same orientation within that colony. However, if the cooling rate is increased, the α-phase can also nucleate directly inside the β-grains and a basket-weave structure is formed in which the orientation of α-lamellae differ from that of the surrounding ones. Hence, the lamellae can grow independently in one of twelve possible directions and the microstructure consists of numerous fine lamellae over all possible orientations. In this case, the lamellae grow into each other and a finer structure of entangled lamellae is formed. The colony and the basket-weave structure are illustrated in Figure 5. [10], [18], [27], [31]

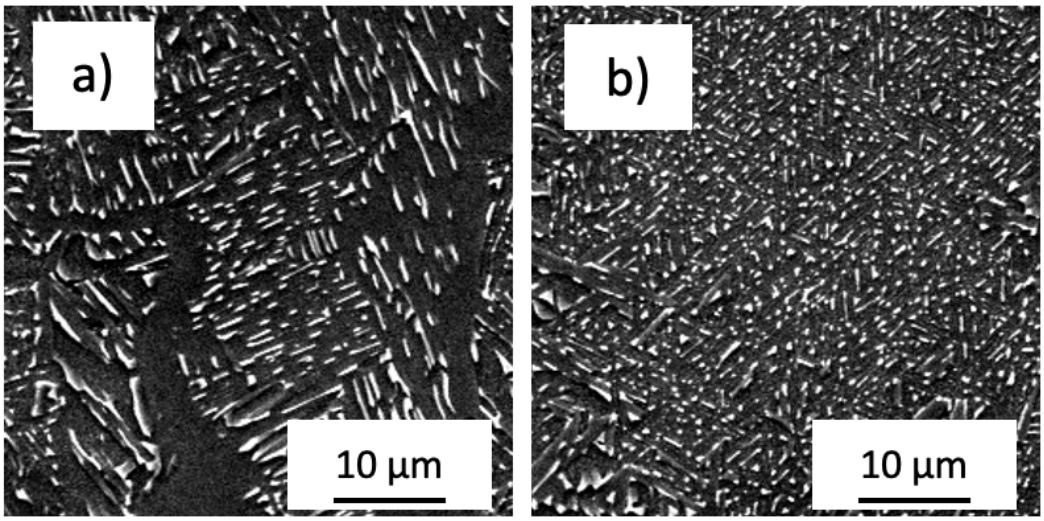

Figure 5: SEM images of a) colony and b) basket-wave structures in Ti-6Al-4V.

If the cooling rate is further increased, instead of a lamellar structure a martensitic one is established in Ti-6Al-4V in the form of thin needles following the Burger's-relationship. It is called "acicular martensite" as shown in Figure 6. In fully martensitic structures, neither the α- nor the β-phase is present. [4], [19]

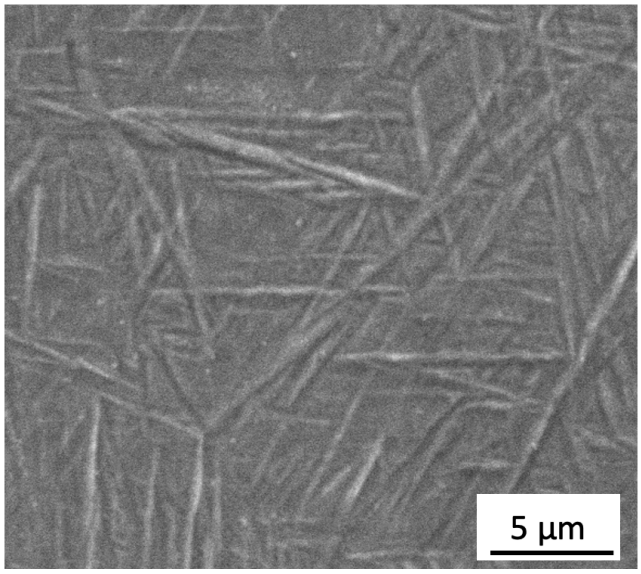

Figure 6: SEM image of acicular martensite in Ti-6Al-4V.

One special α-phase morphology is yielded at very low cooling rates when cooling from temperatures close to the transus. It is referred to be globular α caused by very low nucleation rates. Another possible reason to form this morphology is a long holding time at elevated temperatures near the transus. However, same as the massive martensite, this phase is sparsely reported in literature for Ti-6Al-4V. [28],[32]

Another microstructural parameter strongly dependent on the heat treatment is the feature size. Below the transus, the α-lamellae and the grain boundary α can grow further with increasing temperatures. This is a diffusion-controlled process which is thermally activated. Hence, during aging or post-processing at elevated temperatures the microstructure can be coarsened, the extent of which is increased by higher temperatures and longer holding times. Furthermore, the α-lamellae and the α-grain boundary layer become finer with increasing cooling rates during the cooling from temperatures above the transition temperature. This can be explained by higher nucleation rates and less time for diffusion with increasing cooling rate. [8], [10], [21], [33], [25]

During heating, martensite can be decomposed into α- and β-phase, the size can be directly controlled by the chosen temperature and holding time. The higher the temperature, the less α-nuclei are formed at the phase boundary and in turn less β-nuclei. Both phases can grow to a larger extend before they meet each other. The growth is then stopped and a coarser microstructure is generated. Also, a longer holding time makes the newly formed α-lamellae coarser. Still, the microstructure of decomposed martensite is generally finer than the ones composed of the α-and β-phase formed by cooling from above the transus. [21],[34]

The last microstructural parameters affected by the heat treatment are the number and the size of the Ti_3Al precipitates. Both increase with prolonged aging. According to Carreon et al. [26] the measured area fraction of Ti_3Al in α-phase was 10.45 % for 1 h and

17.22 % for 576 h. The size of the precipitates is approximately in the range of 50 – 200 nm [26]. With increasing size the shape of the precipitates becomes ellipsoidal. [26], [35]

2.1.5 Correlation between microstructure and mechanical properties

The microstructure determines the mechanical properties of metals and alloys. One of the most important parameters is the slip length of dislocations. A decreased slip length increases both strength and ductility due to the Hall-Petch effect. Small lamellae thicknesses and grain sizes mean a reduced slip length. Comparing both Widmanstetten structures, the basket-wave structure is in general finer than the colony structure, leading to smaller slip length and consequently higher strength and ductility. [8], [10], [25] The α'-martensite needles are strong obstacles for dislocations, hence they also decrease the slip length of dislocations. Furthermore, there is a high dislocation density around martensite which leads to dislocation strengthening. The martensitic phase also contains elastic strains due to a distorted crystal structure caused by the vanadium atoms in a hcp structure. Consequently, the strength of the material increases with increasing volume fraction of martensite, giving a stronger material than a pure lamellar structure with same feature size as the martensitic one. However, the elastic strains decrease the ductility, leading to a lower ductility of the material with increasing martensite volume fraction. [6], [36] Furthermore the material can also be strengthened by aging. In Ti-6Al-4V the Ti_3Al precipitates are coherent with the matrix and hence are sheared by dislocations. The shearing of particles requires a higher stress than the normal dislocation glide through the crystal lattice, hence the precipitation of Ti_3Al further increases the strength of the material. [10]

Another mechanical property affected by the microstructure is the high cycle fatigue (HCF) strength which is defined as the resistance to crack nucleation. The low cycle fatigue (LCF) strength also stands for resistance to crack nucleation and additionally for resistance to microcrack propagation. Resistance to crack nucleation is determined by dislocation motion and hence given by the yield strength. The microcrack propagation is hindered by obstacles like lamellae, colony boundaries or grain boundaries. Hence both HCF and LCF strength are increased by finer microstructures. [8], [10], [25]

Fracture toughness is defined as the critical stress intensity factor which leads to rapid uncontrolled crack propagation. It is also related to the microstructure. The fracture toughness is increased by rougher crack front profiles since they lead to a stronger crack deflection proportional to the size of the crack obstacles. In addition, the resistance to macrocrack propagation is affected by the microstructure which is also increased by increasing lamellae thicknesses for same reasons as the fracture toughness.[8], [10], [25]

Equiaxed microstructures have a higher strength, ductility and LCF-strength due to their finer microstructure as the result of recrystallization. However, the HCF-strength is lower compared to the lamellar structure because the α-lamellae formed during the second cooling have a lower concentration of α-stabiliser elements which results in a weaker

phase compared to the lamellae in the fully lamellar structure or the equiaxed alpha in the bi-modal ones. The less strengthened lamellae then act as crack nucleation sites. Also, the fracture toughness and resistance to macrocracks are lowered because of the finer microstructure. [8], [10]

2.2 Electron Beam Melting (EBM)

2.2.1 Working principle

Electron beam melting (EBM) or also called selective electron beam melting (SEBM) is an additive manufacturing method in which a metallic 3D-component is built by melting fine powder particles, which are typically pre-alloyed, layer-by-layer via an electron beam. The layer thicknesses range from 50 to 200 µm [10]. An EBM machine consists of two main parts as illustrated in Figure 7. One is the electron beam gun chamber, which has the same working principle as a scanning electron microscope and uses a tungsten filament with beam powers between 50 and 3500 W [37]. The gun allows scan speeds of at least 1000 m/s [10] and beam spot sizes between 200 and 1000 µm [10]. When the accelerated electrons hit on the powder particles they transfer their kinetic energy as heat into the powder particles. Another main part is the building chamber which is maintained at temperatures between 400 and 750 °C [10] and a high-vacuum between 10^{-4} and 10^{-5} mbar [10]. The vacuum is important to avoid electrons hitting on gas molecules and to prevent chemical reactions between sample and gas. Furthermore the building chamber contains the rake, the powder hopper and the building table made of stainless steel. Their functions are explained below. [10], [38]

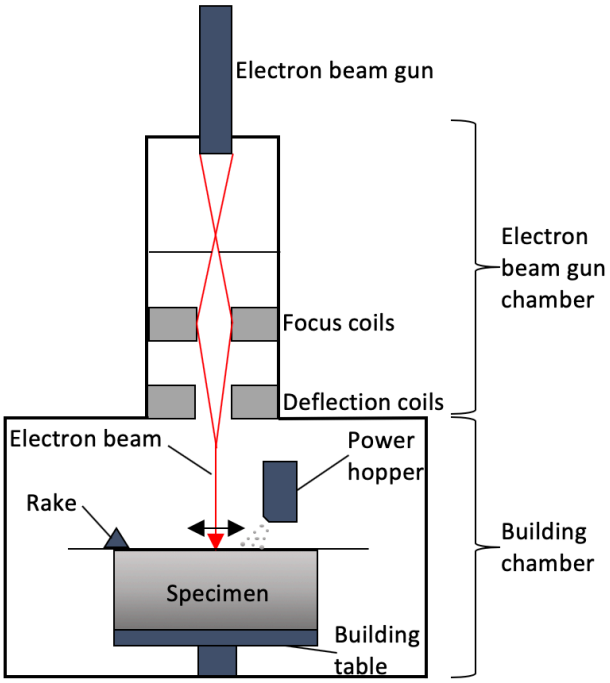

Figure 7: Schematic drawing of an EBM system. Inspired from [38].

The manufacturing process has the following steps: First, a CAD model of the to be printed component is loaded into the EBM software which then slices the 3D-model into numerous thin layers. In the next step, the first layer of powder particles with the

predetermined thickness is given via the powder hopper on the top of a building table by horizontal movement. The rake then smoothens the layer's surface. Subsequently, specific areas of the layer directed by the sliced CAD model are semi-sintered to reduce temperature gradients during the process which would otherwise induce stresses and cracks into the material. This is done by selectively scanning a defocused electron beam with low beam power over the respective area. After this step the semi-sintered area is melted by a focused electron beam with higher power to produce a melt pool which is then solidified to one dense layer. The melting step is subdivided into contour melting and hatch melting. In the former one the outer shape of the to be printed component in this slice is established and in the second step the region inside the layer is built. Next, the building table is lowered and the whole procedure is repeated layer-by-layer until the component is finished. [37]–[39] In the end of the process, the non-molten powder surrounding the component is recycled by a particle recovery system (PRS) which includes blasting, vacuum cleaning and sieving. The recycled powder is then mixed with new powder which then is filled into the powder hopper for the next build. [5]

It is of importance to know the temperature distribution inside the building chamber since the material's microstructure will be affected by its thermal history. However, the temperature distribution in the chamber is very complex and not fully understood yet. The highest temperature is kept in the melt zone generated by the electron beam which is the only heat source in the chamber. The temperature then decreases with increasing distance from the melt pool because a high vacuum in the chamber prevents heat convection. [6], [31]

In addition, the temperature and the cooling rate are not constant within the build. There are three ways of heat transfer during the cooling. One of the main heat dissipations is the heat conduction through the building table at the bottom of the component. The second one is the heat loss through the unmolten powder particles surrounding the to be-printed part. The third heat loss is the heat radiation from the surface of the component. It can be concluded that the cooling rate decreases with increasing building height, because the building table is made of massive stainless steel and hence has a clearly higher thermal conductivity than the highly porous semi-sintered Ti-6Al-4V powder. [6], [31], [40], [41]

2.2.2 Post-processing

Despite its numerous advantages like freedom of design, high material's utilization, high energy efficiency, printing capability of reactive and stress prone materials as well as high build rates, the EBM also has some drawbacks. Similar to other AM methods, the as-built components have a bad surface finish and a high degree of porosity. Both types of defects lower the fatigue performance significantly since they act as crack nucleation sites due to stress concentrations. Also, the porosity considerably lowers the strength and ductility of the component. Different types of porosity will be further discussed in 2.2.3. [4], [9] Post-processing techniques are therefore necessary to minimize these kinds of defects. The surface can be smoothened by surface machining like grinding or honing. The porosity

can be removed by densifying the material via hot isostatic pressing (HIP), which is generally conducted for EBM fabricated components. [9]

During the HIP-process the workpiece is exposed to high temperatures at certain isostatic pressures, typically 920°C and 100 MPa [42] for titanium alloys. A HIP unit mainly consits of a furnace and a gas inlet connected to a compressor. The furnace is heated up and the gas, typically helium or argon is then transferred in the furnace and is acting onto the workpiece's surface by collisions from all directions at once causing the isostatic pressure. [42], [43] The idea behind this technique is to combine the high temperature and high pressure to accelerate the diffusion in the material. The driving force is the reduction of surface energy. The pores with additional surface area will be closed by this activated diffusion. It has been reported in [6] that porosity and pore size indeed are reduced by HIP, but not completely healed. [6], [42]

2.2.3 EBM fabricated microstructures

EBM is a complex thermal process which generates graded microstructures with high degree of heterogeneity in terms of phase morphology and size. The microstructures are strongly dependent on the processing parameters of the EBM process, the post-treatment as well as the size and shape of the component. [31], [40]

The melting of the thin layers produces a small melt pool with temperatures between 1900 °C and 2700 °C [6]. The subsequent cooling in the fabrication chamber causes solidification of the material. The exact cooling rate in this step is not known but it is estimated to be in the range of 10^3 and 10^5 °C/s [6] depending on the melt pool size. During the entire process the build is exposed to the elevated temperatures in the building chamber. Hence, the closer a region is to the building table, the longer the exposure time. Also, when a new powder layer on the top of the component is melted, the already solidified layers below are partially re-melted. It has been estimated by Arcam that three layers below the top one are re-melted. The un-melted part will be heated again by heat transfer from the melt pool into the surrounding region. After printing, the entire component is slowly cooled down to room temperature. Further post-processing by HIP and/or heat treatments expose the component to elevated temperatures again. In addition, stresses are applied to the component by the high pressures. [4], [31], [40]

The previously mentioned complex thermal process certainly affect the microstructures. Large columnar grains with an approximate width of several hundred microns and a length of several millimeters are generally reported, which can be explained as follows. During the melting of the top powder layer by the electron beam, the grains in the layers below are partially re-melted. These grains then act as nuclei for epitaxial grain growth of β-grains parallel to build direction. [6], [22] During the subsequent rapid cooling β is transformed into α'-martensite. The high temperatures in the fabrication chamber and the heat transfer from the melted layers above is then considered to cause the decomposition of the α'-martensite into the thermodynamically stable lamellar structure

of $\alpha + \beta$. As soon as the lamellar structure is formed, it is coarsened due to the high temperatures in the chamber. Depending on the processing parameters some α'-martensite might be left which was stated in several previous studies like in [33], [44], [45]. Especially at the very top layer of the component martensite is expected since it does not experience re-heating from the melt above and furthermore it has the shortest exposure to the chamber temperature compared to the rest of the build. [6], [22], [40]

As explained in 2.2.2, typical defects in EBM fabricated components are pores. There are three different types of porosity observed in the as-built structure. The first one is called lack of fusion which is visible as elongated pore with a length of several hundred microns [40] perpendicular to the build direction. It arises when the beam power is not sufficient to melt all powder particles in one layer either because of lack of beam power, too high scan speeds or too large powder particles. The second type is called gas pore which can be distinguished by its spherical shape and reduced size compared to the lack of fusion. The size is typically between 10 and 50 µm [40]. It also arises during the EBM process and can have two origins. First, it could be some residual porosity from the powder layers when distributed by the hopper and the rake. In general, the packing density is reduced by lower powder flowability due to several reasons such as less spherical particles or too large particle size differences. Second, dissolved residual gases from the fabrication chamber in the melt are released during solidification owing to the decreased solubility in solid compared to the liquid. The third type of pores is also called gas pore, but it has a size of only a few microns and is generated by entrapment of argon in the powder particles during their manufacturing process. All types of pores are presented in Figure 47. [6], [33], [40], [46]

2.3 Principle of some characterization techniques

2.3.1 Scanning electron microscope (SEM)

The scanning electron microscope (SEM) scans a focused electron beam over a sample's surface. A detector system measures the signals produced from the interaction of the electron beam and the sample atoms. The buildup of an SEM and all its components is well known and schematics can be found in literature. [48], [49]

The working principle of an SEM is as follows: Electrons emitted from a cathode, either a thermoionic or a Schottky field emission gun (FEG), called primary electrons (PE), are accelerated towards an anode by voltages E_0 of 0.1 keV up to 50 keV [47]. The first type of source is a tungsten filament which is heated by a current until its electrons gain sufficient energy to overcome the potential barrier and leave the filament's atoms into the vacuum. The second type of source is made of a single crystalline tungsten needle coated with a layer of ZrO_2. When an electrostatic field is applied on the tip, the field lines are densified with decreasing tip radius and at the very end of the tip the energy is high enough for the electrons to leave the tip's atoms into the vacuum. The electron emission is further assisted by heating the tip. Compared to thermoionic guns, the electron beam

of FEGs has a higher coherency and optical brightness leading to a higher resolution. [47], [49], [50]

The generated electron beam of the SEM is then focused to a more parallel one by a set of condenser lenses, which are rotationally symmetric electromagnets. Afterwards the beam passes the objective lens which focuses the beam to a narrow point for scanning the surface of the sample. Also, on its way through the beam column, the beam passes several apertures allowing further reduction of the beam diameter. At the end of the column deflection coils are placed. They consist of wires where applied currents repulse the PE leading to tilt or shift of the focused beam for selectively scanning on the sample's surface in the x-y-plane. The distance between the sample in focus and the lowest part of the beam column is called working distance (WD). To avoid electrons hitting gas molecules the entire microscope is under high vacuum. [49]–[51]

When the PE hit the sample, several interactions in different depths can occur causing characteristic signals. An illustration of beam-sample interactions is presented in [49]. The signals of interest for imaging the sample are the backscattered electrons (BSE) and secondary electrons (SE). The characteristic X-rays and the X-ray continuum, known as "Bremsstrahlung", are further discussed in 2.3.2. [49]

When the PE hit on the sample's surface, its atoms are ionized and loosely bound electrons which are called SE can escape. Since they only have a relatively low kinetic energy, only those close to the sample's surface at a maximum depth of a few nanometers can exit. An SE-detector then collects the SE and transfers them into an electrical signal, the intensity of which is recorded to generate an image. SE-images give topographical information of the sample and features at higher z-coordinates appear brighter. [49], [51]

The BSE are generated by a different process. When striking the sample, PE can be scattered by its atoms and are deflected multiple times. PE escaped from the sample are termed as BSE. They have a higher kinetic energy, making penetration depths larger than that of the SE. The higher the atomic number of the sample's atoms, the more PE are backscattered, and hence more BSE are detected by an BSE-detector. In this way a compositional contrast is created and brighter areas indicate more heavier elements. Besides the compositional contrast, a weak topographical contrast is also created. The resolution of BSE-images is lower compared to SE-images due to the larger interaction volume. [49], [51]

An SEM image can provide depending on the detection mode topographical, compositional and morphological information of the sample's surface at resolutions up to 1 nm [47]. The choice of optimum parameters is important for the best possible images and must be considered for every circumstance. Large E_0 means large interaction volume which reduces resolution but it also generates a high beam current leading to a high contrast and high signal to noise ratio. A smaller beam diameter is achieved by lowering

the aperture sizes and allows higher spatial resolutions, however this also decreases the beam current which then consequently reduces the contrast. [51]

2.3.2 Energy-dispersive X-ray spectroscopy (EDS)

The energy-dispersive X-ray spectroscopy (EDS) is an analytical method used in electron microscopes to analyze the chemical composition of the sample. When the electron beam of the SEM hits the sample, X-rays are emitted when inelastic electron-electron interaction occurs. There are two different types of X-rays which were already mentioned in 2.3.1. The Bremsstrahlung arises from a deceleration of PE by the negative charge cloud of the sample's electrons. Since a loss of velocity means a loss of kinetic energy, the PE emit the lost energy E as X-rays according to Equation 1 [52], where h is the Planck's constant, c the speed of light and λ the wavelength of the X-ray. [51], [52]

$$E = h * \frac{c}{\lambda} \tag{1}$$

The energy of the Bremsstrahlung is strongly dependent on the deceleration of the electron and has no specific value for respective elements. Hence it can't be used for EDS-analysis. On the other hand, when PE strike an atom, a bound electron can be ejected from the inner shell of the atom, leaving a core hole. The characteristic X-rays arise according to equation (1) when an outer shell electron fills this hole. It is "characteristic" to each element. The innermost shell of an atom is the K shell followed by the L, M, N and O shell. The characteristic X-rays produced due to an electron transition from the L into the K shell is designated as K_α, a transition from the M into the K shell as K_β and so on. The characteristic energies for a few selected elements are listed in Appendix 3 . An energy sensitive X-ray detector, like a Si(Li) semiconductor detector is located inside the vacuum chamber of the SEM. It records all the incoming X-rays and then creates a typical EDS-spectrum where number of counts are plotted over the energy and the characteristic peaks for each transition are visible as exemplarily shown in Figure 8. [51]–[53]

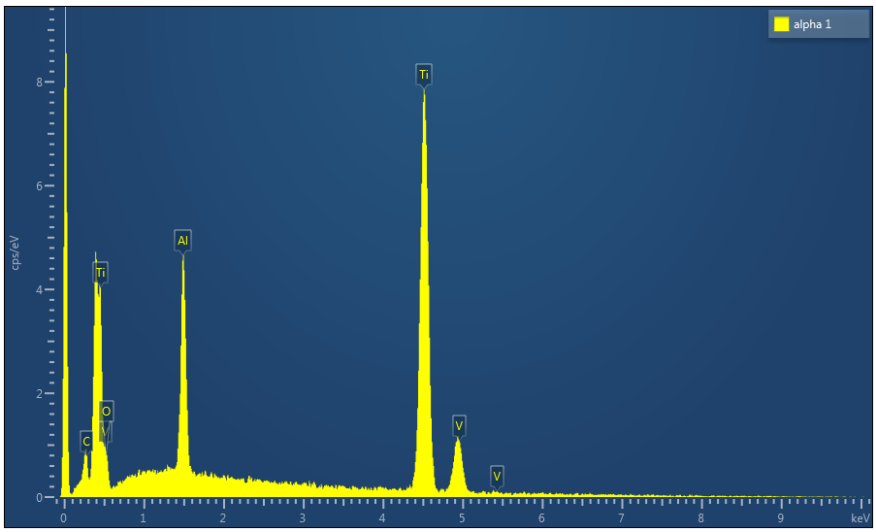

Figure 8: EDS spectrum for Ti-6Al-4V.

By subtracting the background caused by the Bremsstrahlung from the spectrum, peak fitting, peak-integration and the so called "ZAF correction" the fraction of the corresponding elements at the location where the PE hit is calculated. The ZAF correction is necessary to acquire the real composition from the measured one by consideration of several physical effects arising from different types of atoms which influence the spectrum. "Z" stands for the atomic number, "A" for the effect of absorption of X-rays and "F" for the change in X-ray fluorescence. [34], [51]

Same as for the SEM, the selection of the optimum parameters is crucial and must be considered depending on the specific investigation. The most important parameter is the acceleration voltage E_0 of the PE since the energy must be high enough to cover all the critical energies E_c for generation of the characteristic X-rays of all elements in the specimen. A general rule is to select an E_0 of at least double the E_c of the energetically highest characteristic X-ray of interest to ensure the excitation because the PE can lose their energy partially as Bremsstrahlung. However, the interaction volume increases with increasing E_0. Hence if smaller features in the specimen need to be analyzed, E_0 should be set as low as possible. Thus, the final selection of the most suitable E_0 for a microstructural analyzation is about compromising between an interaction volume as low as possible but still guarantying the generation of all the characteristic X-rays of interest. [34], [51]

2.3.3 Vickers hardness (HV)

The hardness of a material is a measure of resistance to local plastic deformation and hence directly proportional to its strength. Typically, an indenter with well-known standardized geometry is pressed with a certain force on the sample's surface along its normal direction for a specified time. Afterwards the area of the very top section of the indentation obtained on the sample's surface is measured using an optical method. The hardness is then defined as the ratio between the force and the measured area. [54]

The Vickers hardness test is one widely used technique which is defined by the ASTM Standard E92-72. A highly polished square-based pyramidal diamond indenter with an angle α of 136 ° between its faces is used. Such an indenter and the produced indentation is schematically shown in Figure 9.

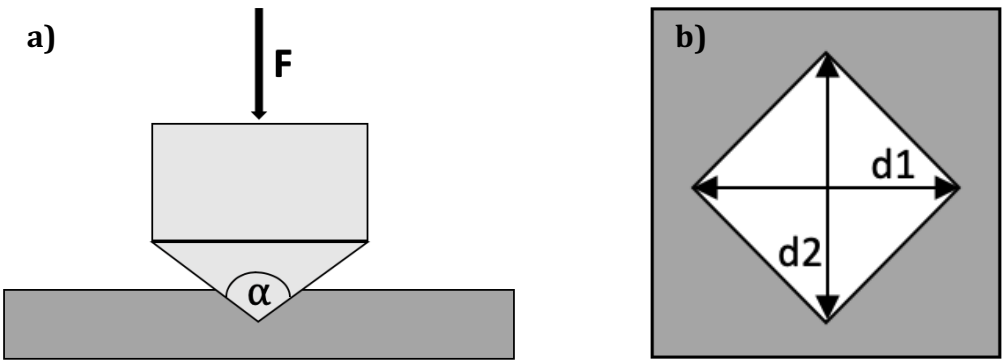

Figure 9: Vickers hardness measurement according to ASTM Standard E92-72 with indenter in a) and indentation in b). Inspired from [57].

The applied force can vary from 0.098 N to 980.7 N. The test is referred to be a micro hardness test if the force is not larger than 0.980 N while it is a macro hardness test if the force is larger than 0.980 N. Vickers hardness (HV) is calculated from the applied force F [N] and the arithmetic average of the indentations diameters d [mm] by Equation 2.

$$HV = 0.1891 * \frac{F}{d^2} \quad (2)$$

The used force is generally indicated in the Vickers hardness. For example, when a force of 98.07 N, equivalent to a load of 10 kg, is chosen the hardness is called HV 10.

3 Methodology

3.1 Sample specification

3.1.1 EBM fabricated components

The three different EBM fabricated Ti-6Al-4V bars named A3K1, A3bK1 and A3bK85 were provided by GKN Aerospace. The powder used for the builds is Arcam ELI (extra low interstitials) Ti-6Al-4V powder produced by plasma atomization with particle sizes from 45 to 106 µm and the composition given in Table 3.

Table 3: Chemical composition of the used Arcam ELI Ti-6Al-4V powder.

Element	Al	V	C	Fe	O	N	H	Y	Ti
Wt%	6.31	4.17	0.01	0.16	0.11	0.01	0.002	<0.001	Bal.

The components A3bK1 and A3bK85 were built by the Arcam EBM Q20plus machine using a 90 µm layer thickness. The component A3K1 was built with the same machine but the Arcam EBM Q10plus theme was used having a layer thickness of 50 µm. In both themes an algorithm tried to achieve a surface temperature of approximately 650 °C on the very top powder layer. The temperature inside the chamber is heterogeneous distributed as explained in 2.2.1 and is decreasing with distance from the currently melted area. Only one thermocouple was placed in the building chamber next to the building table and the measured temperatures were between 400 and 500 °C for both themes.

The components A3K1 and A3bK1 are in the as-built state, meaning no further processing after printing. The component A3bK85 was post-processed by HIP for 2h with a pressure of 100 MPa at 920 °C under an inert atmosphere. Subsequently the component was undertaken a two-step heat treatment (HT) in vacuum, first at 704 °C for 2h followed by 4h at 538 °C. The major differences between the components are summarized in Table 4.

Table 4: Major differences between the specimen A3K1, A3bK1 and A3bK85.

Component	Layer thickness [µm]	State
A3K1	50	as-built
A3bK1	90	as-built
A3bK85	90	HIP+HT

3.1.2 Powders

Besides those components, GKN Aerospace provided a bag of new and unrecycled Arcam ELI Ti-6Al-4V powder which was called “virgin”-powder. Additionally, 10 cubes marked as A13C1, A14C1, …., A22C1 were supplied. These cubes were produced by quick contour melting in an EBM machine having a thin wall and a hollow core. Inside the cubes virgin powder was entrapped. These cubes were then placed inside a EBM machine on the building table next to the to-be-printed component and experienced the high

temperatures in the building chamber for the entire duration of the build. The duration of one complete build is referred to be one cycling. The specification “A13” means the powder was cycled once, “A14” cycled twice and so on until “A22” which was cycled 10 times.

3.2 Sample preparation

3.2.1 EBM fabricated components

To analyze the components with the dimension of 180 mm × 15 mm × 15mm, polished samples had to be prepared. To do so, first they were cut by the Struers Discotom-2 machine with a 10S25 SiC cutting wheel and water as lubricant/coolant. All the cuts were made following the same scheme as illustrated in Figure 10. Three samples were extracted from each component and the analyzed surfaces were parallel to the building direction as indicated by the bold dashed lines.

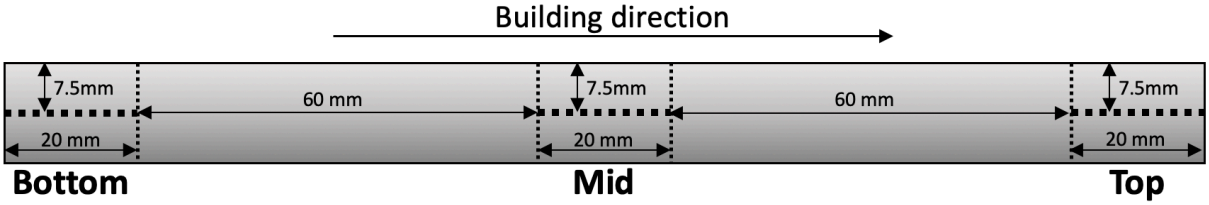

Figure 10: Schematic of a component with the corresponding cuts as dashed lines.

In the next step, the sample was grinded by the Struers LaboPol-21 with a #220 SiC grinding paper and water as lubricant/coolant until defects from the cutting, like burs have been removed. The samples were then mounted in electrically conductive Polyfast powder (Bakelite resin mixed with carbon) by the Struers CitoPress-20. The Struers TegraPol-31 was then used for the next three surface preparation steps. The first one was for plain grinding (PG) followed by a fine grinding (FG) and the last step was the polishing (OP). The respective processing parameters are listed in Table 5.

Table 5: Parameters for plane grinding (PG), fine grinding (FG) and polishing (OP) of bars.

Step	**PG**	**FG**	**OP**
Surface	MD Piano	MD Largo	MD Chem
Abrasive type, size	Diamond, #220	Diamond, 9 µm	Collodial Silica, 0.04 µm
Suspension/Lubricant	Water	DiaPro Allegro/Largo 9	90% OP-S+ 10% H_2O_2 (30%)
Rpm	300	150	150
Force [N]	25	20	30
Time [min]	8	10	10

After polishing, the samples were rinsed in isopropanol (IPA) inside an ultrasonic bath for 15 min to remove all silica particles. For microstructural investigations the samples

were then etched with Kroll's reagent (H_2O + 3% HNO_3 + 1-2 % HF) by speckling wetted cotton for 20 s onto the surface.

3.2.2 Powders

First, the cubes A13C1, A17C1, A22C1 were opened by the Buehler Isomet 11-1180 Low Speed Saw with a diamond blade without lubricant/coolant. Then the powder particles were scratched out with a spatula from the center of the cubes. Subsequently the powders from the cubes as well as the virgin powder from the bag were mounted into Polyfast by the Struers CitoPress-20. To do so, some Polyfast powder was first crushed to finer particles by a mortar and then mixed with powder before mounting. Afterwards the Struers TegraPol-31 was used for PG, FG and OP. The procedure was similar to the one specified in Table 5. Only the times and forces were changed to 2 min and 20 N for FG and 20 N and 8 min for FG, respectively. The time and force for OP (10 min and 30 N) were remained the same. After these steps the samples were cleaned and etched similarly as the components.

3.3 Characterization methods

3.3.1 Microstructural analysis

In this work a Zeiss Axio Imager.M2m optical microscope (OM) operated by the Zeiss Zen Core 2.5 software was used for low magnification images of the samples to study the grain structures.
For microstructural analysis two different SEMs were used. The first one was a Philips XL30 environmental SEM (ESEM) with a tungsten filament as electron source. It was controlled by the FEI Microscope Control software. An acceleration voltage of 12 keV, an aperture size of "5" and an Everhart Thornley (ET) SE-detector were chosen for all the images. For high magnification images a Zeiss-LEO 1550 Gemini Schottky field emission gun SEM (FEGSEM) was utilized. The software for operating the FEGSEM was the Zeiss SmartSEM software. An acceleration voltage of 15 keV, an aperture size of "1" and an Inlens detector were chosen for SE-images.
All images from the OM, ESEM as well as FEGSEM in this work were taken in a way that the build direction is pointing from the bottom to the top, hence it not further specified in later images.
For qualitative compositional analysis of different features EDS measurements were conducted in the FEGSEM with an Oxford X-mas EDS-detector, an acceleration voltage of 10 keV, an aperture size of "5"and a fixed working distance of 8.5 mm. The images for the measurement were taken by a Centaurus BSE-detector and point analysis was done using the Oxford Instruments-Aztec software to obtain compositional information.

3.3.2 Quantitative microstructural analysis

The quantitative microstructural analysis was performed by taking 15 images with the ESEM for every sample following the pattern shown in Figure 11. A magnification of 1000× was chosen for the A3bK85 samples and 2500× for the ones of A3K1 and A3bK1. Two different parameters were measured, α-lamellae thickness and phase fraction of α and β.

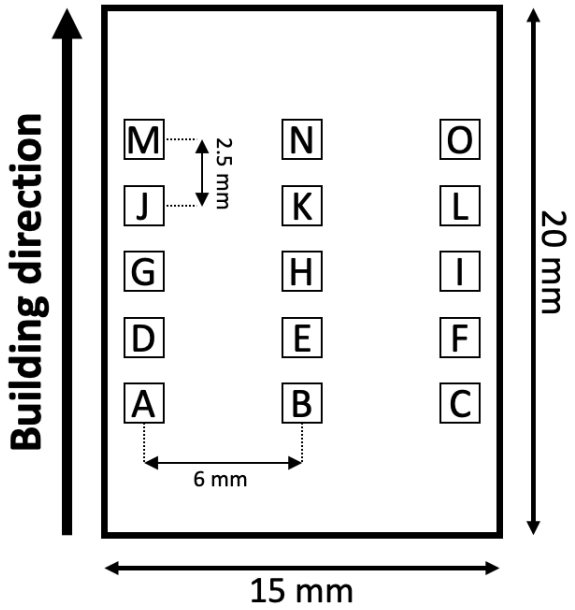

Figure 11: Image location on the samples surface (A to O) for quantitative analysis.

To determine the α-lamellae thickness, the images were analyzed by the Mipar software following steps below: A) The scale (microns/pixel) is set by help of the scale bar from the ESEM. B) The image is cropped to remove the annotation bar. C) A non-local means filter is applied to remove the background of electron microscope images. D) The image is inverted and a basic threshold of 110 is executed to define the β-phase. E) The phase is first dilated and then eroded to smoothen the α-β-interface. F) Features smaller than 10 square pixel are excluded since they are due to blurry SE-contrast or background which was still present to some extent. G) All edge features were removed. An example for the result of this algorithm is depicted in Appendix 4. H) After the beta was defined, the function "measure nearest neighbor distance" was applied to measure the distance of every β-phase in the respective image to its nearest neighbor. This is defined as the α-lamellae thickness. The algorithm was applied on all 15 images of each sample and were then combined in one data set representative for the lamellae thicknesses in this sample.

The second parameter, the phase fraction of α and β, was analyzed by the ImageJ software. First, the annotation bar was removed by the "region of interest" function. Afterwards the "Otsu-threshold" was applied to distinguish between these two phases by an automatically set threshold. One example of a thresholded image is given in Appendix 5. The phase fraction was then obtained by measuring the area of the phase above and below this threshold. The procedure was applied on all 15 images of each sample. The average value was then taken as the phase fraction of the respective specimen.

3.3.3 Porosity measurement

For the investigation of the porosity the polished and unetched samples were analyzed by the OM at 50× magnification. Each sample was mapped by the stitching-function of the Zeiss software allowing one image of the entire specimen. A rectangular region of interest excluding the edges of every specimen was set to avoid the additional measurement of surface roughness. The reason is the software cannot distinguish the pores and surface roughness due to the same color contrast. The image was then evaluated by means of the ImageJ software by binarization using a constant threshold limit of 150. Afterwards the area fraction of all regions above that threshold were determined to obtain the porosity of the sample. In the next step the particle analysis plugin was utilized to examine the pore sizes in the samples. Because the program was only able to measure the area A of each pore, the diameter d was then calculated by $d = 2\sqrt{A/\pi}$ assuming the pores are circular. Also, a lower threshold of 8 µm for the pore diameter was set and anything smaller than this was considered as insufficiently accurate to be measured by the system.

3.3.4 Vickers hardness measurement

The hardness measurements in this work were performed by means of the Struers DuraScan-70 G5 hardness tester using a 10 kg load, with holding time of 15 s and a 20× objective to examine the indentations. Polished and unetched samples were used. The indentation diameter was automatically measured by the Ecos Workflow software. For each sample a pattern of 8 × 8 indentations was placed on the sample's surface as illustrated in Figure 12. The arithmetic average of the 64 hardness values was then referred to be the Vickers hardness of the respective sample.

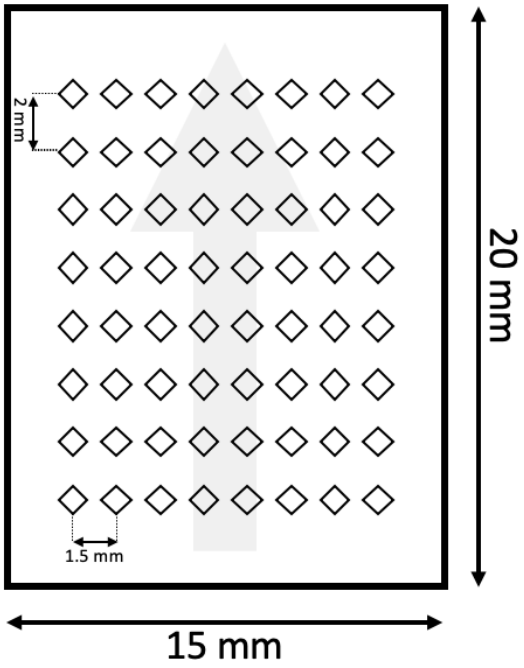

Figure 12: Indentation location for the Vickers hardness measurements.

4 Results and Discussion

4.1 EBM fabricated Components

4.1.1 Microstructure

4.1.1.1 Grain structure

Figure 13 shows OM images of the grain structure of the three different bars parallel to building direction at 25× magnification. The grains can be either identified by different color from the neighboring grains or by a thin white layer located at the grain boundaries. All of them are elongated and parallel to the build direction all over the build height. The grain boundaries are not perfectly straight, instead they are rather wavy. The grains are several millimeters long and have widths ranging from 30 to 240 μm. No equiaxed grains or significant differences in grain size between the as-built samples and the post-processed one were observed.

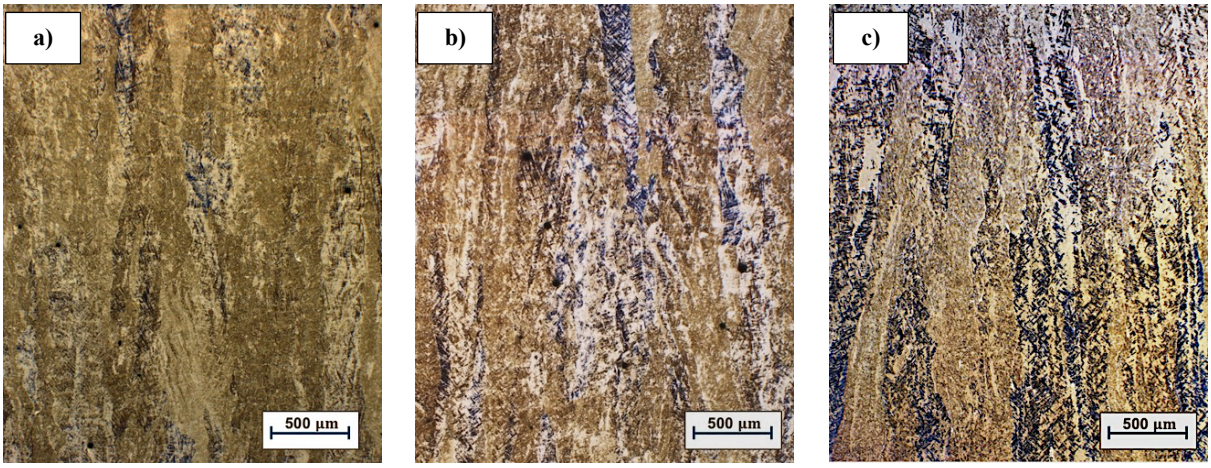

Figure 13: OM images of grain structure for a) A3K1(50μm;as-built), b) A3bK1(90μm;as-built) and c) A3bK85(90μm; post-processed).

The characteristic shape of the grains and their orientation are expected since the elongated grains are formed by epitaxial growth along the building direction during the EBM process when cooling the melt below the melting point of 1660 °C. Also, when the temperature is kept below the transus of 994 °C the grain boundary α layer hinders any grain boundary motion which would otherwise lead to a change in grain size as well as shape. Above the transus, this layer is depleted and the grains would grow. The maximum temperature of post-processing was 920 °C, which is 74 °C lower than the transus. Hence the size and shape of the epitaxial grown grains remained the same after post-processing.

4.1.1.2 Microstructure of A3K1 (50μm; as-built)

An overview of the microstructure from the A3K1 is given by the ESEM image in Figure 14. Very fine and heterogeneous microstructures with several different features in terms of contrast, size and morphology are observed. The heterogeneities arise from the thermally complex EBM process where the microstructure is exposed to different temperatures with changed cooling rates for several times. The heterogeneities could also be established from powder particles with varying size and microstructure if they are for some reason not entirely melted by the electron beam. The bright phase in the image is

the β-phase whereas the dark one is the α-phase. Also, sharp needles are visible, which could be acicular martensite. There was no significant difference observed in microstructural features between the samples from the bottom, mid and top section.

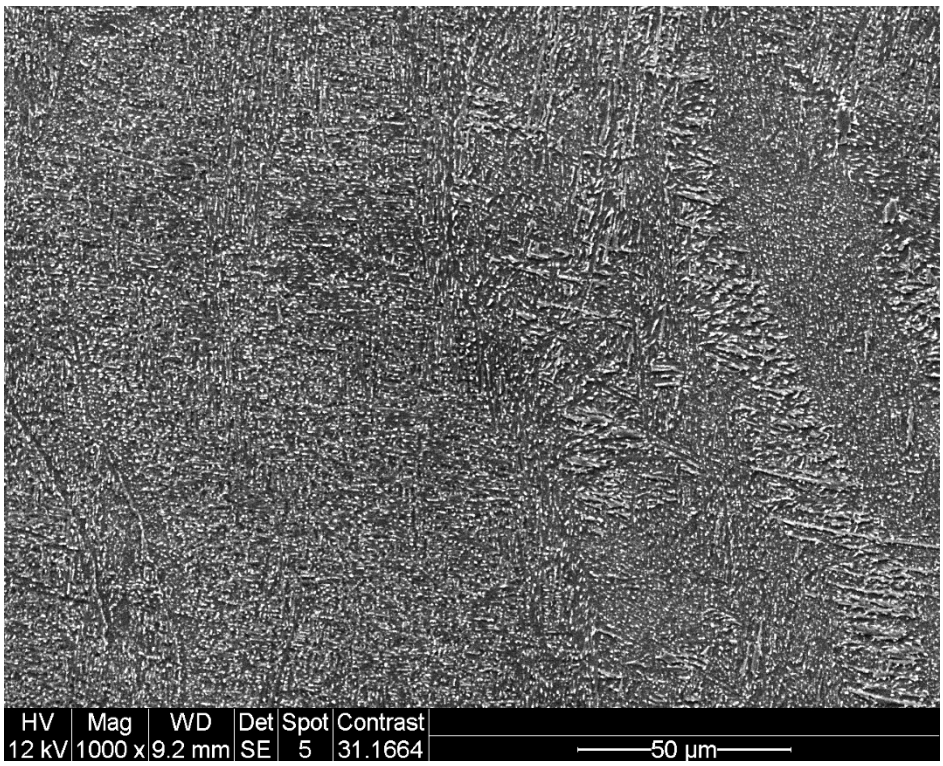

Figure 14: ESEM image as overview microstructure of A3K1.

The feature size in this structure is too small for any EDS point analysis even at the smallest acceleration voltage of 10 keV, which is necessary to generate the vanadium K_α-peak, as listed in Appendix 3. An exemplarily EDS point analysis of the alloy's main elements for both the α- and β-phases is given in Table 6.

Table 6: Average EDS results for the α- and β-phase in A3K1.

	Aluminum [wt%]	**Titanium [wt%]**	**Vanadium [wt%]**
α-phase	6.20 ± 0.32	89.86 ± 1.45	3.94 ± 1.52
β-phase	5.90 ± 0.54	90.49 ± 0.79	3.61 ± 1.29

It is known that α-phase should be enriched in aluminum and β-phase in vanadium. However, the measurement gives the nominal alloy composition of 6wt% aluminum and 4 wt% vanadium for both phases. This means the lateral resolution of the EDX analysis is too low to separate these two phases. Besides point analysis, mapping and line scans were also conducted which were not able to distinguish between the different phases neither.

Furthermore, it is difficult to estimate the phase fraction of α and β due to the presence of the third needle shaped phase which has a varying contrast. These two phases can only be clearly distinguished by its shape. Several other image analysis techniques using different softwares were tried to measure the phase fraction which were not successful neither. However, the most promising one seemed to be the "Trainable Weka

Segmentation" in ImageJ. In the following section the phase morphologies are discussed in more detail.

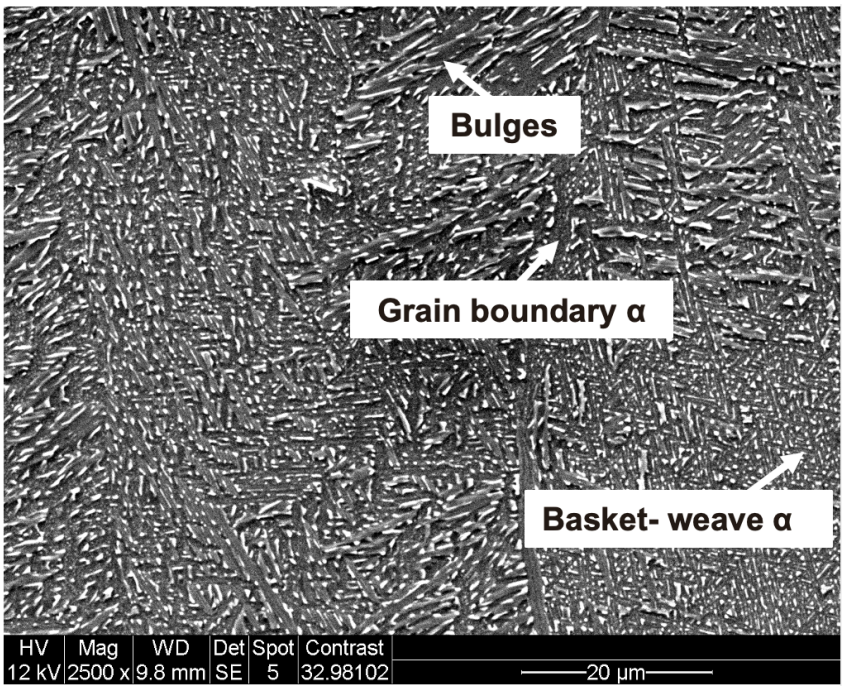

Figure 15: ESEM image of different microstructural features in A3K1.

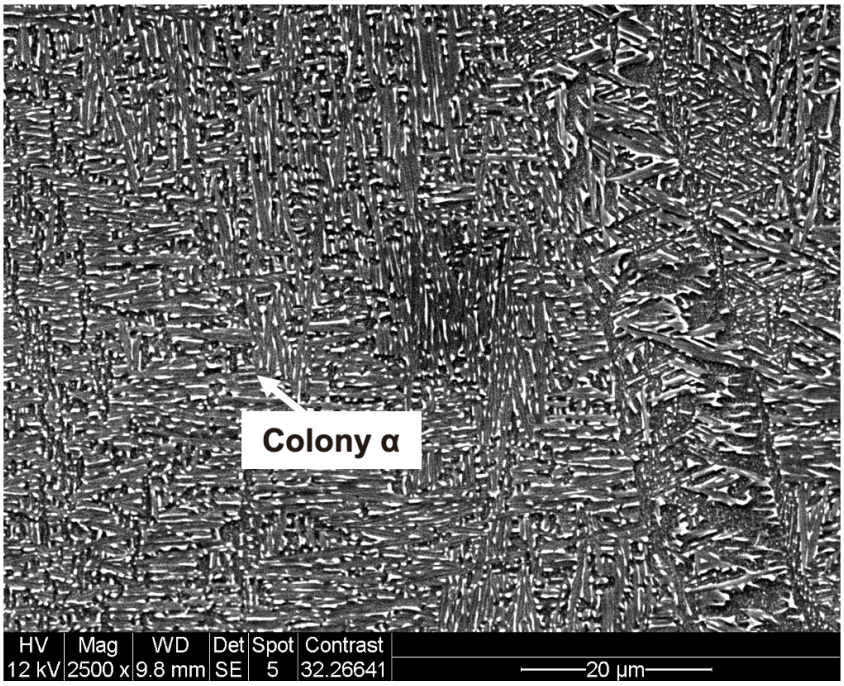

Figure 16: ESEM image of different microstructural features in A3K1.

Two of the most predominant features in the component are basket-weave α and colony α as presented in Figure 15 and Figure *16*, respectively. The features can have two origins: A) The β-phase might have established again by exceeding the transus during heat transfer from the melt. Then the α nucleated in the β-phase at cooling rates below the critical one necessary for the formation of martensite. B) The α-phase nucleated in the

martensite or on its boundaries during martensitic decomposition either during tempering at the chamber temperatures or due to heat transfer from the melt pool.

As depicted in Figure 15 another typical morphology is the grain boundary α located on the prior β grain boundaries visible as clear dark lines nearly parallel to build direction throughout the entire image. Similar to the basket-wave α it could not be formed in the microstructure during the first rapid cooling. It instead nucleated at the prior β grain boundaries in the subsequent heating stages.

Another microstructural feature could also be frequently observed and was not expected. It is indicated as dark feature protruding from the surface with a lamellar structure inside (marked as "bulge" in Figure 15). It was also found in previous studies like the ones of Tan et al. [31] in which it was called "bulge" without further discussion. This type of feature always exhibited an arbitrary shape. There are a few assumptions: It could be martensite in a slightly different morphology or an inclusion like oxide. It could also be a new morphology of the α- phase or fourth it could simply be an etching artifact. This will be further discussed in 4.1.1.4.

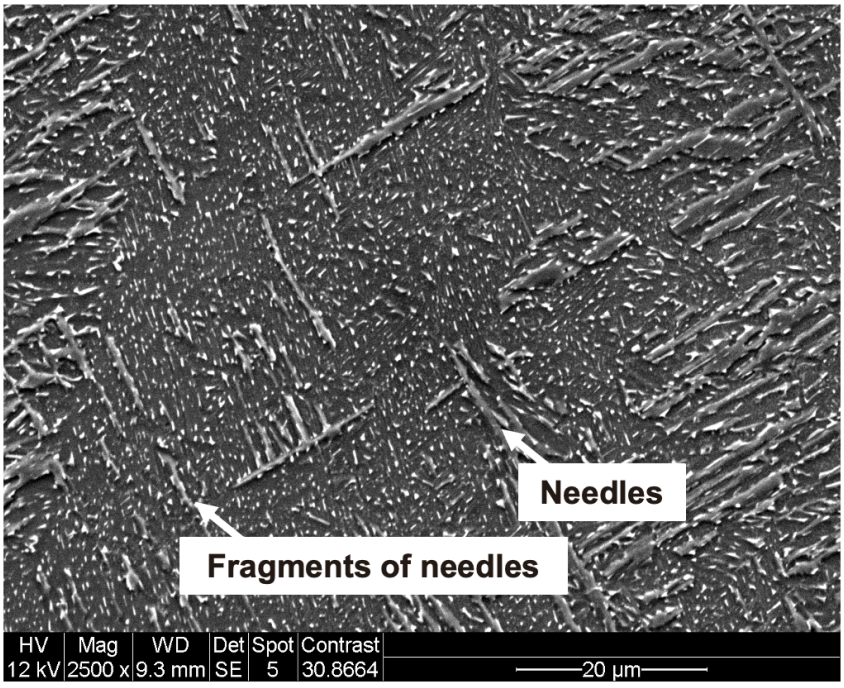

Figure 17: ESEM image of different microstructural features in A3K1.

Figure 17 and Figure 18 show one more main microconstituent which are sharp needles protruding from the surface. The thickness ranges from 0.4 µm to 1.2 µm. The β-phase can be observed on the sides of these needles and sometimes inside of them. They are inclined by 90° indicating that the Burgers-relationship is followed. This phase might be retained martensite. The full decomposition of martensite formed after the initial melting or the re-melting by quick cooling requires temperatures of 800 °C for a certain time depending on the specimen's size and temperature. However, the maximum chamber temperature at the very top powder layer was 650 °C which then decreased with increasing distance from the melt pool. Hence it is likely that not the entire martensite

was decomposed and some martensite is retained. This is in agreement with several studies [33], [44], [45] where martensite was reported in as-built components. The observation of fragments of needles like in Figure 17, which could represent partially decomposed martensite, further supports this assumption.

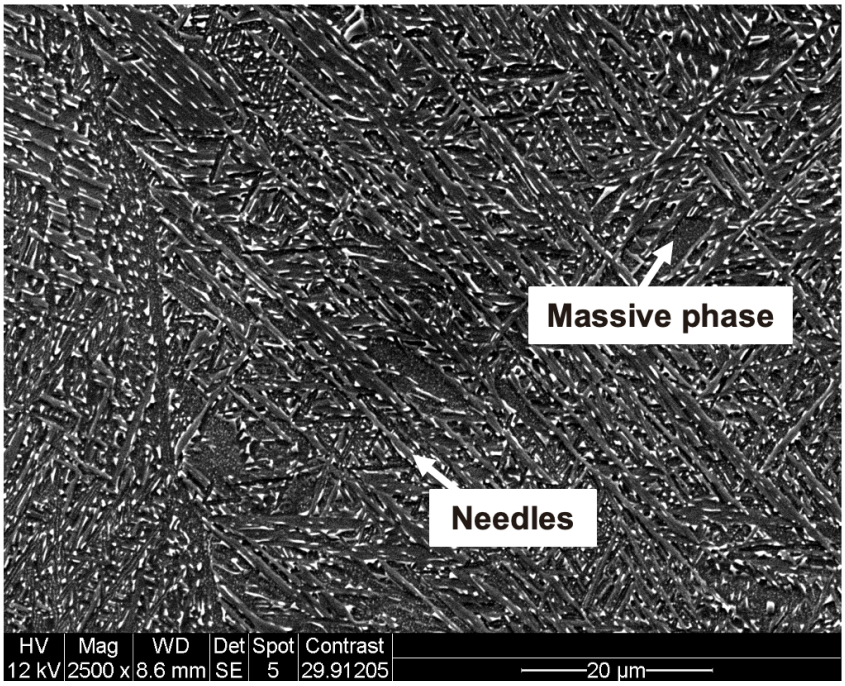

Figure 18: ESEM image of different microstructural features in A3K1.

Furthermore, comparatively large and featureless dark regions were occasionally observed in the microstructure as shown in Figure 18. They were simply called "massive phase" by Raghavan et al. [32], but are not further discussed. There are a few assumptions regarding this type of feature: A) It could be massive martensite which is formed when cooling rates are lower than the ones necessary for typical acicular martensite, as explained in 2.1.3. B) It might be an inclusion such as oxide since titanium has a high affinity with oxygen. C) It could be the α-phase in globular form developed at very low cooling rates or during heat accumulations in later stages after the first rapid cooling steps. D) Another possibility is very coarse α-lamellae due to quick growth in the local region. E) It could be formed due to heterogeneities in composition within the powder. In areas with lack of vanadium, the β-phase cannot be stabilized efficiently at room temperature. The heterogeneities in the powders might be induced during the powder recycling. F) The last option could be recrystallized α-grains. However, this is most unlikely. First, a considerable amount of dislocations must be induced into the crystal prior to recrystallization. Second, the required recrystallization temperature T_R, which is estimated to be approximately 693.4 °C using $T_R \approx 0.4\ T_m$ is only reached for short periods during the heat transfer from the re-melted layers above. The massive phase will be further discussed in 4.1.1.4.

All images shown so far were taken from the bulk of the printed component. However, it is of interest to analyze the very top of the part because it has a different thermal history

compared to the bulk of the component. It was not partially re-melted simply because there are no layers on the top of it. Also it was least exposed to the elevated temperatures in the building chamber. Figure 19 was taken at the very top of A3K1. The microstructure consists mostly of clear fine needles and sometimes fragments of them. The needles have thicknesses between 0.3 μm and 1.3 μm, which are in the same size range as the ones in Figure 18 and also are inclined by 90°. These results further support that these needles are in fact martensite because it is expected to be retained on the very top of the component due to the different thermal history compared to the bulk. The analysis with the FEGSEM also revealed very fine lamellar structures next to the martensite and its fragments in this region.

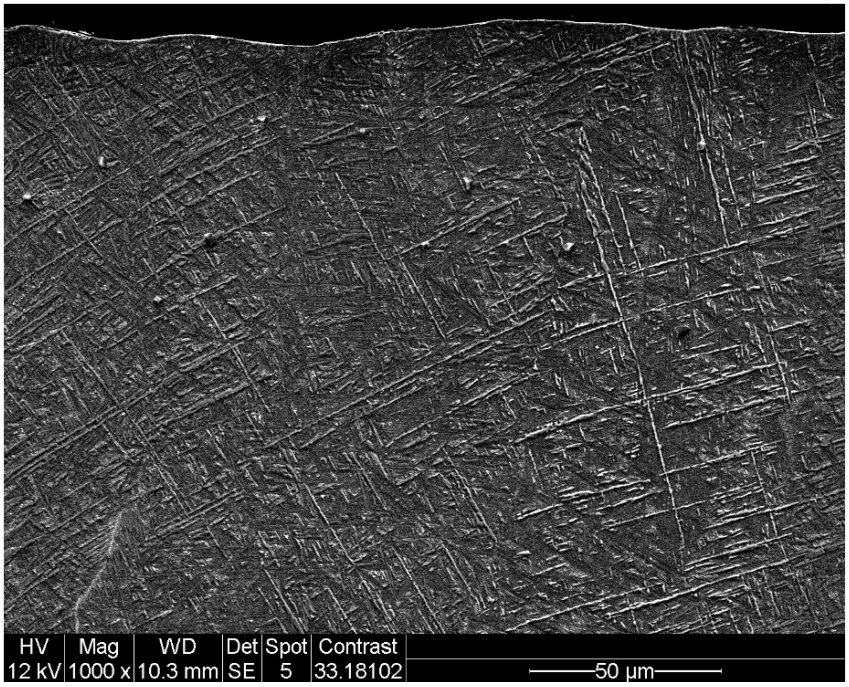

Figure 19: ESEM image of the very top of A3K1.

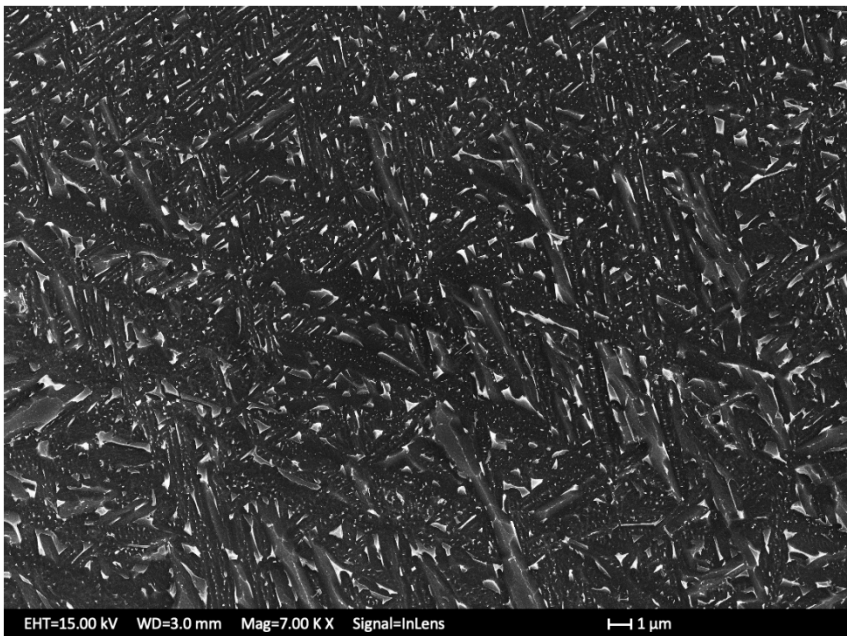

Figure 20: FEGSEM image showing tiny bright dots in the α-phase.

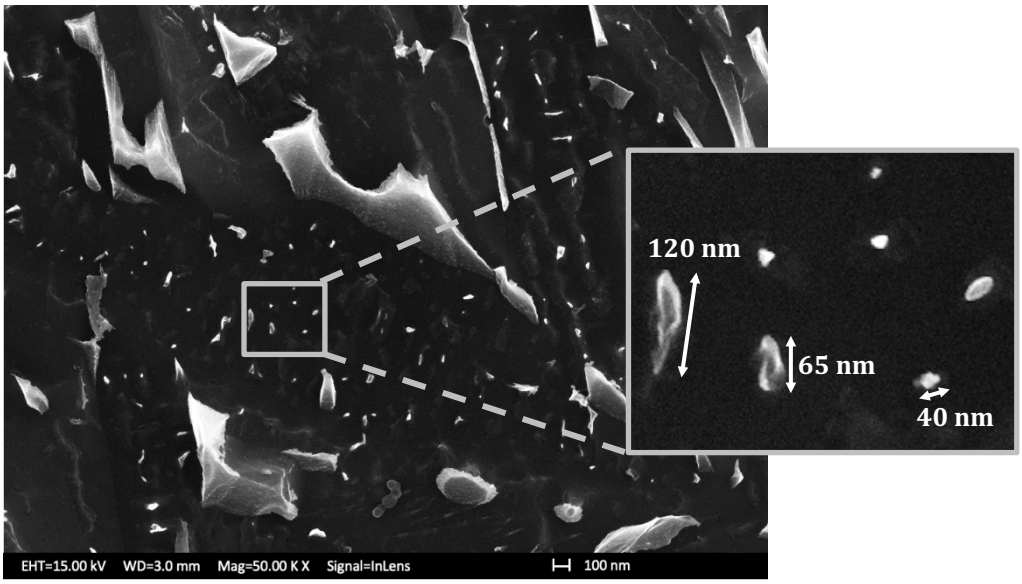

Figure 21: FEGSEM image of tiny bright dots in the α-phase at high magnification and digital zoom into the frame.

At higher magnification by the FEGSEM, an additional phase was visible inside the α-phase in shape of homogeneously distributed tiny particles shown in Figure 20 and Figure 21. They were found everywhere in all three samples of the A3K1, even at the very top. The particles have sizes between 40 and 120 nm with mostly a spherical or elliptical shape. The boundary between particles and α-phase is less clear since a less bright area is surrounding the significant brighter areas. The particles could have different origins and again a few assumptions were made. Because the sample's surfaces were polished by a suspension containing silica nanoparticles with a size of approximately 40 nm, the visible particles could be leftovers from the suspension. The second option might be again etching artifacts. However, the most likely possibility is the precipitation of the intermetallic phase Ti_3Al according to the Ti-Al phase diagram in Appendix 1 and discussion in 2.1.3 and 2.1.4. The size and shape of the particles are in line with the typical Ti_3Al precipitates having sizes of 50 – 200 nm. The precipitates might be developed in the α-phase during the exposure to the elevated temperatures of building chamber after the melting as well as re-melting. Since the temperature in the chamber is decreasing with increasing distance from the top powder layer, the condition for precipitating Ti_3Al could be met at a certain position in the component. According to Carreon et al [26] after one hour at 545 °C a significant number of precipitates were already formed. Maybe an even shorter time at suitable aging temperatures is enough to precipitate Ti_3Al. However it cannot be clearly proved if the particles are in fact Ti_3Al precipitates at this stage. In 4.1.3.3 this will be further discussed.

The α lamellae thickness is of great importance for the mechanical properties of the material. The results obtained by the technique explained in 3.3.2 are plotted in Figure 22 and summarized in Table 7. The bottom and top sections have a similar distribution and almost an equal mean α lamellae thickness. For the middle part, an increased portion of large thickness value is observed.

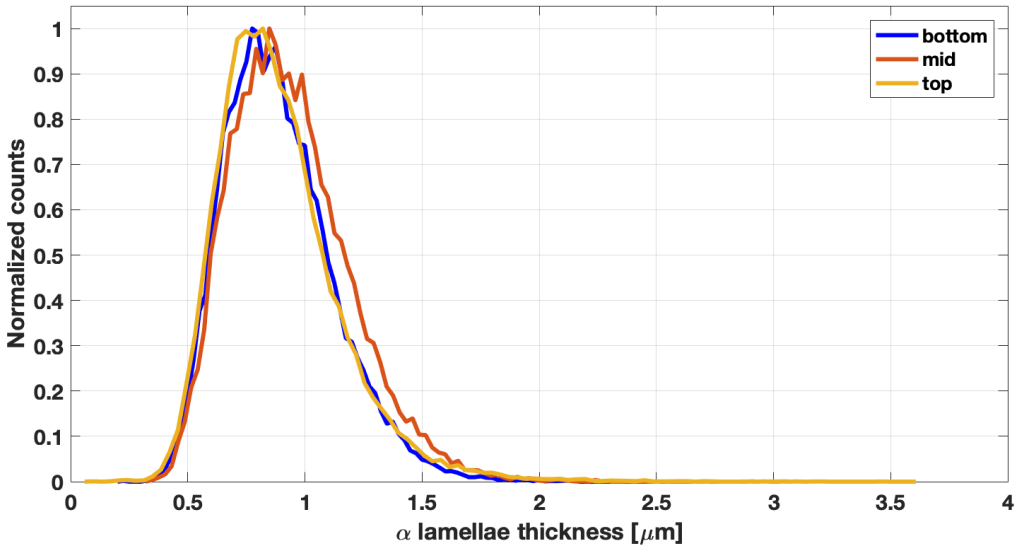

Figure 22: Lamellae thickness distribution for bottom mid and top section of A3K1.

Table 7: Summary of α lamellae thickness for bottom, mid and top section as well as average representative for the entire A3K1.

	mean [µm]	standard deviation [µm]
bottom	0.875	0.235
mid	0.925	0.255
top	0.871	0.261
average	0.889	0.252

The distributions in Figure 22 show a large variation in α lamellae thickness throughout all locations of the specimen. The minimum thickness was measured to be 0.065 µm and the maximum to be 3.674 µm. An almost normal distribution with a tail to large lamellae thicknesses is observed. The large standard deviations of the corresponding mean values listed in Table 7 are in fact the indication of heterogeneous α-lamellae thicknesses. The entire distribution is shifted to increasing lamellae thicknesses with increasing mean value. Hence it is believed that the average in Table 7 is a meaningful material's parameter despite the relatively large standard deviations.

The results for the α-lamellae thicknesses indicate a graded microstructure. With increasing building height, the α lamellae thickness is first increasing from the bottom to mid-section and then decreasing from the mid to the top section whereas the smallest thicknesses are measured in the top. The graded microstructure can be explained by two competing mechanisms as follows. It is known that with increasing cooling rates and decreasing holding times at elevated temperatures the microstructure becomes finer. The part of the component next to the building table is exposed for the longest time to the temperatures in the building chamber and the top part of the component for the shortest time. According to this argumentation it would be expected that the lamellae thickness is continuously decreasing with increasing build height. However, the cooling rate also influences the feature size. Notice it is not constant throughout the entire build and decreases with increasing building height. Hence the cooling rate at the very bottom is the highest, which has according to the results for the lamellae thicknesses a larger influence

on the feature sizes in the microstructure than the holding time. Also, due to the high thermal conductivity of the building table, less heat accumulation could have happened and hence the bottom section is less affected by the chamber temperatures. Consequently, a small α lamellae thickness, similar as the top, is observed here. The largest mean α lamellae thickness is observed in the middle. From the mid-section towards the top, the lamellae thickness is then decreasing which presents a larger influence of the holding time than the cooling rate. It seems that only at the very bottom of the component the high cooling rate is dominating whereas further upwards the shorter exposure to the chamber temperature is the governing factor that influences the lamellae thickness.

4.1.1.3 Microstructure of A3bK1 (90µm; as-built)

An overview about the microstructure of A3bK1 is given by the ESEM image in Figure 23. Again, a very fine and heterogeneous fully lamellar microstructure, similar to the ones of A3K1, is observed. It contains the colony α, basket-weave α, grain boundary α, retained martensite, massive phase and bulges. Furthermore, there was no significant difference observed between the samples from the bottom, mid and top section. This observation is expected because the thermal history is nearly the same as the ones of the A3K1. The microstructure of the A3bK1 is slightly coarser, which will be further quantified in 4.1.1.5. In the following section the observed phase morphologies are discussed in more detail.

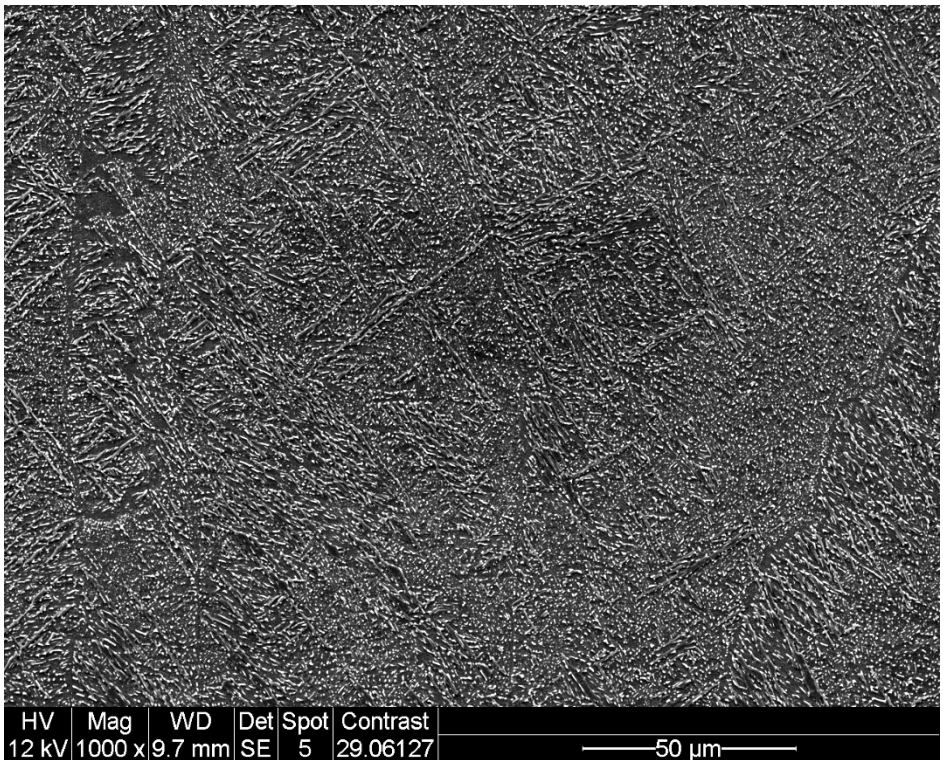

Figure 23: ESEM image as overview microstructure of A3bK1.

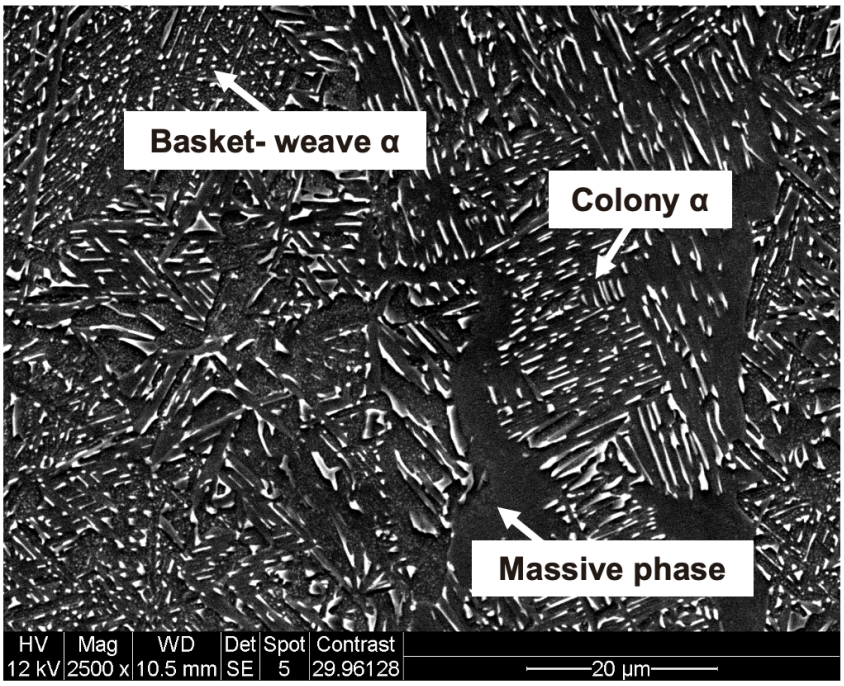

Figure 24: ESEM image of different microstructural features in A3bK1.

As depicted in Figure 24, two of the most predominant features in this component are the Widmannstetten structures - basket-weave α and the colony α. They are established in the same way as the ones in the A3K1.

Compared to the A3K1, the massive phase was observed more frequently and it also has larger sizes in the A3bK1. Because it is not known what exactly this feature is, only a few assumptions can be made as given in 4.1.1.2. Interestingly, the assumption that the massive phase is globular α could explain why it now occurs more often. The Q10plus theme for 50 µm-layer thickness and the Q20 plus theme for 90 µm-layer thickness are designed to generate the same energy per volume in order to compensate the larger layer thicknesses in the latter case. It is expected that the melt pools in the A3bK1 are larger compared to the ones for the A3K1, leading to a comparatively lower cooling rate. Consequently, more globular α established from extremely low cooling rates might be formed in the microstructure of the A3bK1.

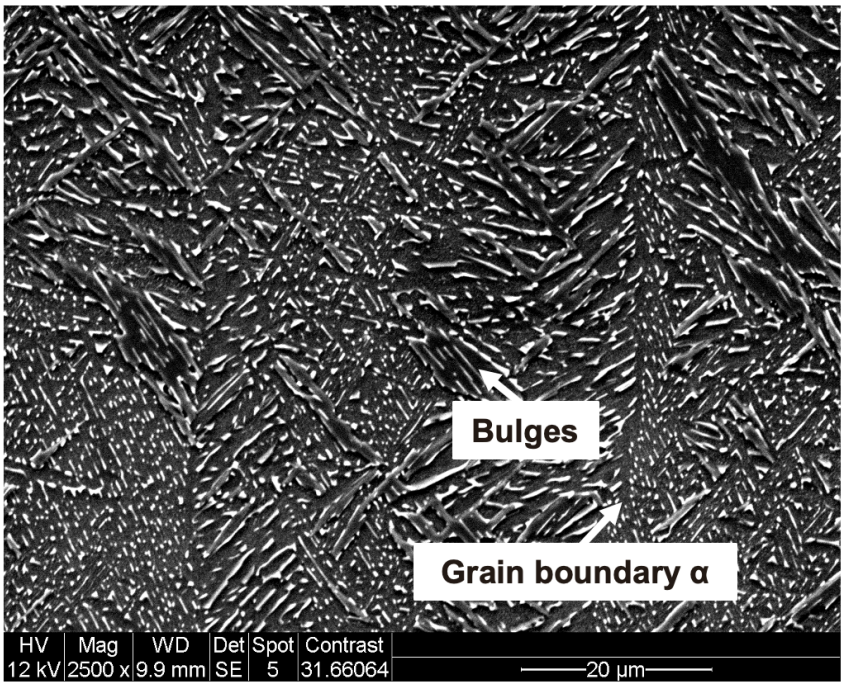

Figure 25: ESEM image of different microstructural features in A3bK1.

Figure 25 shows other two typical features, grain boundary α and bulges. There are no significant differences in morphology and size compared to the A3K1.

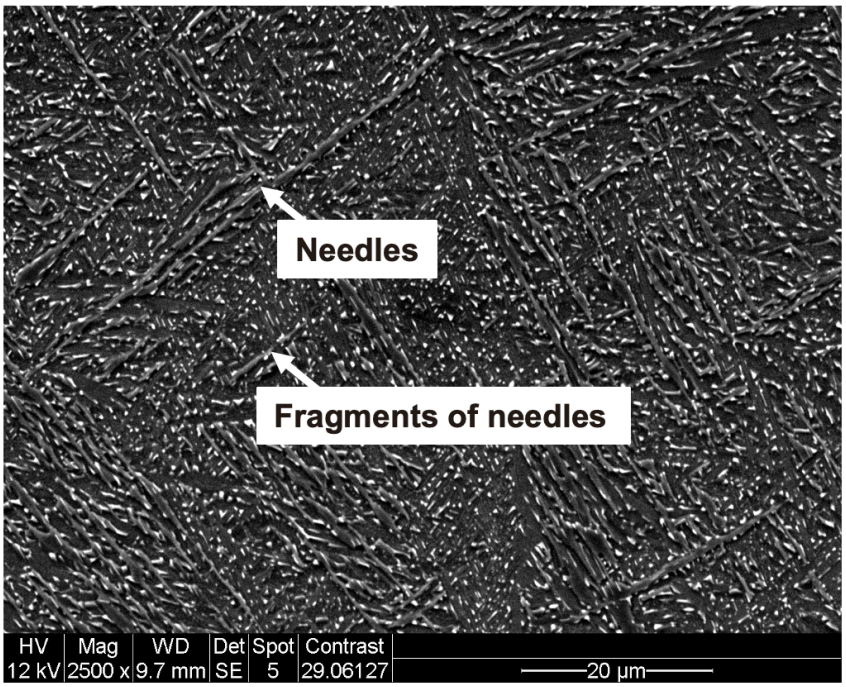

Figure 26: ESEM image of different microstructural features in A3bK1.

As already indicated in the overview in Figure 23, the microstructure of the A3bK1 contains retained martensite. The characteristic needles and their fragments are exhibited in Figure 26 in more detail. They also follow the Burgers-relationship indicated by inclination angles of 90°. The thickness is again between 0.4 µm and 1.2 µm.

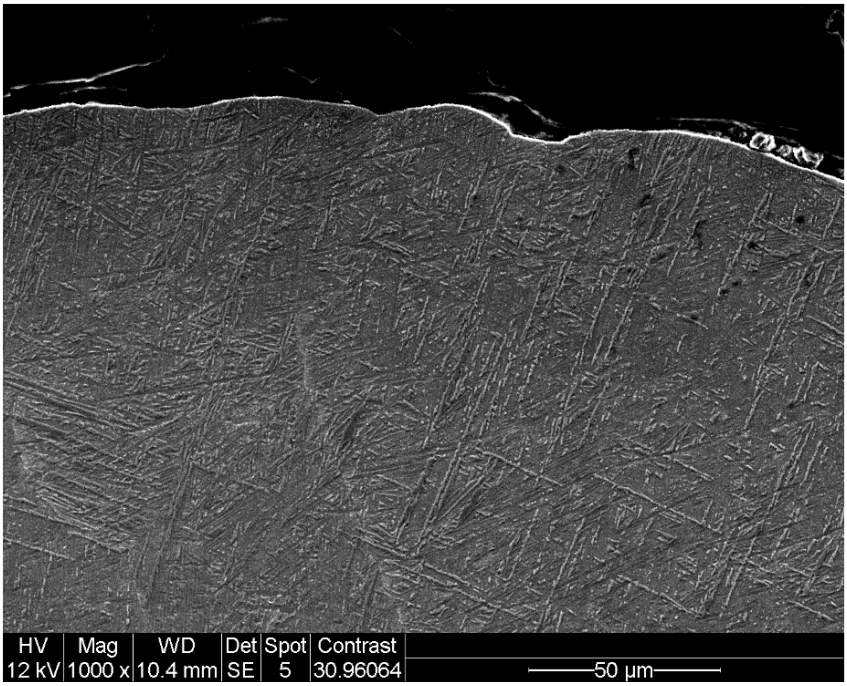

Figure 27: ESEM image of the very top of A3bK1.

The very top of the A3bK1 is depicted in Figure 27. The microstructure here is similar to the ones of the very top of A3K1 and mainly consist of martensite. The sizes are again in the range of 0.3 and 1.3 µm. Also, the FEGSEM revealed very fine lamellar structures in this region.

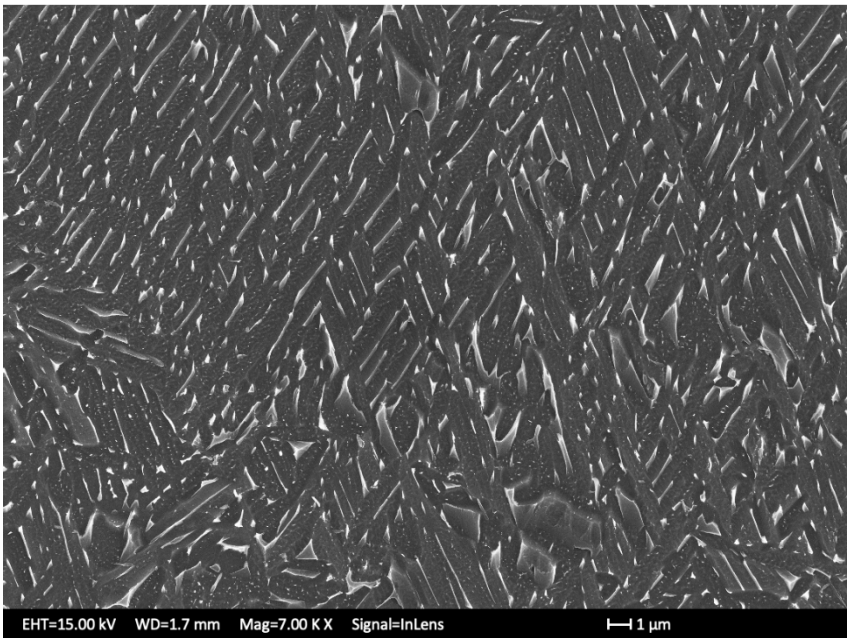

Figure 28: FEGSEM image showing tiny bright dots in the α-phase.

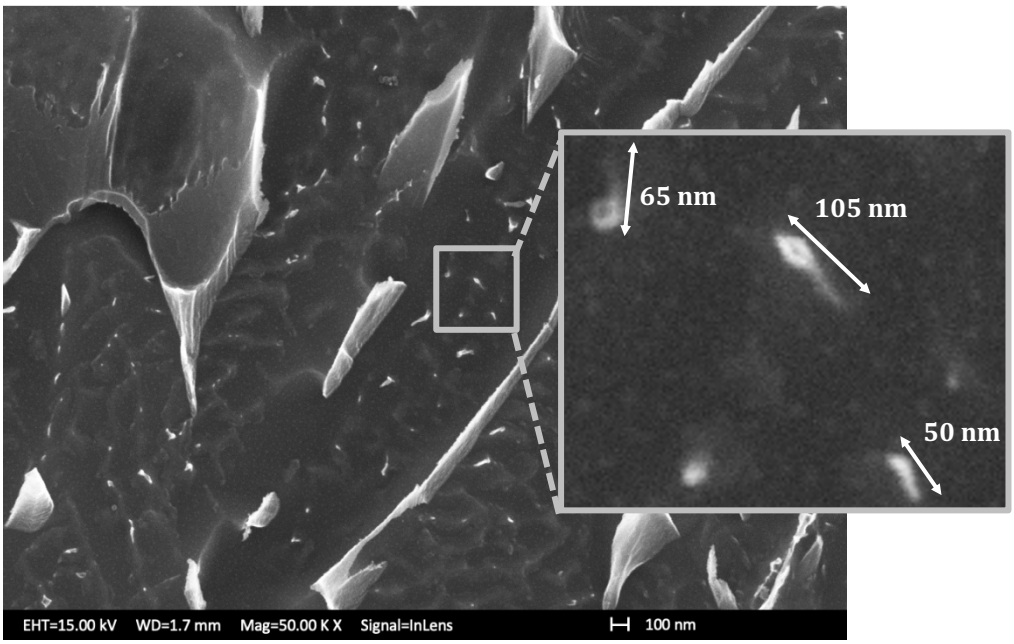

Figure 29: FEGSEM image of tiny bright dots in the α-phase at high magnification and digital zoom into the frame.

When the microstructure was analyzed by the FEGSEM at higher magnification, again tiny bright particles were observed in the α-phase, which is shown in Figure 28 and Figure 29. The particles have a similar shape and size compared to the ones in the A3K1. They could be established by the same reasons because of the relatively similar thermal history of the two as-built components. The particles are further discussed in 4.1.1.4.

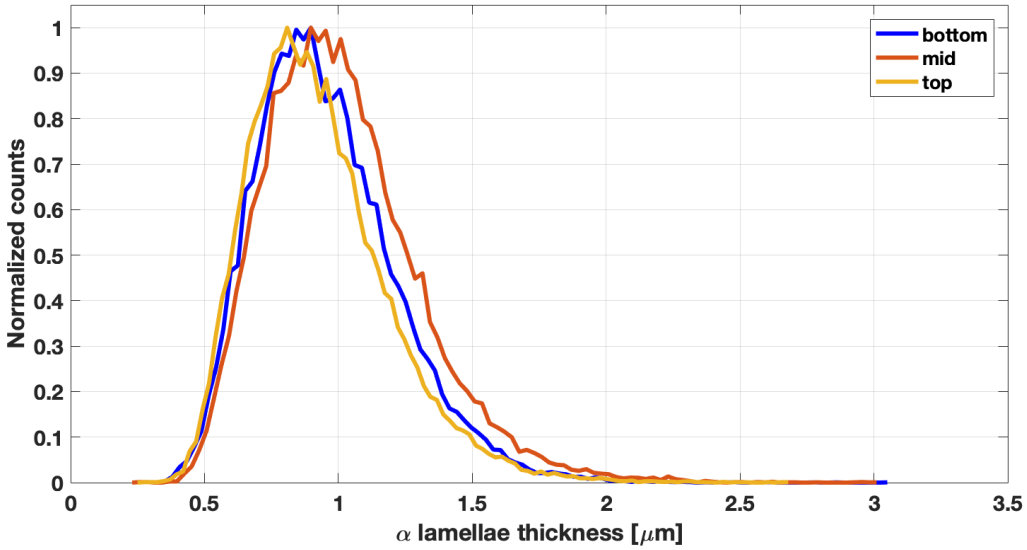

Figure 30: Lamellae thickness distribution for bottom mid and top section of A3bK1.

Table 8: Summary of α lamellae thickness for bottom, mid and top section as well as average representative for the entire A3bK1.

	mean [µm]	standard deviation [µm]
bottom	0.941	0.263
mid	1.002	0.288
top	0.913	0.260
average	0.949	0.272

The α-lamellae thicknesses of A3bK1 are plotted in Figure 30 and summarized in Table 8. The distributions in Figure 30 show again a relatively large variation in α-lamellae thickness in every section of the component. The minimum thickness was measured to be 0.233 µm and the maximum thickness to be 3.031 µm. The thicknesses are again almost normal distributed with a tail to the right side. Table 8 shows a similar trend for change in α-lamellae thickness with increasing build height as the A3K1. The largest mean α lamellae thickness is observed in the middle followed by the one at the bottom. This type of graded microstructure was already discussed for the A3K1, which is also valid for the A3bK1.

4.1.1.4 Microstructure of A3bK85 (90µm; post-processed)

An overview microstructure of the A3bK85, which was HIPed and then subjected to a heat treatment, is given in Figure 31. Notice the thermal history is different compared to the as-built components. It shows a heterogeneous fully lamellar microstructure different from the ones of the as-built components A3K1 and A3bK1. The features observed in the microstructure are colony α, basket-weave α, grain boundary α, massive phase, bulges and α twins. The latter one was not found in the as-built components. The features are significantly larger, and no martensite is present. The HIP temperature exceeded 800 °C, which is necessary to fully decompose martensite. Absence of needles supports the conclusion that the needles in the as-built components are in fact martensite since they completely disappeared after post-processing.

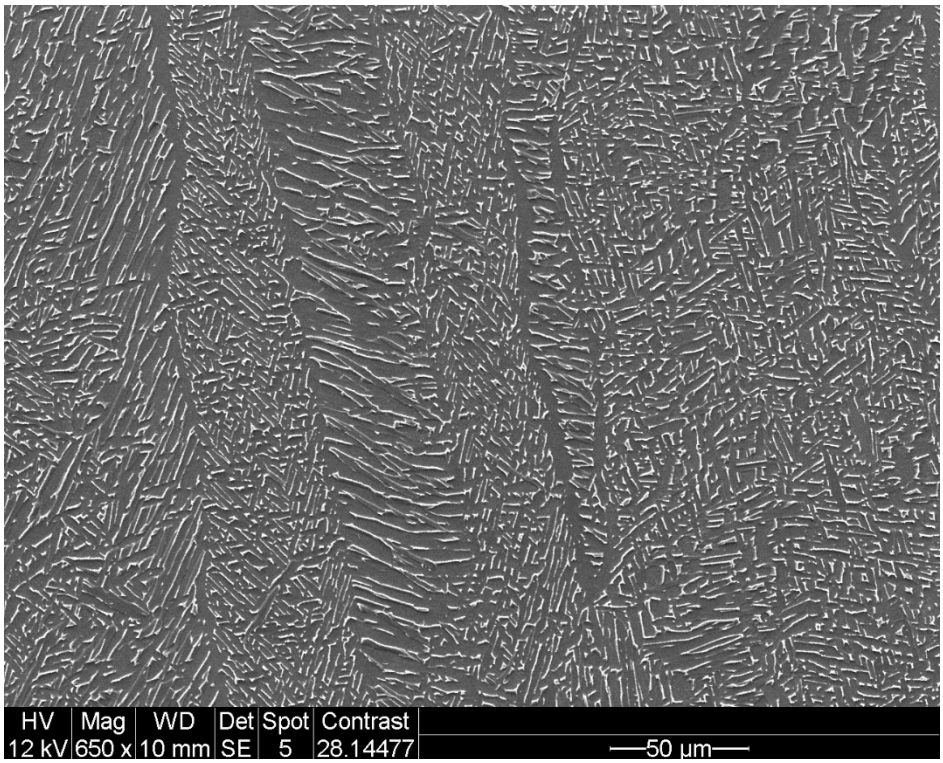

Figure 31: ESEM image as overview microstructure of A3bK85.

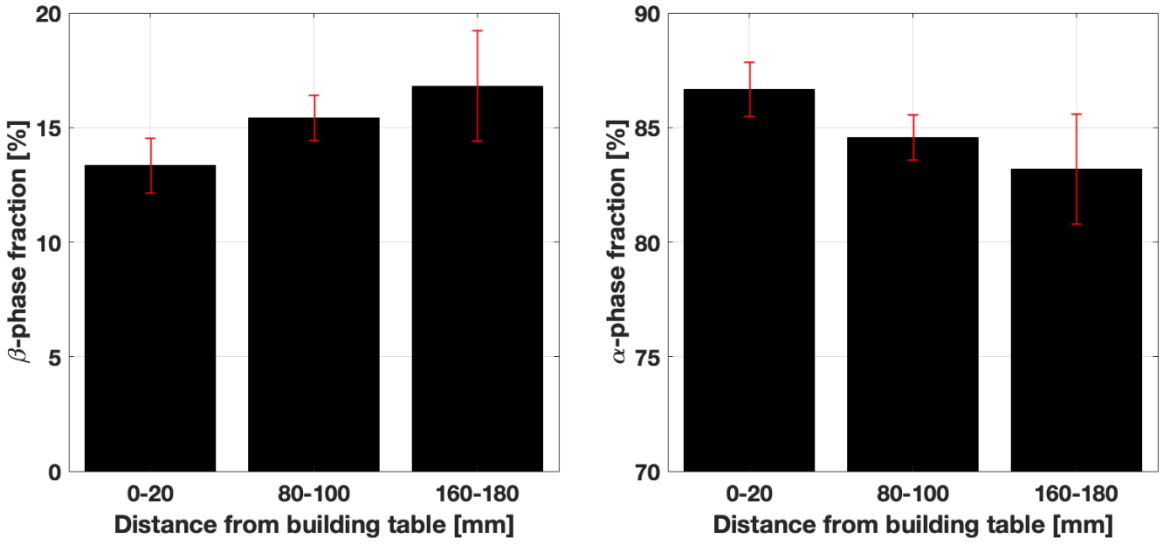

Figure 32: Phase fraction of the α- and β-phase as a function of build height.

The phase fraction of the α- and β-phase as a function of distance from the building table is plotted in Figure 32. It can clearly be seen that the β-phase fraction is monotonically increasing with increasing build height whereas the α-phase fraction is continuously decreasing. To understand this, first, it must be pointed out that the amount of α-phase is primarily affected by the nucleation of α-phase in the β-crystal during cooling from above the transus. It is known in general that with increasing undercooling the nucleation rate is increased. During the EBM the cooling rate in the bottom part of the component next to the building table is higher. Hence less heat accumulates in the alloy there and the overall temperature is lower. Consequently, more α-crystals are able to nucleate in the bottom-section than in the top-section, leading to a higher α-phase fraction.

EDS analysis of the α- and β-phase was possible because the microstructure is coarser compared to the as-built components. The point analysis result of the alloy's main elements is listed in Table 9. It shows significant enrichments of aluminum in the α-phase and vanadium in the β-phase. This was expected because they are the respective stabilizer elements and they preferably diffuse into the corresponding phase they stabilize. The vanadium content of 23.28 wt% in the β-phase appears relatively high. However it must be considered that the phase fraction of the β-phase is clearly lower than that of the α-phase, as visible in Figure 32. Vanadium diffusing out from the α-phase, the main constituent in the microstructure, must be accumulated at the remaining sites, which are the β-phase. Furthermore, the compositions measured by EDS must be interpreted more as qualitative than quantitative results since they are dependent on acceleration voltage and calibration of the detector. A more detailed compositional analysis is given in Table 10 and Table 11. In the following section the microstructural features found in the A3bK85 are presented in detail.

Table 9: Average composition of α- and β-phase in A3bK85 determined by EDS point analysis.

	Aluminum [wt%]	**Titanium [wt%]**	**Vanadium [wt%]**
α-phase	6.62 ± 0.21	91.13 ± 0.29	2.24 ± 0.14
β-phase	2.09 ± 0.23	74.63 ± 1.05	23.28 ± 1.29

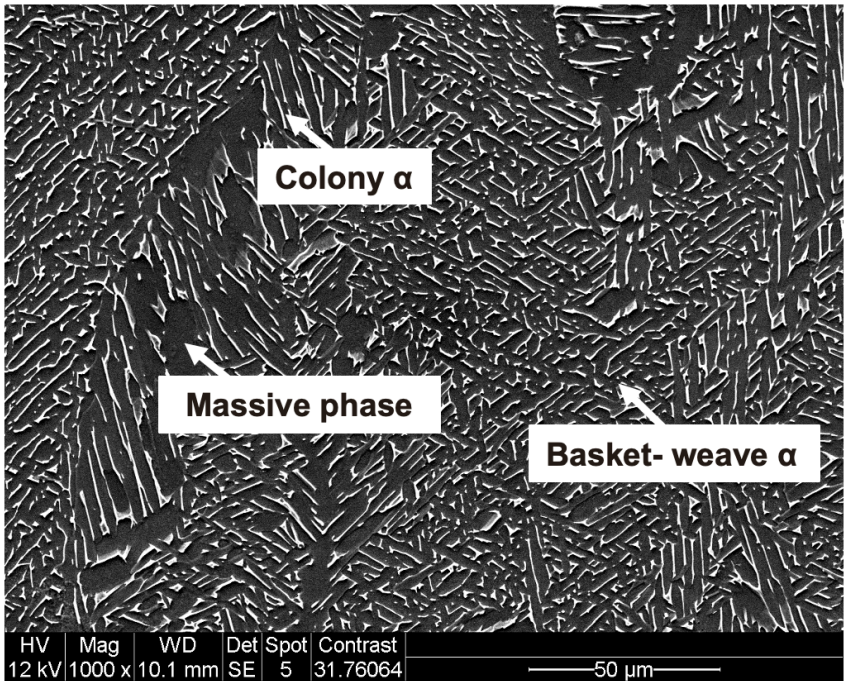

Figure 33: ESEM image of different microstructural features in A3bK85.

Similar to the as-built components, two main features are the colony α and basket-weave α. Both structures are established either during the EBM process as explained for the as-built samples or upon the final decomposition of the retained martensite during post-processing.

Figure 33 presents the massive phase, which is another frequently observed feature. An EDS point analysis according to Appendix 6 was performed to analyze the composition of the alloy's main elements and a few trace elements to check potentially impurities. The composition was then compared to the ones of the α- and β-phase in the neighboring area. The results are listed in Table 10.

Table 10: Average composition of massive phase by EDS point analysis according to Appendix 6.

	O [wt%]	**Al [wt%]**	**Si [wt%]**	**Ti [wt%]**	**V [wt%]**	**Fe [wt%]**
α-phase	3.17±0.49	6.50±0.15	0.04±0.04	87.95±0.67	2.17±0.28	0.19±0.13
Massive phase	3.08±0.42	6.36±0.21	0.05±0.03	87.79±0.43	2.17±0.14	0.56±0.36
β-phase	2.00±1.04	1.99±0.21	0.01±0.02	70.89±1.70	22.09±0.94	3.02±0.42

Besides elements listed in Table 10, nitrogen having high affinity with titanium was also checked, but in all three types of sites its content was negligible. Compared to the β-phase, the α-phase seems to have a higher oxygen content but lower iron content. This is in line with the theory that oxygen is an α-stabilizer and iron a β-stabilizer. Anyhow the oxygen contents in general seem to be high. Either most of the measured oxygen comes from an oxide layer on the surface or there was a detection error since it is difficult to detect light elements accurately with EDS. Also, the iron content in the β-phase appears to be higher than expected but the same argumentation as for the high amount of vanadium in this phase is valid.

As seen in Table 10, the massive phase has the same composition as the α-phase when considering the standard deviations. Hence a few explanations of this unknown feature, such as massive martensite and inclusions, can be excluded. This is because massive martensite would have exhibited an increased vanadium content, and inclusions should not contain the same amount of oxygen, silicon, nitrogen or iron as the α-phase. Also, it is unlikely that the vanadium content is the same as that in the α-phase even if there is a lack of vanadium in this area. It is therefore expected that the massive phase is another morphology of the α-phase which might be recrystallized, globulized or a normal lamella which is excessively coarsened compared to the surrounding ones. However, the recrystallized α-phase is the least probable option. The yield strength of Ti-6Al-4V is approximately 1000 MPa at room temperature and it is significantly decreased at temperatures above 700 °C [11]. Theoretically plastic deformation is possible under the pressure (100 MPa) applied by HIPing. Nevertheless, the massive phase was also observed in the as-build components which were not plastically deformed before. Though recrystallization still cannot be completely excluded especially in the A3bK85, but it is most questionable.

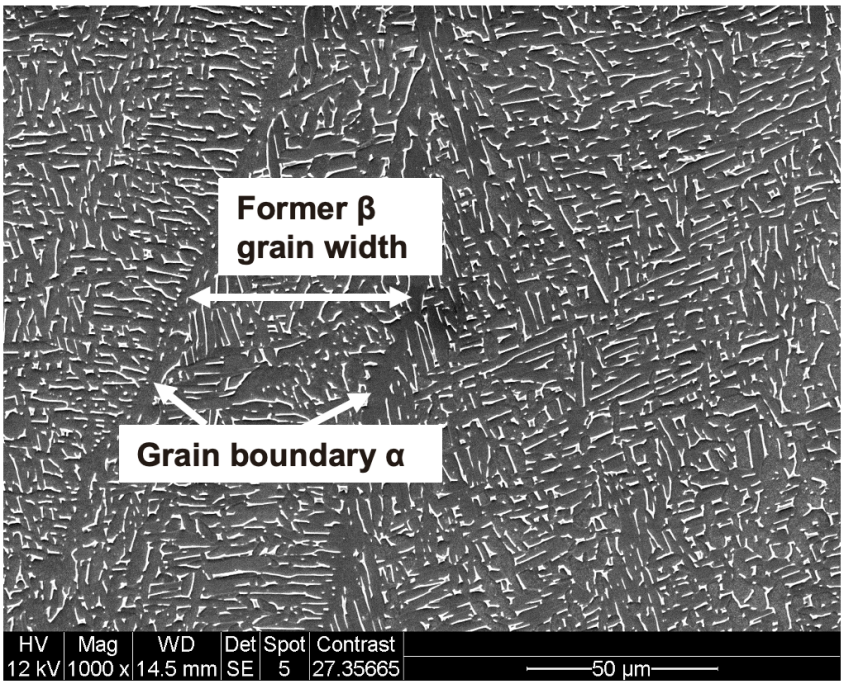

Figure 34: ESEM image of different microstructural features in A3bK85.

In Figure 34 a former β-grain is clearly depicted by two grain boundary α layers. A strong variation of the grain width within one grain is observed. In this image it changes from 72 µm to 33 µm over a distance of 163 µm. The surrounding grains seem to have a larger width than the indicated one, which is in agreement with the OM observations in 4.1.1.1 where grain sizes between 30 to 240 µm were detected.

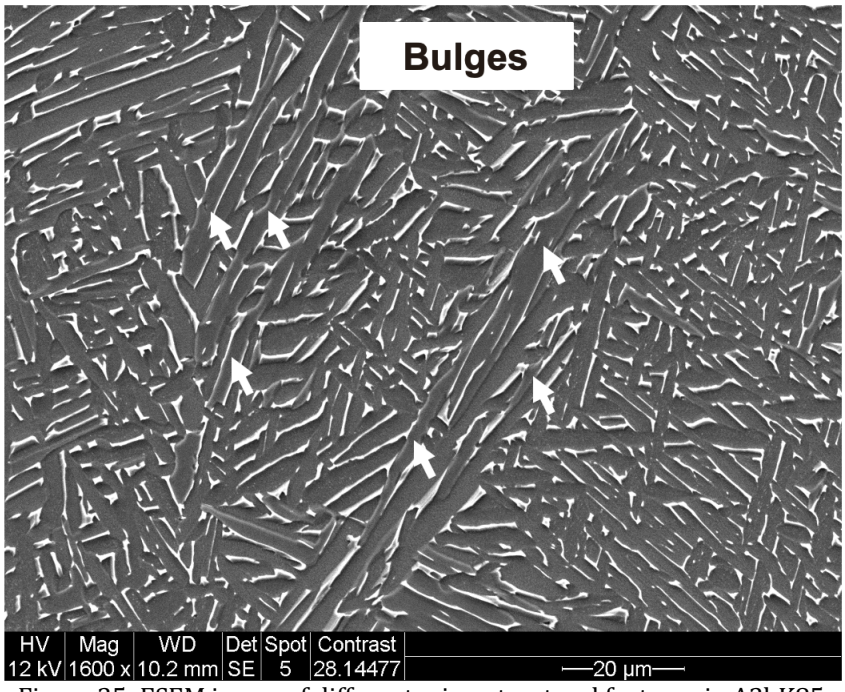

Figure 35: ESEM image of different microstructural features in A3bK85.

Similar to the as-built components, the A3bK85 exhibits bulges as shown in Figure 35. An EDS point analysis was performed to analyze its elemental composition. The location of

the points is given in Appendix 7. The composition was then compared to the ones of the α-and β-phase in the neighboring area. The results are listed in Table 11.

Table 11: Average composition of bulges by EDS point analysis according to Appendix 7.

	O [wt%]	Al [wt%]	Si [wt%]	Ti [wt%]	V [wt%]	Fe [wt%]
α-phase	3.04±0.14	6.18±0.35	0.03±0.02	88.43±0.41	2.30±0.60	0.04±0.04
Bulge	2.43±0.06	6.14±0.18	0.04±0.02	88.90±0.16	2.48±0.23	0.02±0.04
β-phase	2.22±0.76	2.14±0.35	0.02±0.02	73.27±3.06	19.67±2.31	2.68±0.64

The EDS measurement in Table 11 indicates that the bulges are normal α-phase despite of the slight difference in oxygen content which could just be a surface artifact. In this case it cannot be martensite since it would be otherwise enriched in vanadium. It is also unlikely to find martensite in post-processed samples. Hence it can be concluded that it is either a different α-phase morphology or an etching artifact. Further analysis is required to identify and understand the bulges.

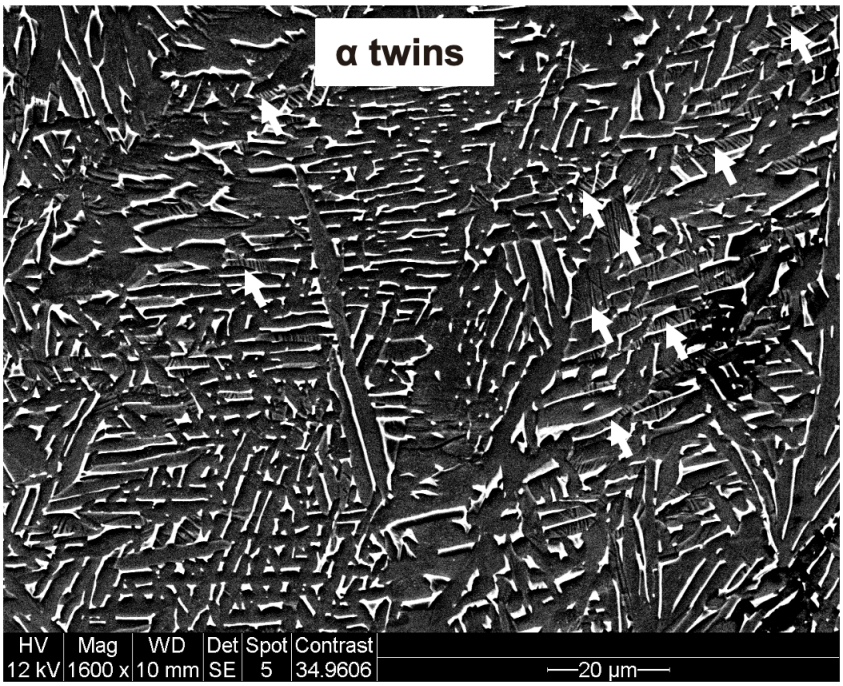

Figure 36: ESEM image of different microstructural features in A3bK85.

Another microstructural feature which was sometimes observed in the A3bK85 are small black lines with a thickness of about 250 nm mostly parallel aligned inside of α-lamellae as shown in Figure 36. This morphology is a characteristic of twins. It cannot be explicitly verified how they are formed. There are three possible reasons for crystal twins. The first one is the deformation twin generated in the crystal during plastic deformation. HIP was done at 920 °C under 100 MPa. As mentioned in 2.1.2, plastic deformation could have happened and hence deformation twins might be generated. The fact that no twins were observed in the as-built samples may support this hypothesis. However, mechanical twinning generally occurs when slipping caused by dislocation movement is restricted. It is generally reported for low temperatures and less probable at high temperatures.

Another type of twins are transformation twins which are formed when the crystal is transformed with orientation differences during heating or cooling. As illustrated in the schematic phase diagram of Ti-6Al-4V in Figure 4, the fraction of the β-phase is increasing with increasing temperatures and vice versa. Accordingly, phase transformation could have happened during the HIP. The third type of twins are growth twins which occur during a crystal growth. The normal pattern of layer-by-layer growth may be interrupted by a supersaturation of atoms at the preferred growth sites. Since the growth of α-lamellae is diffusion controlled at elevated temperatures this type of twins could have been occurred as well. This might be again supported by the fact that no twins were found in the as-built samples where the lamellae are significantly thinner and hence almost no growth happened. Further investigation is necessary in order to clarify how the twins were formed. Regardless of the formation mechanism, the twins are obstacles for dislocation movement and hence increase the strength of the material.

Same as for the as-built components, the microstructure of the very top of the A3bK85 was examined, as depicted in Figure 37. Here, the same microstructure as for the bulk of the material was found. Post-processing removed all the needles which again confirms the existence of martensite in the as-built components.

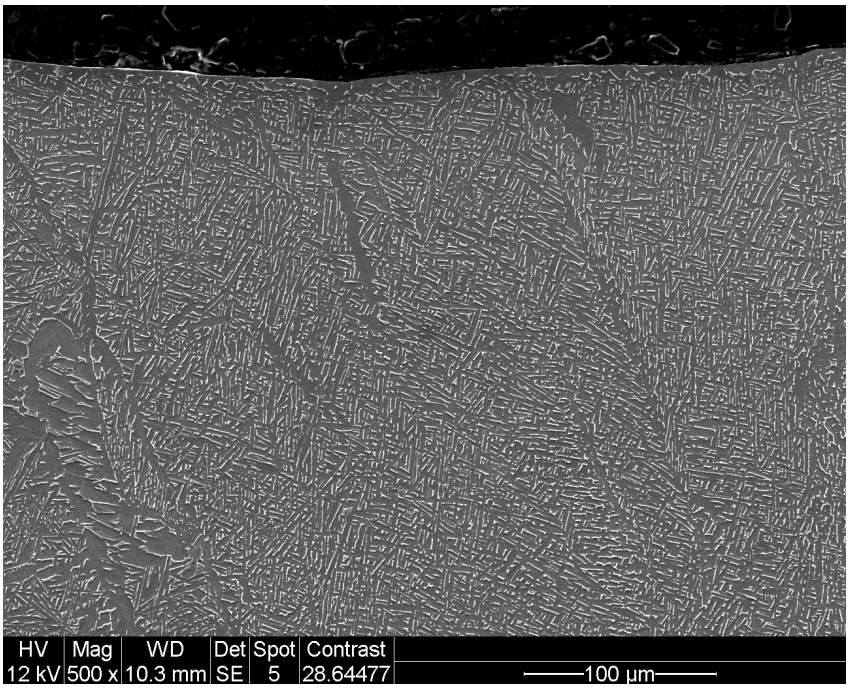

Figure 37: ESEM image of the very top of A3bK85.

When the microstructure was analyzed by the FEGSEM at higher magnification, the tiny bright dots were also visible inside the α-phase, as shown in Figure 38 and Figure 39. This type of feature could be found at all locations within the entire component even at the very top.

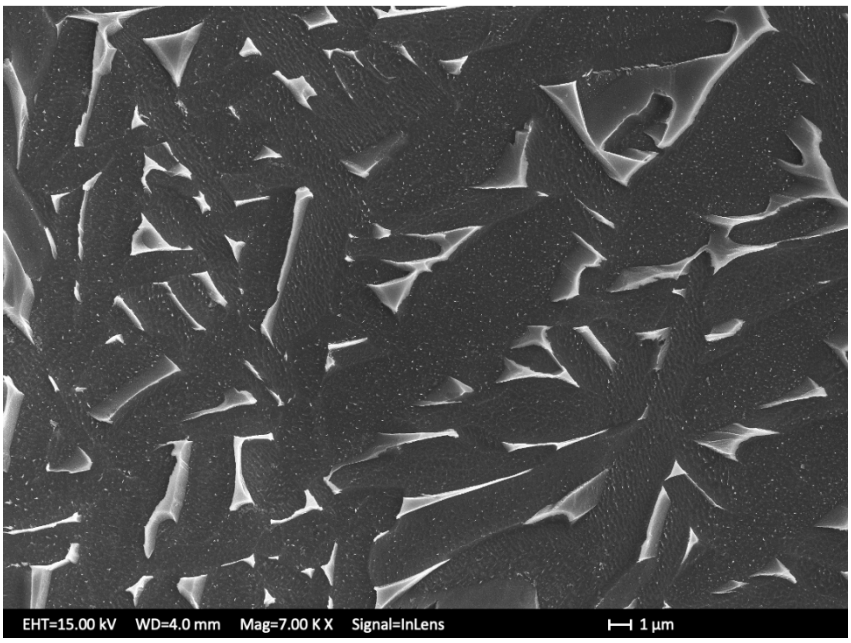

Figure 38: FEGSEM image showing tiny bright dots in the α-phase.

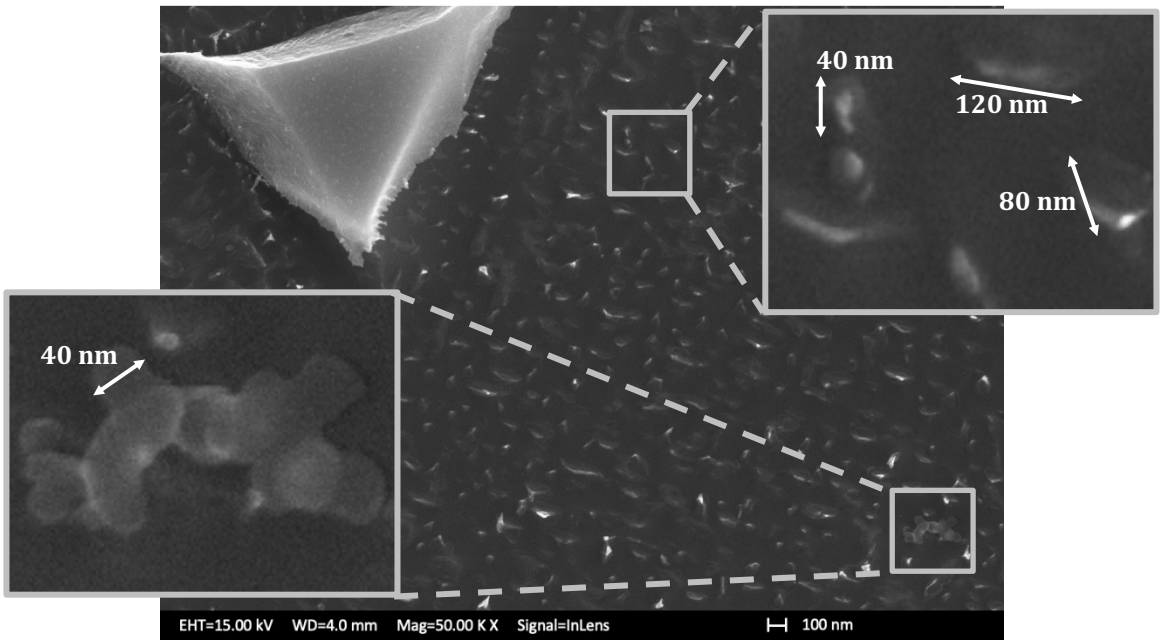

Figure 39: FEGSEM image of particles in the α-phase at high magnification and digital zoom into the frames.

These particles have the approximately the same size and shape as the ones in the as-built condition. It is again difficult to identify from the contrast where the actual particle ends and where the α-matrix begins. Beside the particles in the upper frame of Figure 39 another type of particles was also detected in the lower frame, which have a spherical shape with sizes of about 40 nm in the form of clusters. This type of particles is supposed to be a left-over from the polishing suspension since the size fits exactly to the ones provided by the manufacturer. Hence the assumption that the particles within the α-phase marked in the upper frame are left-overs from the polishing suspension can be withdrawn and only the possibilities of etching artifacts and precipitation of Ti_3Al remain.

For this component the precipitates cannot be developed during building because it was post-processed at temperatures above the Ti_3Al solvus of 550 °C. Hence they could only be formed during the second heat treatment step at 538 °C for 4h, which was the last step of the entire processing history. It was stated in 2.1.4 that the most suitable temperature for aging Ti-6Al-4V is 545 °C which is close to the heat treatment temperature in the current study. Also, the holding time of 4 hours should be enough to precipitate Ti_3Al. According to Carreon et al. [26] even 1 hour at 545 °C was sufficient for the aging of the alloy.

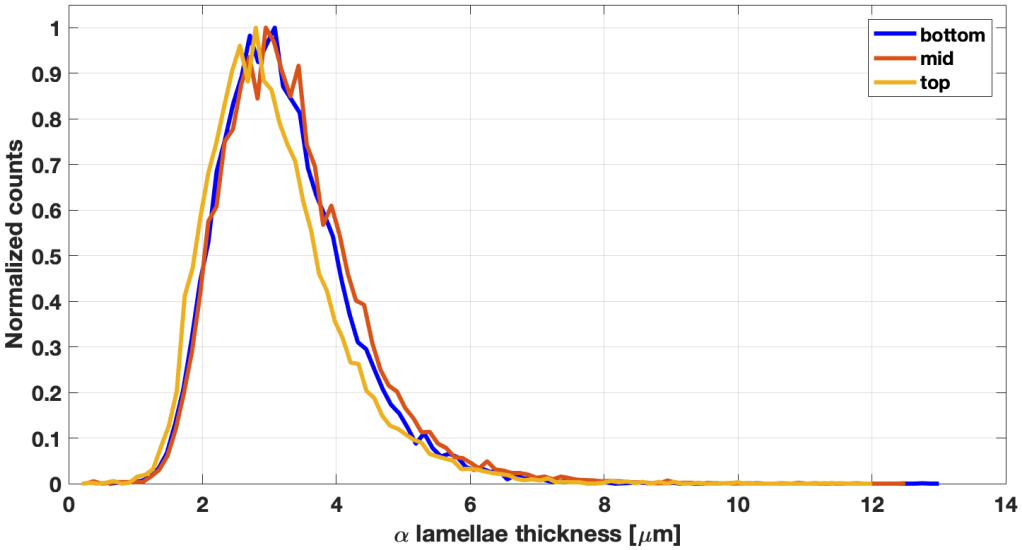

Figure 40: Lamellae thickness distribution for bottom mid and top section of A3bK1.

Table 12: Summary of α lamellae thickness for bottom, mid and top section as well as the average representative for the entire A3bK85.

	mean [µm]	**standard deviation [µm]**
bottom	3.168	0.973
mid	3.273	1.056
top	3.014	0.999
average	3.159	1.016

The α-lamellae thickness of the component was measured by the method explained in 3.3.2 and the results are plotted in Figure 40 as well as summarized in

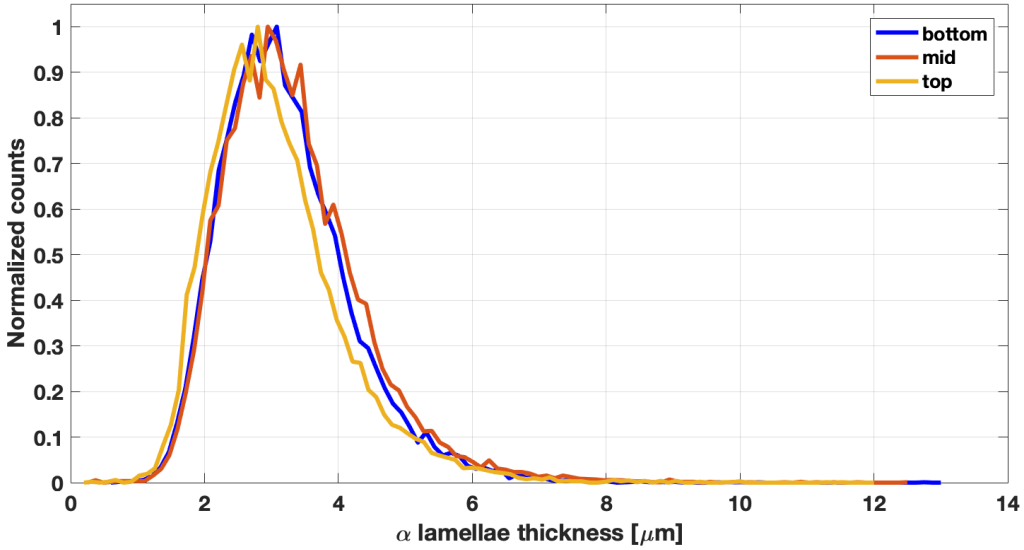

Figure *40*: Lamellae thickness distribution for bottom mid and top section of A3bK1.

Table *12*.

The distributions in Figure 40 show a large variation in α-lamellae thicknesses in each location in the component. The minimum thickness was measured to be 0.235 μm and the maximum thickness to be 12.750 μm. However, the maximum detected thicknesses are not the ones from normal Widmannstetten lamellae, instead it might be from a massive phase. The thicknesses are again almost normal distributed with a tail to the right side.

Table 12 shows the same trend for variation of α-lamellae thickness with increasing build height as that of A3K1 and A3bK1. The thickness first increases from the bottom to mid-section and then decreases from the mid to the top-section. Averagely, the α-lamellae were thinnest at the top. The results in Figure 40 and

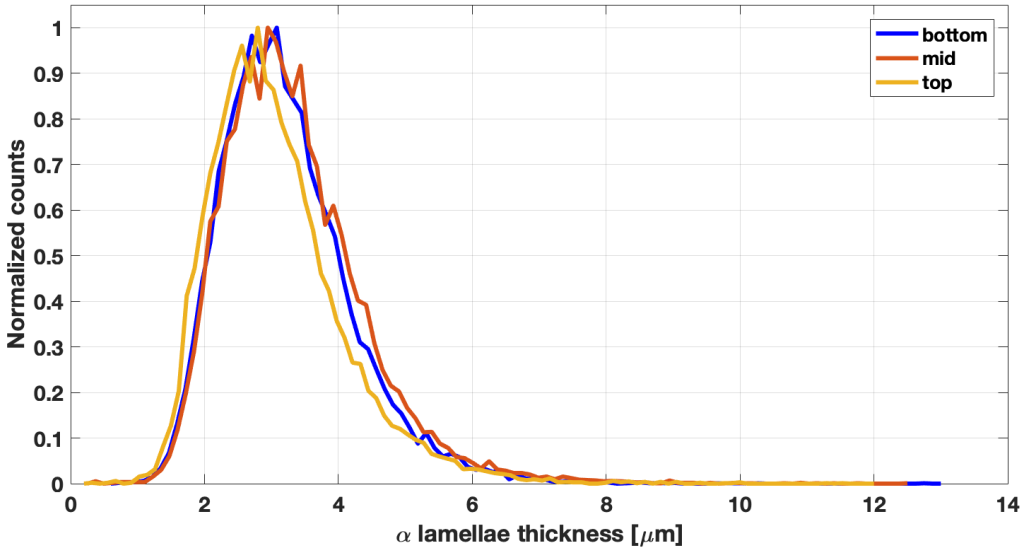

Figure *40*: Lamellae thickness distribution for bottom mid and top section of A3bK1.

Table *12* imply that the post-processing does not affect the variation trend of α-lamellae thicknesses with building height, as previously explained.

4.1.1.5 Comparison of microstructures for A3K1, A3bK1 and A3bK85

All components have a different processing history, hence it is essential to understand the influence of the different process parameters on the mechanical performance by comparing the microstructures of the components. A comparison of lamellae thickness distributions is given in Figure 41. Table 13 and Figure 42 summarize the overall α-lamellae thicknesses in each component and directly compare the influence of the respective processing history.

Table 13: Summary of average α-lamellae thicknesses in A3K1, A3bK1 and A3bK85.

	A3K1	**A3bK1**	**A3bK85**
Max [µm]	3.674	3.031	12.750
Min [µm]	0.065	0.233	0.235
Mean [µm]	0.889	0.949	3.159
Std dev [µm]	0.252	0.272	1.016

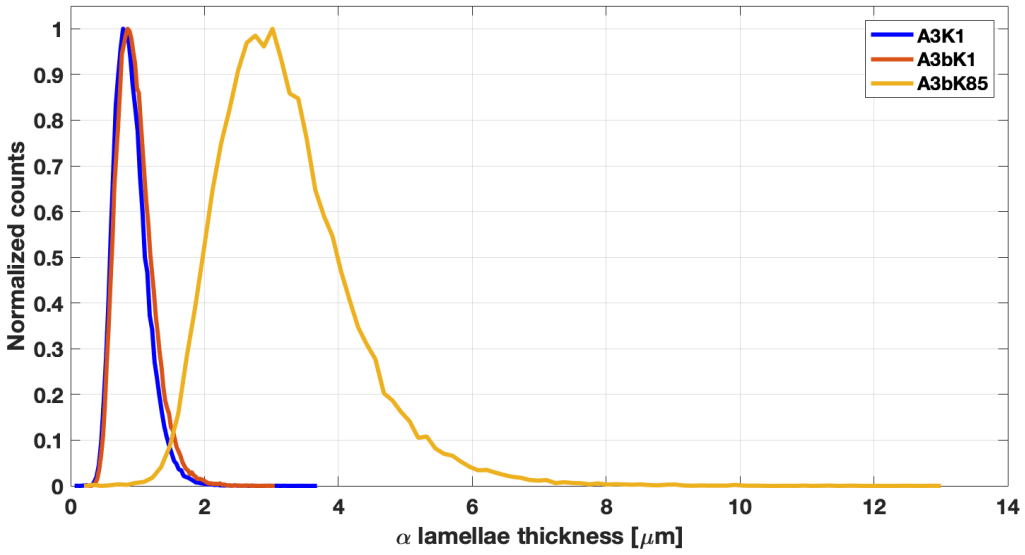

Figure 41: Comparison of lamellae thickness distributions for A3K1, A3bK1 and A3bK85.

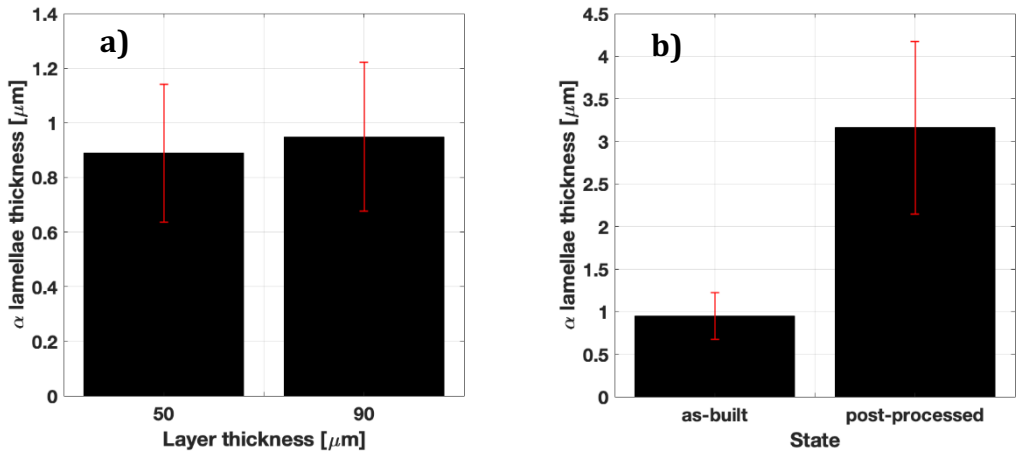

Figure 42: Comparison of average α-lamellae thickness for a) different layer thicknesses in the as-built condition and b) for different states of the component at constant layer thickness of 90 μm.

Table 13 and Figure 42a exhibit a slight increase for α-lamellae thickness by 0.06 μm when increasing the layer thickness from 50 μm to 90 μm. The distribution of the A3K1 is slightly shifted to lower lamellae thicknesses compared to the ones for A3bK1. The trend is reliable despite of the large standard deviations. The heterogeneity in both components is approximately the same when comparing the standard deviations and the width of the distributions. This trend can be explained as follows. It was stated earlier that the beam parameters were tuned to match the respective layer thickness. Hence the melt pools during the printing of the A3K1 were smaller than the ones of the A3bK1. Smaller melt pools are cooled faster which leads to a finer microstructure. It must be highlighted that builds with smaller layer thicknesses take more time to complete the build because of more layers to print. However, the solidification of the melt pool in both builds is sufficiently fast not to affect the overall build time. It is estimated by Arcam that the processing of the A3K1 took 2.4 times longer than that of the A3bK1. A longer processing time then means a longer exposure to the elevated temperatures in the building chamber. However, the results imply this effect is compensated by higher cooling rates of the melt pools, otherwise the A3bK1 would have exhibited the finer microstructure.

Table 13, Figure 41 and Figure 42b demonstrate that the lamellae thickness is more than tripled after the post-processing and the distribution for the A3bK85 is significantly shifted to higher thicknesses. Furthermore, significantly increased standard deviations and widths of the distribution indicate a stronger heterogeneity in the A3bK85. The microstructure is coarsened by the additional thermal energy acting on the crystal during the HIP and the heat treatment. The larger heterogeneity might be explained by two generations of α-lamellae. One was already formed during the printing process and the second one resulted from the martensitic decomposition during the post-processing. The first generation would be coarser than the second one and a larger spread of lamellae thicknesses is achieved. However, if this effect is significant, a distribution with two local maxima would be visible. Furthermore, when the relative standard deviations are calculated, using standard deviation divided by the corresponding mean value, the results are 0.272μm/0.949μm=0.286 for the A3bK1 and 1.016μm/3.159μm=0.322 for the

A3bK85. By comparing these results, the relative standard deviation is still higher for the latter one, but not as significant as before. It could be concluded that the comparatively large width of the distribution for the A3bK85 is just an effect arising from the large lamellae thicknesses itself.

4.1.2 Hardness

4.1.2.1 Hardness of A3K1 (50µm; as-build)

In Figure 43 the change in hardness with increasing build height is exhibited for the A3K1. The highest mean hardness of 350.25 ± 4.69 HV was obtained next to the build plate and the lowest mean hardness of 342.0 ± 4.29 HV in the mid-section of the component. At the highest build height, a mean hardness of 344.05 ± 4.31 HV was obtained. The results show no clear trend of change in hardness with increasing build height.

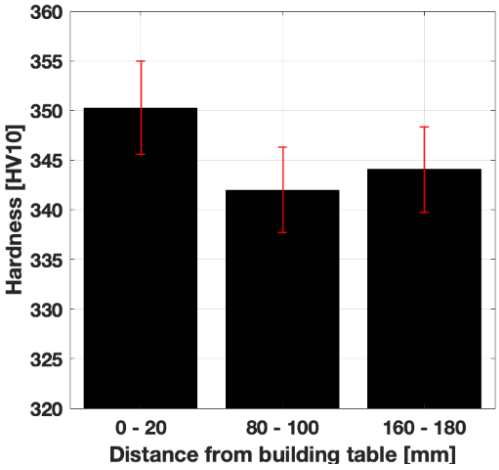

Figure 43: Change of hardness with increasing build height in A3K1.

One of the decisive microstructural parameters for the hardness of the material is the α-lamellae thickness since thinner lamellae means more α-β-interfaces acting as obstacles for moving dislocations. For all three components the highest lamellae thickness was found in the mid-section and the lowest in the top-section. This explains the smallest hardness in the mid-section. Significantly higher hardness for the section next to the building table indicates that the lamellae thickness is not the only important factor. As stated previously, martensite might be present in the microstructure. High cooling rates and less heat accumulation at the section next to the building table might make the decomposition of martensite less favorable and retain more martensite, which increases the hardness. The longer holding time at the chamber temperature could have had a minor effect on the martensitic decomposition. However, the technique to quantify the phase fraction of martensite still has to be found. Other factors influencing the hardness might be grain size, colony size or concentration of solid solution strengtheners. These parameters and their change along the building height were not investigated in this work. The fraction of the massive phase might also be a hardness determining factor. If they are in fact excessively coarsened lamellae or globalized α, they might be the weak points and hence decrease the resistance to plastic deformation resulting in a lower hardness. One further explanation could be that in the bottom section less pores were in the area of the indentations which then also results in higher hardness. On the other hand in 4.1.3.1 the highest porosity was found next to the building plate which increases the probability of hitting a pore and in this context a lower hardness is expected. Further investigation is necessary to answer the hardness variation.

4.1.2.2 Hardness of A3bK1 (90µm; as-build)

In Figure 44 the change in hardness with increasing build height is plotted for the A3bK1. The highest mean hardness of 337.80 ± 4.17 HV was found next to the build plate and the lowest mean hardness of 335.44 ± 3.72 HV in the top-section of the component. In the mid-section a mean hardness of 336.05 ± 5.68 HV was obtained. The results indicate a decrease in hardness with increasing build height. The same discussion as for the A3K1 can be done for these results.

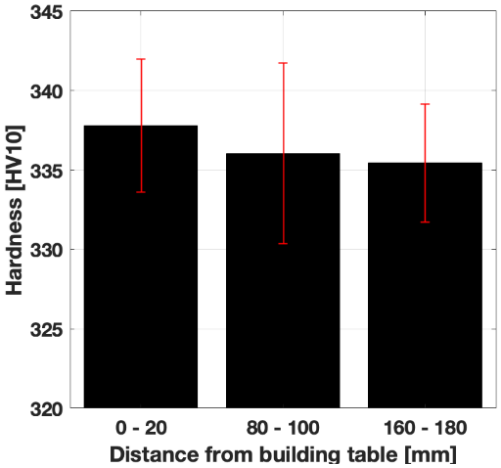

Figure 44: Change of hardness with increasing build height in A3bK1.

4.1.2.3 Hardness of A3bK85 (90µm; post-processed)

In Figure 45 the change in hardness with increasing build height for the A3bK85 is shown. The highest mean hardness of 323.81 ± 4.63 HV was obtained in the mid-section and the lowest mean hardness of 321.53 ± 4.24 HV next to the build plate. In the top-section a mean hardness of 323.06 ± 3.72 HV was obtained. Same as for the A3K1 and the A3bK1, there is no clear correlation between hardness and lamellae thickness. The same discussions as for the components above is valid here except the influence of martensite, since no needles were observed in the microstructure.

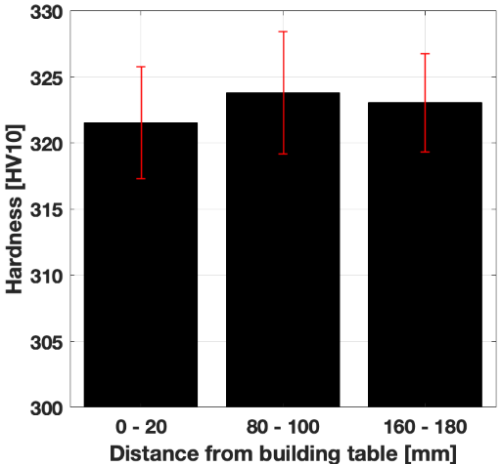

Figure 45: Change of hardness with increasing build height in A3bK85.

4.1.2.4 Comparison of hardness for A3K1, A3bK1 and A3bK85

The change in hardness with different processing history is illustrated in Figure 46. To do so, an average of the mean hardness from three locations (top, middle, bottom) within a component was calculated. The hardness decreases with increasing layer thickness from 345.43 ± 5.64 HV to 336.43 ± 4.67 HV in the as-built condition, and decreases from 336.43 ± 4.67 HV to 322.80 ± 4.29 HV after post-processing.

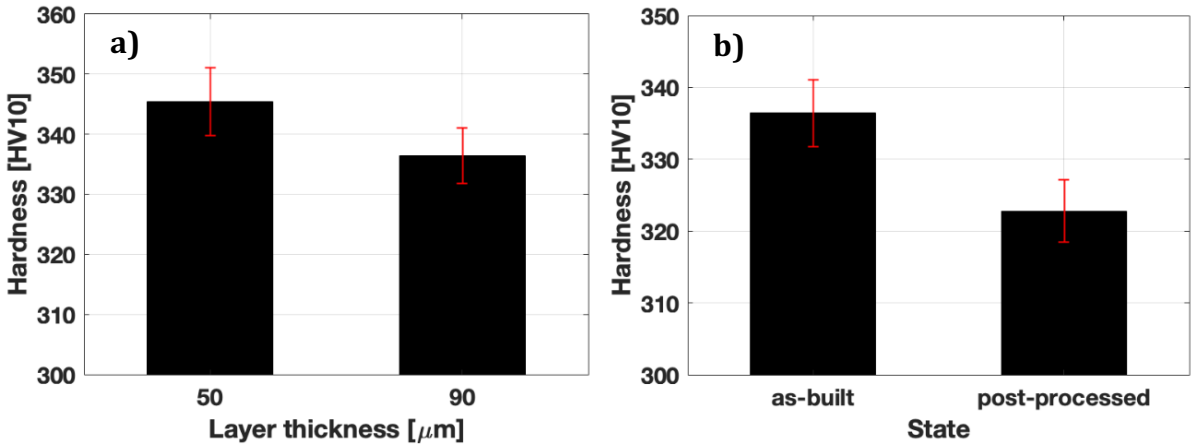

Figure 46: Comparison of hardness for a) different layer thicknesses and b) for different states of the component at constant layer thickness of 90 µm.

Both the decrease in hardness with increasing layer thick and the decrease in hardness after post-processing can be correlated to the lamellae thickness in the respective component (see Figure 42). However, as indicated in the previous sections for the single components other factors might also affect the hardness. It should be mentioned that for each component the average hardness was calculated from $3 \times 64 = 192$ indentations resulting in comparatively good statistics in terms of scattering.

4.1.3 Porosity

Three different types of porosity were found in the microstructures. They are lack of fusion, gas pores from EBM and gas pores from powder manufacturing. The observed lack of fusions in Figure 47a had an approximate length ranging from 50 to 200 µm. The size of gas pores presented in Figure 47b & c were between 8 to 100 µm for the ones generated during EBM and below 2 µm for the ones induced during powder manufacturing.

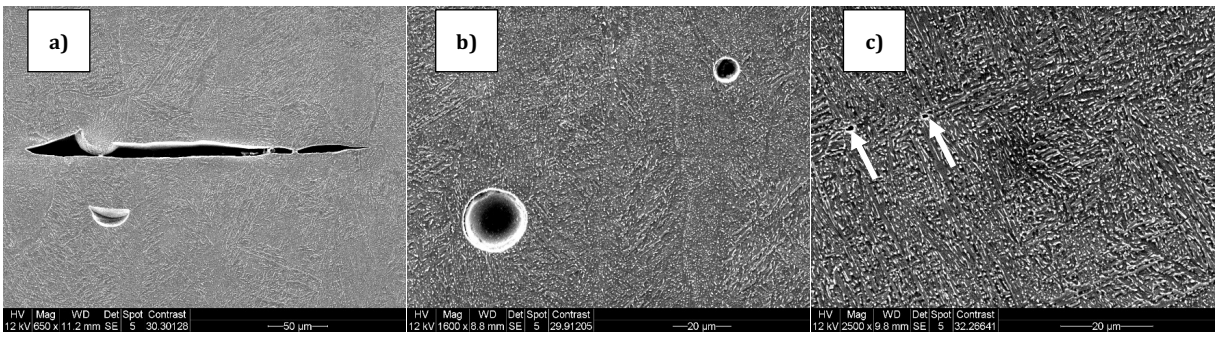

Figure 47: ESEM images of different types of porosity: a) lack of fusion, b) gas pores from EBM and c) gas pores from powder manufacturing. The exemplary images were taken from A3K1.

4.1.3.1 Porosity of A3K1 (50µm; as-built)

The change of porosity with increasing build height for the A3K1 is illustrated in Figure 48a and the OM images, where the porosities were determined from, are given in Appendix 8. The highest porosity was found next to the build plate with 0.129 % and the lowest in the mid-section with 0.108 %. The top-section exhibits a porosity of 0.126 %. No clear trend for change of porosity with increasing build height can be observed. For the closure of pores diffusion processes have to be activated which requires either high pressures or high temperatures. It seems the temperatures in the component were not high enough to clearly affect its porosity and the results are of random nature.

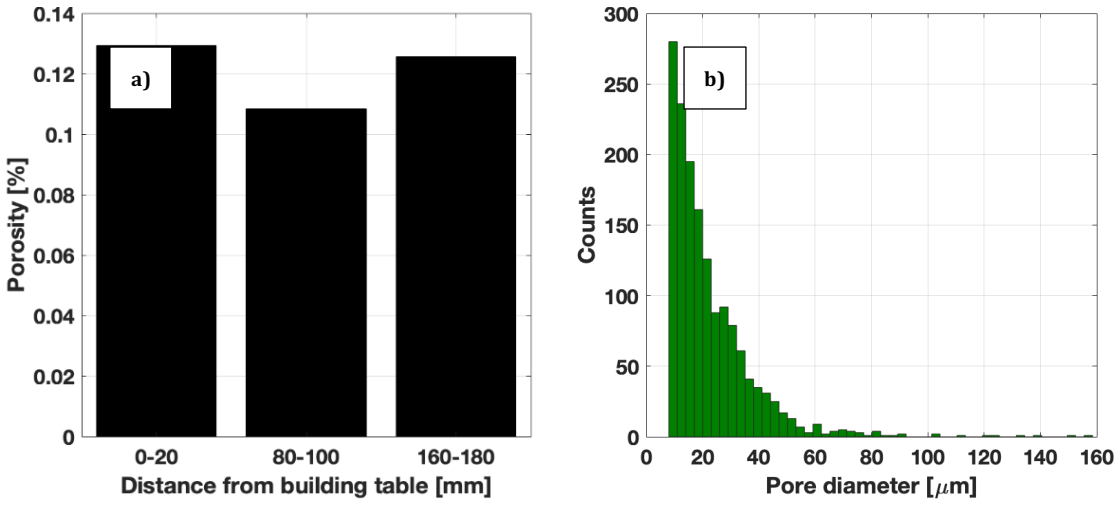

Figure 48: a) Change of porosity with increasing build height and b) the pore size histogram of all three locations in A3K1.

In Figure 48b the pore size histogram for the A3K1 is plotted. The maximum detected pore size is 158.52 μm and most of the pores have a diameter ranging from 8 μm to 40 μm indicating that the majority of the pores are gas pores. This conclusion was supported by the OM images in Appendix 8. The average pore size is 22.62 μm. The true pore diameters in some cases might be higher since the spherical approximation was taken during the pore size determination as stated in 3.3.3. During SEM investigations as well as the OM images in Appendix 8 all three types of pores could be detected, whereas the majority of the pores was spherical. The observation of lack of fusion pores indicate that in some regions the powder layer was not sufficiently melted. Hence the true melt pool depth can have strong variations from the theoretical ones with a depth of four layers. Lack of fusion pores are generally an indication for non-optimum processing parameters. To fully avoid this pore type either the electron beam scan speed must be reduced, the beam power increased or the EBM machine improved to avoid inconsistencies in beam parameters. Another option could be to reduce the powder layer thickness while keeping the beam parameters constant.

The number of gas pores established during the EBM could also be diminished by using optimized process parameters. For example, the powder flowability could be increased allowing a higher powder packing density. The vacuum in the building chamber might be improved even more to reduce the amount of gas solved in the melt. The pores arising from powder manufacturing are not discussed in this work.

4.1.3.2 Porosity of A3bK1 (90μm; as-built)

In Figure 49a the change of porosity with increasing build height for the A3bK1 is presented and the corresponding OM images are shown in Appendix 9. The maximum porosity of 0.154 % was found in the mid-section and the lowest one of 0.096 % in the top-section. The bottom section next to the build plate has a porosity of 0.104 %. Same as for the A3K1, no clear trend for change of porosity with increasing build height can be observed.

In Figure 49b the pore size distribution for the A3bK1 is given. The maximum detected pore size is 117.12 μm, however this value could be even higher considering the spherical approximation. The average pore size is 26.61 μm. The majority of the pores exhibits a diameter ranging from 8 μm to 50 μm and was spherical as seen in Appendix 9. Lack of fusions could be again observed frequently by OM and SEM.

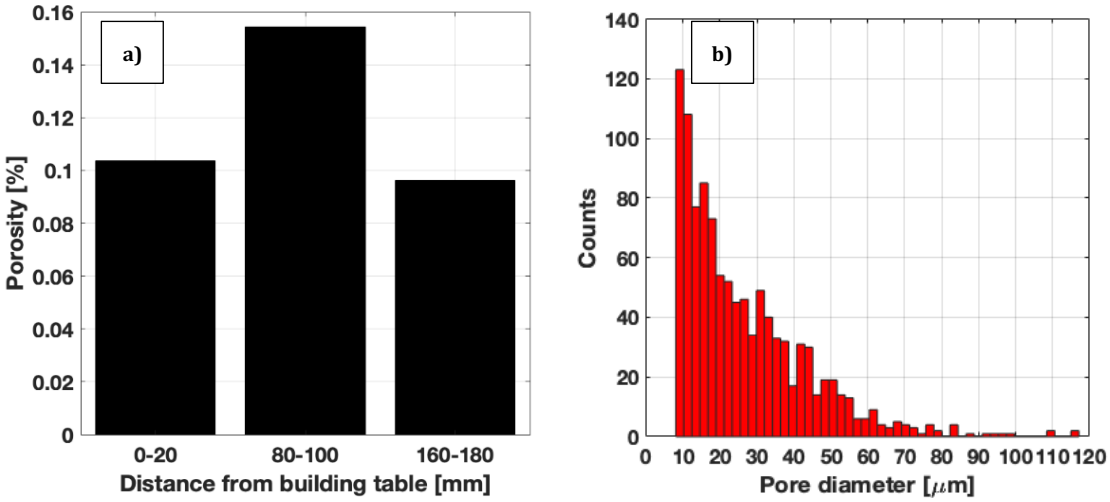

Figure 49: a) Change of porosity with increasing build height and b) the pore size histogram of all three locations in A3bK1.

4.1.3.3 Porosity of A3bK85 (90μm; post-processed)

The influence of build height on the porosity of A3bK85 is depicted in Figure 50a and the OM images where the results were taken from are presented in Appendix 10. The lowest porosity of 0.00150 % was found in the top-section and the highest one in the mid-section with 0.00437 %. The bottom-section was measured to have a porosity of 0.00353 %. Same as for the as-built components, no trend for change in porosity with increasing build height is evident and the differences might be of random nature. However in this case, the highest porosity in the mid-section could be explained by a weak point of all common pressing methods. The pressure next to the pressuring medium like pistons or in this case the gas is higher than in the center of the workpiece. Consequently, on the top or at the bottom of the printed component the pressure parallel to the building direction is higher than the one acting on the mid-section which is more far away from the pressurized gas pushing along this axis. The pressure perpendicular to the building direction should be the same for every section in the bar. Then the mid-section experienced a smaller total pressure and hence less pores are closed.

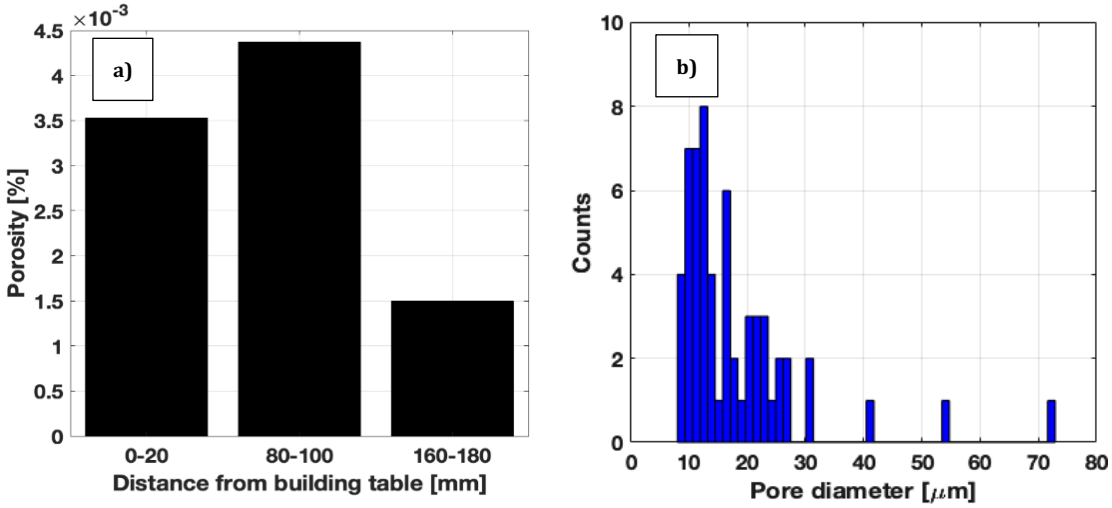

Figure 50: a) Change of porosity with increasing build height and b) the pore size histogram of all three locations in A3bK85.

The pore size histogram of A3bK85 is displayed in Figure 50b. Compared to the as-built samples the number of counts is significantly less. The maximum detected pore size is 72.90 µm and the most probable pore diameters were detected between 8 and 28 µm. The average pore size is 18.72 µm. No lack of fusions were observed in the OM images in Appendix 10 showing that the HIP closed all this type of pores. Only spherical pores are left. This might be explained by a larger curvature on the sides of lack of fusion pores compared to spherical ones, which increases the driving force for diffusion.

The results above indicate that the HIP clearly reduced the component's porosity and pore sizes, but a few relatively large pores are left. By increasing the time, temperature or pressure of the HIP all the pores might be closed.

4.1.3.4 Comparison of porosity for A3K1, A3bK1 and A3bK85

In this section a mean porosity from all three locations (top, middle, bottom) within a component was calculated and compared as illustrated in Figure 51. The average porosity is slightly decreasing with increasing layer thickness from 0.121 ± 0.0111 % to 0.118 ± 0.0317 %. However, when the large error bars are considered, no trend might be indicated. As already discussed in the porosity sections, the differences in temperatures and cooling rates in the chamber are not strong enough to affect the porosity. If the beam power for both builds was the same without compensating the larger layer thicknesses, the porosity of the A3bK1 would have been larger, but in the current case the energy input per volume was the same. During the post-processing the porosity significantly decreases from 0.118 ± 0.0317 % to 0.00313 ± 0.00147 %, indicating again the effect of the pore closure during the HIP.

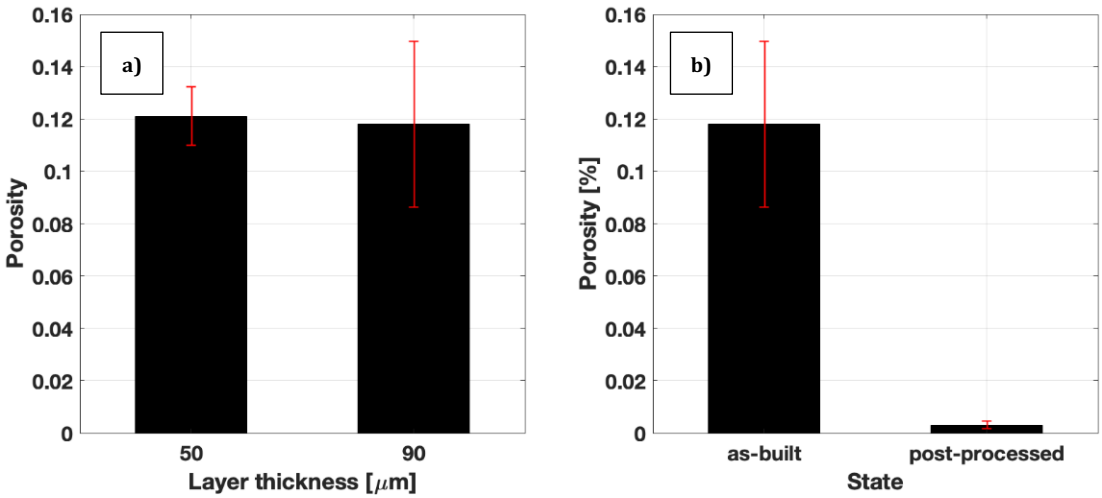

Figure 51: Comparison of porosity for a) different layer thicknesses and b) different states of the component at constant layer thickness of 90 µm.

4.2 Virgin and cycled powders

4.2.1 Virgin (new powder)

In Figure 52 and Figure 53 the microstructure of virgin powder particles is presented. Figure 52 exhibits spherical pores with a size of about 2 µm indicating gas pores induced during the powder manufacturing as explained in 2.2.3. The only microstructural feature which could be clearly detected was sharp needles following the Burgers-relationship. The widths are in the range of 0.15 µm to 0.80 µm and the lengths are between 3.5 µm and 32 µm. The needles look exactly like acicular martensite which was expected in the virgin powder. During the powder manufacturing the pre-alloyed material is atomized and the fine droplets are then rapidly cooled due to their small size. The high cooling rates then form martensite.

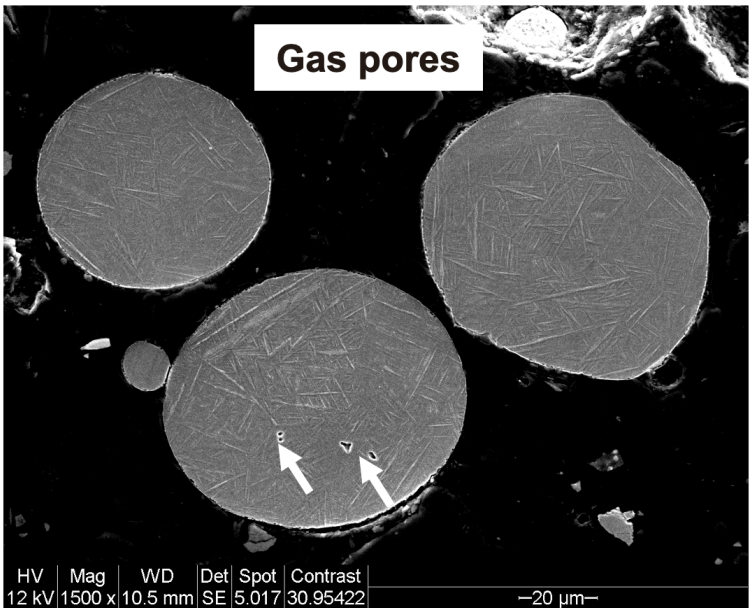

Figure 52: ESEM image of virgin powder particles and their microstructure.

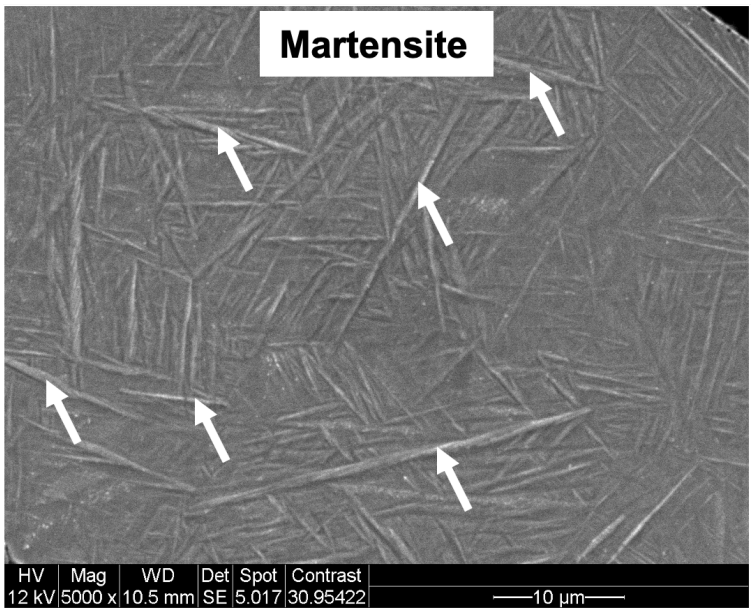

Figure 53: ESEM image of the virgin powder's microstructure.

4.2.2 A13C1 (cycled once)

In Figure 54 and Figure 55 the microstructure of powder particles after cycling once is shown. A significantly different microstructure compared to that of the virgin powder is observed. Same microstructural features as the as-build components A3K1 and A3bK1 are found including retained β, massive phase, grain boundary α, basket-weave α, colony α, bulges and martensite. Grains are depicted by grain boundary α layers. These microstructural features are either formed during the printing of the cubes or during exposure to the chamber temperatures when cycling. The needles in the microstructure have an approximate size from 0.4 to 0.8 μm which is in the range of the martensite established in the virgin powder. Hence it is again concluded that they are martensite, which further supports the existence of martensite in the as-built components A3K1 and A3bK1.

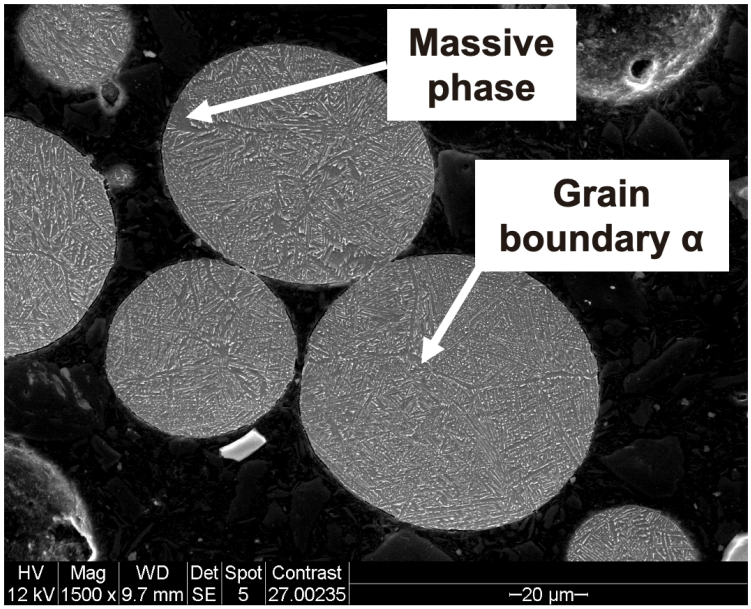

Figure 54: ESEM image of A13C1 powder particles and their microstructure.

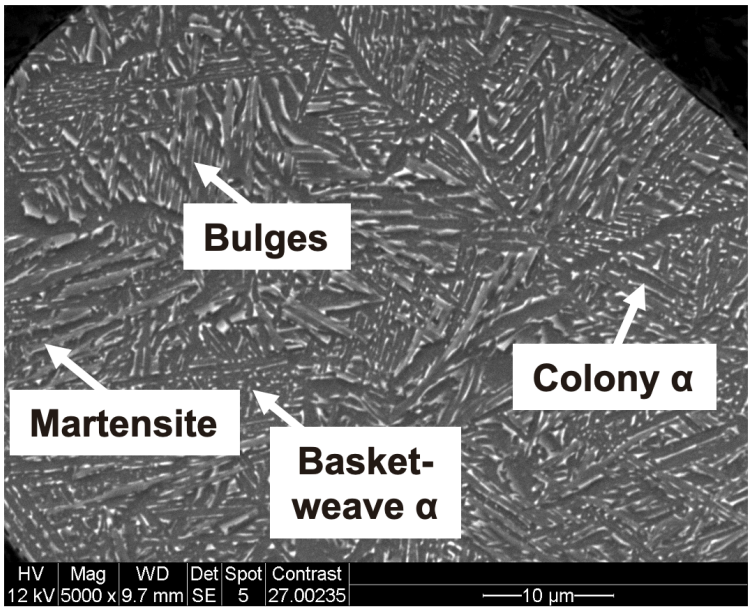

Figure 55: ESEM image of the A13C1 powder's microstructure.

4.2.3 A17C1 (cycled five times)

In Figure 56 and Figure 57 the powder particles and the microstructure of the A17C1 sample is illustrated. There are no significant differences visible with respect to the A13C1 powder. Needles are still frequently observed after five times cycling. The observations indicate that the microstructural features are less affected by longer exposure to the chamber temperature. This would mean the features in the as-built components are established during the cooling from the last re-melting or subsequently during the heat transfer from the re-melted layers above. It is not due to the exposure to the chamber temperatures of about 500 °C.

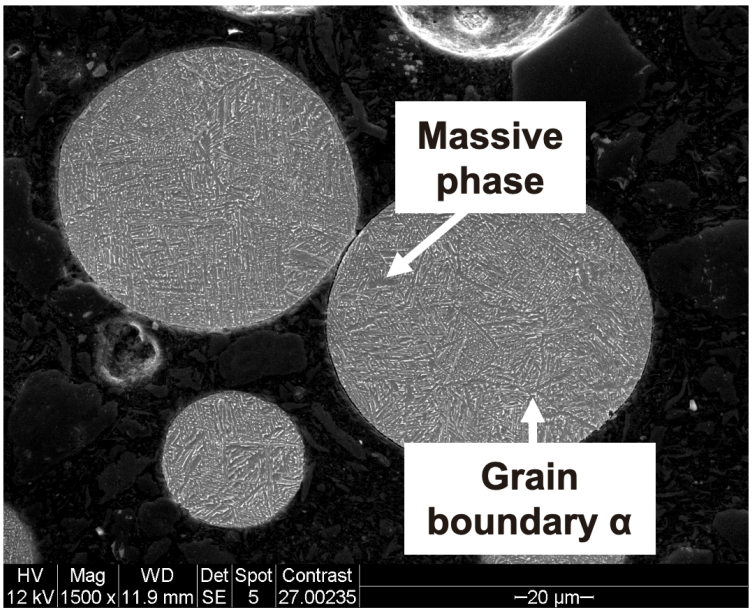

Figure 56: ESEM image of A17C1 powder particles and their microstructure.

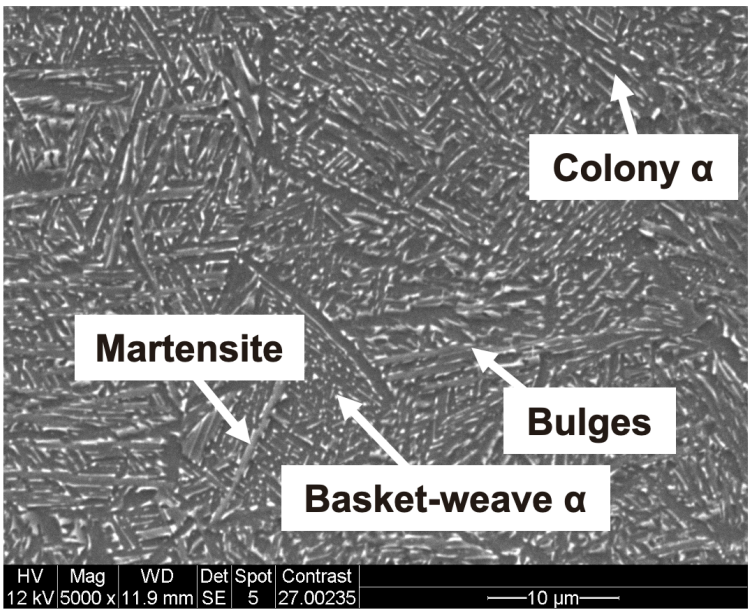

Figure 57: ESEM image of the A17C1 powder's microstructure.

4.2.4 A22C1 (cycled ten times)

Same as for the A17C1 the microstructure of the A22C1 powder which has been cycled ten times does not differ from the ones of the A13C1 as presented in Figure 58 and Figure 59. Grains are depicted by continuous grain boundary α layers and the features are the same as in the as-built components. Again, these micrographs suggest the microstructural features are already established during the printing of the cubes and not during the exposure to the chamber temperatures of about 500 °C.

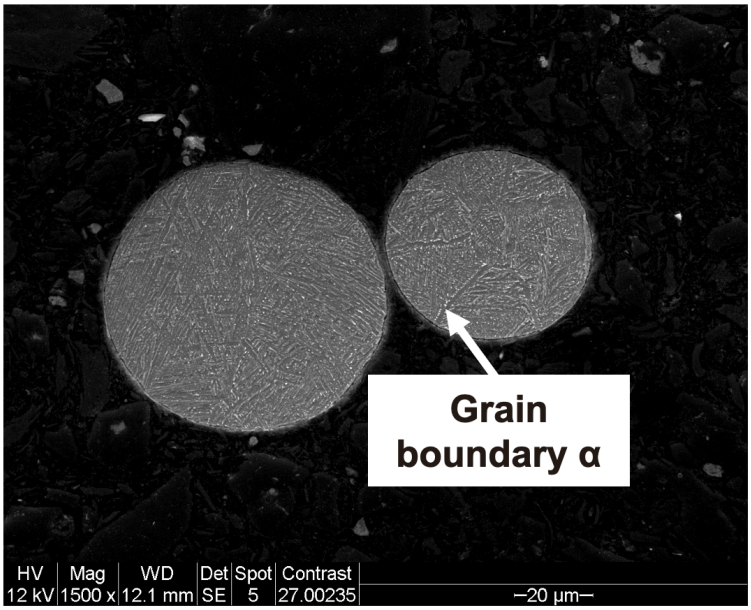

Figure 58: ESEM image of A22C1 powder particles and their microstructure.

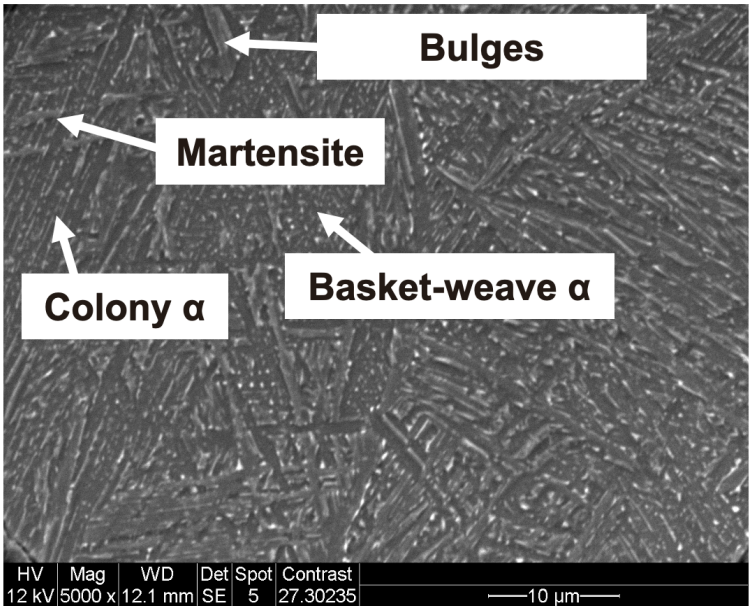

Figure 59: ESEM image of the A22C1 powder's microstructure.

As in the virgin powder, in all the semi-sintered powders gas pores with a size of approximately 2 µm are visible. For the A22C1 powder, as shown in Figure 60, pores are still present even after ten times exposure to the chamber temperatures. This observations support the discussions in 4.1.3 that the chamber temperature is not high

enough to close any pores and hence exposure time or differences in cooling rates have no influence on the porosity.

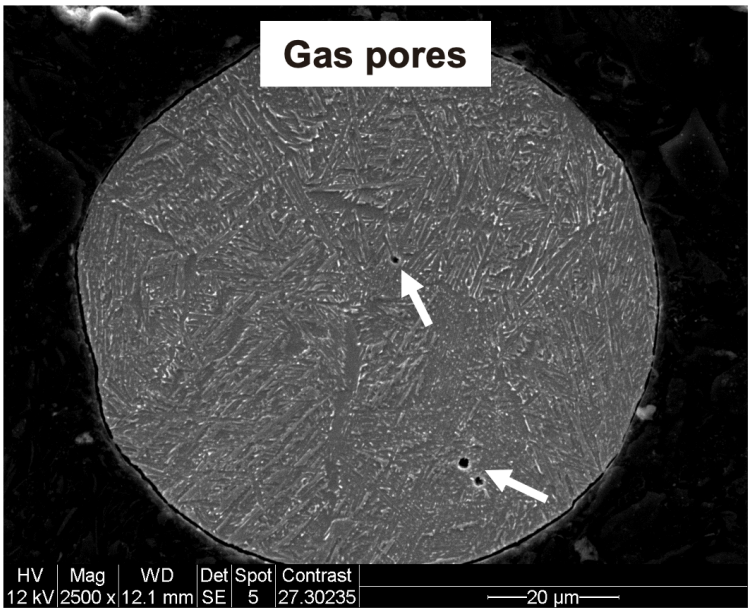

Figure 60: ESEM image of gas pores in A22C1 powder particle.

5 Summary

This thesis was aimed to further understand how the complex thermal history affects the microstructure, porosity and hardness of EBM fabricated Ti-6Al-4V components with different processing parameters. To do so, three components in shape of bars were investigated at different building heights. Two of them were in the as-built state with a layer thickness of 50 μm and 90 μm, respectively. The third component was printed with a 90 μm layer thickness and then post-processed.

Parallel to the building direction of all samples, the OM images presented an elongated grain structure and no significant difference between the samples were observed at low magnification. The grain width varied from 30 to 240 μm and their length was about several millimeters. The microstructure of the as-built samples with different layer thickness was similar. Both exhibited a fine and heterogeneous lamellar microstructure consisting of the α- and β-phase. The observed α-phase morphologies were colony α, basket-weave α, α at the boundaries of the former β-grains, massive α phase and α-bulges. The last two morphologies are not fully understood, but EDS characterization indicates they are probably α-phase. Beside the α and β phase, acicular martensite was also present in the microstructures. Post-processing makes the microstructure significantly coarser with similar features as the as-built samples except that the martensite disappeared. Instead, α-twins were observed. No oxides or nitrides could be found in the microstructures of all components. By the use of high-resolution SEM imaging fine nano-sized particles which might be Ti_3Al precipitates were observed in the α-phase of all three components. Their existence is reasonable, but the available techniques were not enough to fully characterize them.

By means of an image analysis software the α-lamellae thickness in different building heights was measured. For all three components the thickness is first increases from the bottom to the mid-section and then decreases again from the mid- towards the top section. The results are summarized in Table 14. This trend was explained by two competing mechanisms. Both exposure time and cooling rate decrease with increasing building height. The α-lamellae thickness depends on which factor is dominant. Furthermore, the results in Table 14 indicate that the α-lamellae thickness is slightly increasing with increasing layer thickness. Post-processing makes this value increase significantly.

Table 14: α-lamellae thicknesses at different building heights and the average for the entire component.

	50μm; as-built	**90μm; as-built**	**90μm; HIP+HT**
Bottom	0.875±0.235 μm	0.941±0.263 μm	3.168±0.973 μm
Mid	0.925±0.255 μm	1.002±0.288 μm	3.273±1.056 μm
Top	0.871±0.261 μm	0.913±0.260 μm	3.014±0.999 μm
Average	0.889±0.252 μm	0.949±0.272 μm	3.159±1.016 μm

Table 15: Average porosity for all three components.

	50μm; as-built	**90μm; as-built**	**90μm; HIP+HT**
Average porosity	0.118 ± 0.0317 %	0.121 ± 0.0111 %	0.00313 ± 0.00147 %

Regarding porosity there was no clear correlation with the building height and the layer thicknesses. Hence average porosities of the entire components are given in Table 15. The effect of the HIP on the porosity is evident and significant reduction is observed. In the as-built samples lack of fusion pores were observed which implies that the beam parameters were not completely optimized.

Similar to the porosity, the hardness of the components showed no clear trend with increasing building height, but the average hardness presented meaningful differences between the components, as listed in Table 16. There is a decrease in hardness with increasing layer thickness or when the component is post-processed. These differences can be correlated to the α-lamellae thicknesses and the Hall-Petch effect.

Table 16: Average hardness for all three components.

	50μm; as-built	**90μm; as-built**	**90μm; HIP+HT**
Average hardness	345.43 ± 5.64 HV	336.43 ± 4.67 HV	322.80 ± 4.29 HV

Another objective of this project was the effect of cycling (up to 10 times) in EBM on the microstructure of Ti-6Al-4V powder. Virgin powder exhibited a fully martensitic microstructure and small gas pores generated during the powder manufacturing. The porosity remained the same after cycling. However the microstructure was transformed completely after the first cycling, producing a microstructure similar to the ones of the as-built components with all characteristic features. No significant change in porosity and microstructure with increasing cycling numbers was found.

6 Future work

This project was planned to be finished within 20 weeks and hence a limited time frame was available. Also, the resources for the experiments were limited due to the corona pandemic.

In the future, further understanding of the effect of EBM on the microstructure of Ti-6Al-4V and full characterization of all the features found in the microstructure are of interest. First, all parts of the bar shaped components could be analyzed and not only the three sections at different building heights. Second, high energy X-ray diffraction (XRD) could be conducted to resolve the diffraction peaks of all different phases in the microstructure to check the possible existence of Ti_3Al and to further characterize the martensite. The problem with conventional XRD is peak overlapping of the martensite and the α-phase as well as too small Ti_3Al peaks compared to the background. Furthermore, the microstructures could be analyzed by means of transmission electron microscopy to confirm if nano-sized Ti_3Al precipitates have established during the EBM process. Additionally, electron beam backscatter diffraction (EBSD) could be performed to examine the exact grain sizes and the texture of the microstructures since they also affect the mechanical properties. In this work the image analysis methods limited the possibilities of quantitative microstructural analysis. For example, it was difficult to obtain the information of the phase fractions in the as-built samples for the needles and the two titanium allotropes. Hence new softwares or techniques could be tested. From the mechanical performance point of view, since the hardness only gives a rough overview, the EBM fabricated Ti-6Al-4V components could be tensile and fatigue tested. In addition, nano- or micro indentation could be performed to understand the contribution of different microstructural features on the overall hardness of the component.

7 Remarks

Beside all the limitations, meaningful results were achieved in this work. The examination of the components shows that there is nothing such as a “perfect” processing history for EBM fabricated Ti-6Al-4V components. It is always a trade-off between all the processing parameters and the respective requirements. The higher the layer thickness, the higher the production speed. However, the hardness and hence the strength decreases. The porosity seems to have a minor effect on the hardness, but several other mechanical properties such as ductility and fatigue performance are reduced. Thus, for a more predictable mechanical performance like for the fittings of OGV’s in jet engines, the porosity must be diminished or even completely removed. The applied HIP clearly reduced the porosity on the cost of the hardness of the component.
The analysis of the powders exhibited that the EBM chamber temperatures itself have a negligible effect on the formation of microstructural features and the closure of pores.

8 References

[1] L. E. Murr *et al.*, "Metal Fabrication by Additive Manufacturing Using Laser and Electron Beam Melting Technologies," *J. Mater. Sci. Technol.*, vol. 28, no. 1, pp. 1–14, 2012, doi: 10.1016/S1005-0302(12)60016-4.

[2] V. V. Popov, A. Katz-Demyanetz, A. Garkun, and M. Bamberger, "The effect of powder recycling on the mechanical properties and microstructure of electron beam melted Ti-6Al-4 V specimens," *Addit. Manuf.*, vol. 22, no. June, pp. 834–843, 2018, doi: 10.1016/j.addma.2018.06.003.

[3] A. Strondl, O. Lyckfeldt, H. Brodin, and U. Ackelid, "Characterization and Control of Powder Properties for Additive Manufacturing," *Jom*, vol. 67, no. 3, pp. 549–554, 2015, doi: 10.1007/s11837-015-1304-0.

[4] X. Gong, T. Anderson, and K. Chou, "Review on powder-based electron beam additive manufacturing Technology," *Manuf. Rev.*, vol. 1, pp. 1–9, 2014, doi: 10.1051/mfreview/2014001.

[5] V. Petrovic and R. Niñerola, "Powder recyclability in electron beam melting for aeronautical use," *Aircr. Eng. Aerosp. Technol.*, vol. 87, no. 2, pp. 147–155, 2015, doi: 10.1108/AEAT-11-2013-0212.

[6] S. Liu and Y. C. Shin, "Additive manufacturing of Ti6Al4V alloy: A review," *Mater. Des.*, vol. 164, p. 107552, 2019, doi: 10.1016/j.matdes.2018.107552.

[7] M. T. Whittaker, *Titanium alloys*, vol. 5, no. 3. 2015.

[8] L. Wagner and M. Wollmann, *Titanium and Titanium Alloys*. 2013.

[9] Bhaskar Dutta, *Additive Manufacturing of Titanium Alloys Additive Manufacturing of Titanium Alloys State of the Art , Challenges , and Opportunities*. 2014.

[10] S. Sun and W. Lv, "Microstructure and mechanical properties of TC18 titanium alloy," *Xiyou Jinshu Cailiao Yu Gongcheng/Rare Met. Mater. Eng.*, vol. 45, no. 5, pp. 1138–1141, 2016, doi: 10.1142/9789812793959_0001.

[11] W. H. Lee *et al.*, "Self-consolidation mechanism of porous TI-6AL-4V implant prototypes produced by electro-discharge-sintering of spherical TI-6AL-4V powders," *Arch. Metall. Mater.*, vol. 60, no. 2, pp. 1185–1189, 2015, doi: 10.1515/amm-2015-0094.

[12] L. Parry, I. A. Ashcroft, and R. D. Wildman, "Understanding the effect of laser scan strategy on residual stress in selective laser melting through thermo-mechanical simulation," *Addit. Manuf.*, vol. 12, pp. 1–15, 2016, doi: 10.1016/j.addma.2016.05.014.

[13] G. Davenport, "1 Introduction," *Remote Sens. Technol. Forensic Investig.*, pp. 1–4, 2017, doi: 10.1201/9781315186573-2.

[14] T. Ahmed and H. J. Rack, "Phase transformations during cooling in α + β titanium alloys," *Mater. Sci. Eng. A*, vol. 243, no. 1–2, pp. 206–211, 1998, doi: 10.1016/s0921-5093(97)00802-2.

[15] E. Hancock, W. Smith, R. Wilson, and A. Bors, "Lecture Notes in Computer Science (including subseries Lecture Notes in Artificial Intelligence and Lecture Notes in Bioinformatics): Preface," *Lect. Notes Comput. Sci. (including Subser. Lect. Notes Artif. Intell. Lect. Notes Bioinformatics)*, vol. 8048 LNCS, no. PART 2, 2013, doi: 10.1007/978-3-642-40246-3.

[16] I. Katzarov, S. Malinov, and W. Sha, "Finite element modeling of the morphology of β to α phase transformation in Ti-6Al-4V alloy," *Metall. Mater. Trans. A Phys. Metall. Mater. Sci.*, vol. 33, no. 4, pp. 1027–1040, 2002, doi: 10.1007/s11661-002-0204-4.

[17] R. Pederson, F. Niklasson, F. Skystedt, and R. Warren, "Microstructure and mechanical properties of friction- and electron-beam welded Ti-6Al-4V and Ti-

6Al-2Sn-4Zr-6Mo," *Mater. Sci. Eng. A*, vol. 552, no. April 2018, pp. 555–565, 2012, doi: 10.1016/j.msea.2012.05.087.
[18] M. Neikter, *Microstructure and texture of additive manufactured Ti-6Al-4V*. 2017.
[19] H. K. Rafi, N. V. Karthik, H. Gong, T. L. Starr, and B. E. Stucker, "Microstructures and mechanical properties of Ti6Al4V parts fabricated by selective laser melting and electron beam melting," *J. Mater. Eng. Perform.*, vol. 22, no. 12, pp. 3872–3883, 2013, doi: 10.1007/s11665-013-0658-0.
[20] F. X. Gil Mur, D. Rodríguez, and J. A. Planell, "Influence of tempering temperature and time on the α′-Ti-6A1-4V martensite," *J. Alloys Compd.*, vol. 234, no. 2, pp. 287–289, 1996, doi: 10.1016/0925-8388(95)02057-8.
[21] B. Vrancken, L. Thijs, J. P. Kruth, and J. Van Humbeeck, "Heat treatment of Ti6Al4V produced by Selective Laser Melting: Microstructure and mechanical properties," *J. Alloys Compd.*, vol. 541, pp. 177–185, 2012, doi: 10.1016/j.jallcom.2012.07.022.
[22] T. Vilaro, C. Colin, and J. D. Bartout, "As-fabricated and heat-treated microstructures of the Ti-6Al-4V alloy processed by selective laser melting," *Metall. Mater. Trans. A Phys. Metall. Mater. Sci.*, vol. 42, no. 10, pp. 3190–3199, 2011, doi: 10.1007/s11661-011-0731-y.
[23] S. L. Lu, M. Qian, H. P. Tang, M. Yan, J. Wang, and D. H. StJohn, "Massive transformation in Ti-6Al-4V additively manufactured by selective electron beam melting," *Acta Mater.*, vol. 104, pp. 303–311, 2016, doi: 10.1016/j.actamat.2015.11.011.
[24] T. B. Massalski, "Massive transformations revisited," *Metall. Mater. Trans. A Phys. Metall. Mater. Sci.*, vol. 33, no. 8, pp. 2277–2283, 2002, doi: 10.1007/s11661-002-0351-7.
[25] G. Lütjering, *Titanium*, 2nd ed. 2007.
[26] H. Carreon, M. Carreon, and A. Dueñas, "Assessment of precipitates of aged Ti-6Al-4V alloy by ultrasonic attenuation," *Philos. Mag.*, vol. 97, no. 1, pp. 58–68, 2017, doi: 10.1080/14786435.2016.1244359.
[27] R. Pederson, "Microstructure and Phase Transformation of Ti-6Al-4V," 2002.
[28] R. Pederson, "The microstructures of Ti-6Al-4V and Ti-6Al-2Sn-4Zr-6Mo and their relationship to processing and properties," p. 59, 2004, doi: ISSN 1402-1544 / ISRN LTU-DT--04/19--SE / NR 2004:19.
[29] G. Z. Quan, G. C. Luo, J. T. Liang, D. Sen Wu, A. Mao, and Q. Liu, "Modelling for the dynamic recrystallization evolution of Ti-6Al-4V alloy in two-phase temperature range and a wide strain rate range," *Comput. Mater. Sci.*, vol. 97, pp. 136–147, 2015, doi: 10.1016/j.commatsci.2014.10.009.
[30] G. Gottstein, *Physikalische Grundlagen der Materialkunde*, 3rd ed. Springer.
[31] X. Tan *et al.*, "Graded microstructure and mechanical properties of additive manufactured Ti-6Al-4V via electron beam melting," *Acta Mater.*, vol. 97, pp. 1–16, 2015, doi: 10.1016/j.actamat.2015.06.036.
[32] S. Raghavan, M. L. S. Nai, P. Wang, W. J. Sin, T. Li, and J. Wei, "Heat treatment of electron beam melted (EBM) Ti-6Al-4V: microstructure to mechanical property correlations," *Rapid Prototyp. J.*, vol. 24, no. 4, pp. 774–783, 2018, doi: 10.1108/RPJ-05-2016-0070.
[33] H. P. Tang *et al.*, "Microstructure, Mechanical Properties, and Flatness of SEBM Ti-6Al-4V Sheet in As-Built and Hot Isostatically Pressed Conditions," *Jom*, vol. 69, no. 3, pp. 466–471, 2017, doi: 10.1007/s11837-016-2253-y.
[34] C. de Formanoir *et al.*, "Micromechanical behavior and thermal stability of a dual-phase α+α' titanium alloy produced by additive manufacturing," *Acta Mater.*, vol. 162, pp. 149–162, 2019, doi: 10.1016/j.actamat.2018.09.050.

[35] D. G. Lee, S. Lee, and C. S. Lee, “Quasi-static and dynamic deformation behavior of Ti-6Al-4V alloy containing fine α2-Ti3Al precipitates,” *Mater. Sci. Eng. A*, vol. 366, no. 1, pp. 25–37, 2004, doi: 10.1016/j.msea.2003.08.061.
[36] Y. Fan, W. Tian, Y. Guo, Z. Sun, and J. Xu, “Relationships among the Microstructure, Mechanical Properties, and Fatigue Behavior in Thin Ti6Al4V,” *Adv. Mater. Sci. Eng.*, vol. 2016, 2016, doi: 10.1155/2016/7278267.
[37] B. Wysocki, P. Maj, R. Sitek, J. Buhagiar, K. J. Kurzydłowski, and W. Świeszkowski, “Laser and electron beam additive manufacturing methods of fabricating titanium bone implants,” *Appl. Sci.*, vol. 7, no. 7, 2017, doi: 10.3390/app7070657.
[38] M. Koike, K. Martinez, L. Guo, G. Chahine, R. Kovacevic, and T. Okabe, “Evaluation of titanium alloy fabricated using electron beam melting system for dental applications,” *J. Mater. Process. Technol.*, vol. 211, no. 8, pp. 1400–1408, 2011, doi: 10.1016/j.jmatprotec.2011.03.013.
[39] M. F. Zäh and S. Lutzmann, “Modelling and simulation of electron beam melting,” *Prod. Eng.*, vol. 4, no. 1, pp. 15–23, 2010, doi: 10.1007/s11740-009-0197-6.
[40] H. Galarraga, D. A. Lados, R. R. Dehoff, M. M. Kirka, and P. Nandwana, “Effects of the microstructure and porosity on properties of Ti-6Al-4V ELI alloy fabricated by electron beam melting (EBM),” *Addit. Manuf.*, vol. 10, pp. 47–57, 2016, doi: 10.1016/j.addma.2016.02.003.
[41] P. Wang, X. Tan, M. L. S. Nai, S. B. Tor, and J. Wei, “Spatial and geometrical-based characterization of microstructure and microhardness for an electron beam melted Ti-6Al-4V component,” *Mater. Des.*, vol. 95, pp. 287–295, 2016, doi: 10.1016/j.matdes.2016.01.093.
[42] H. V. Atkinson and S. Davies, “Fundamental aspects of hot isostatic pressing: An overview,” *Metall. Mater. Trans. A Phys. Metall. Mater. Sci.*, vol. 31, no. 12, pp. 2981–3000, 2000, doi: 10.1007/s11661-000-0078-2.
[43] M. H. BOCANEGRA-BERNAL, “Hot Isostatic Pressing (HIP) technology and its applications to metals and ceramics,” vol. 9, pp. 6399–6420, 2004.
[44] K. Sofinowski *et al.*, “In situ characterization of a high work hardening Ti-6Al-4V prepared by electron beam melting,” *Acta Mater.*, vol. 179, pp. 224–236, 2019, doi: 10.1016/j.actamat.2019.08.037.
[45] J. Wang, H. P. Tang, K. Yang, N. Liu, L. Jia, and M. Qian, “Selective Electron Beam Manufacturing of Ti-6Al-4V Strips: Effect of Build Orientation, Columnar Grain Orientation, and Hot Isostatic Pressing on Tensile Properties,” *Jom*, vol. 70, no. 5, pp. 638–643, 2018, doi: 10.1007/s11837-018-2794-3.
[46] C. He, P. Wang, M. Ling, S. Nai, and J. Wei, “Distribution of porosity in electron beam melting additive manufactured Ti-6Al-4V component,” *Ninth Pacific Rim Int. Conf. Adv. Mater. Process.*, no. October 2019, pp. 385–387, 2016.
[47] L. Reimer, *Scanning Electron Microscopy*, 2nd ed. Springer.
[48] O. P. Choudhary and P. ka, “Scanning Electron Microscope: Advantages and Disadvantages in Imaging Components,” *Int. J. Curr. Microbiol. Appl. Sci.*, vol. 6, no. 5, pp. 1877–1882, 2017, doi: 10.20546/ijcmas.2017.605.207.
[49] W. Zhou, R. Apkarian, Z. L. Wang, and D. Joy, “Fundamentals of scanning electron microscopy (SEM),” *Scanning Microsc. Nanotechnol. Tech. Appl.*, pp. 1–40, 2007, doi: 10.1007/978-0-387-39620-0_1.
[50] R. Wang and C. Wang, *Springer Tracts in Modern Physics 272 Progress in Nanoscale Characterization and*. 2018.
[51] J. I. Goldstein, D. E. Newbury, J. R. Michael, N. W. M. Ritchie, J. H. J. Scott, and D. C. Joy, *Microscopy and X-Ray Microanalysis*. 2018.
[52] K. Yase, *Transmission Electron Microscopy*, vol. 43, no. 2. 1994.

[53] C. X-rays, “Analytical Electron Microscopy for Materials Science,” *Mater. Today*, vol. 6, no. 1, p. 38, 2003, doi: 10.1016/s1369-7021(03)00133-0.
[54] Meyers, *Mechanical Behaviour of Materials*, 2nd ed. Cambridge University Press, 2009.
[55] “Baker, Hugh Okamoto, Hiroaki. (1992). ASM Handbook, Volume 03 - Alloy Phase Diagrams. ASM International. Retrieved from https://app.knovel.com/hotlink/toc/id:kpASMHVAP1/asm-handbook-volume-03/asm-handbook-volume-03,” .
[56] Bruker, “X-Ray Energies of the Elements,” *Eds*. [Online]. Available: https://www.bruker.com/fileadmin/user_upload/8-PDF-Docs/X-rayDiffraction_ElementalAnalysis/HH-XRF/Misc/Periodic_Table_and_X-ray_Energies.pdf.
[57] A. S. Darmawan *et al.*, “The influences of ion implantation doses to commercially pure titanium surface hardness,” *Simp. Nas. RAPI XI FT UMS*, no. December, 2012.

9 Appendices

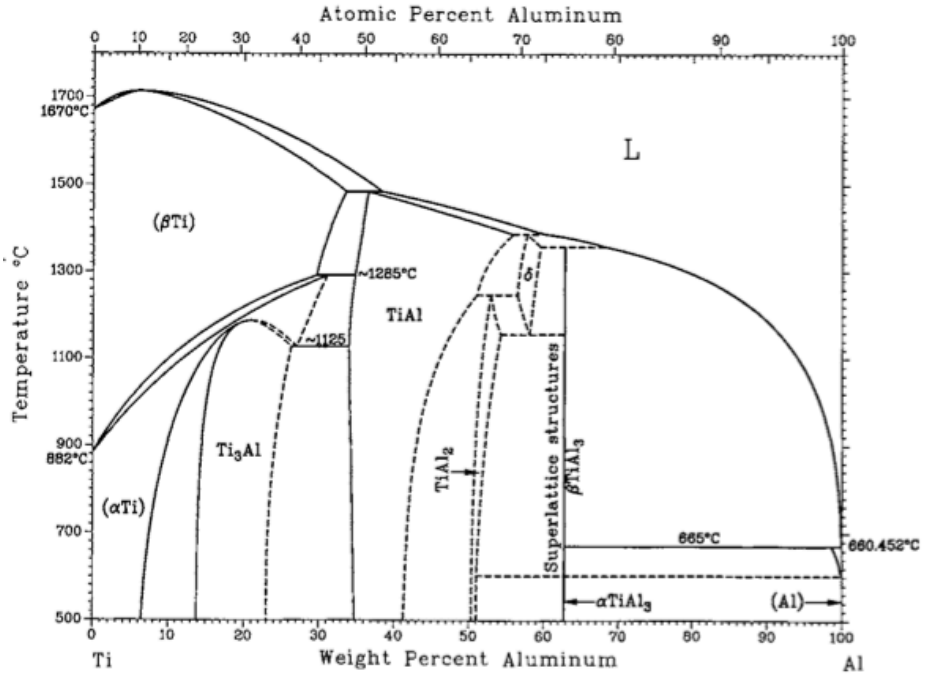

Appendix 1: Titanium aluminum phase diagram. [55]

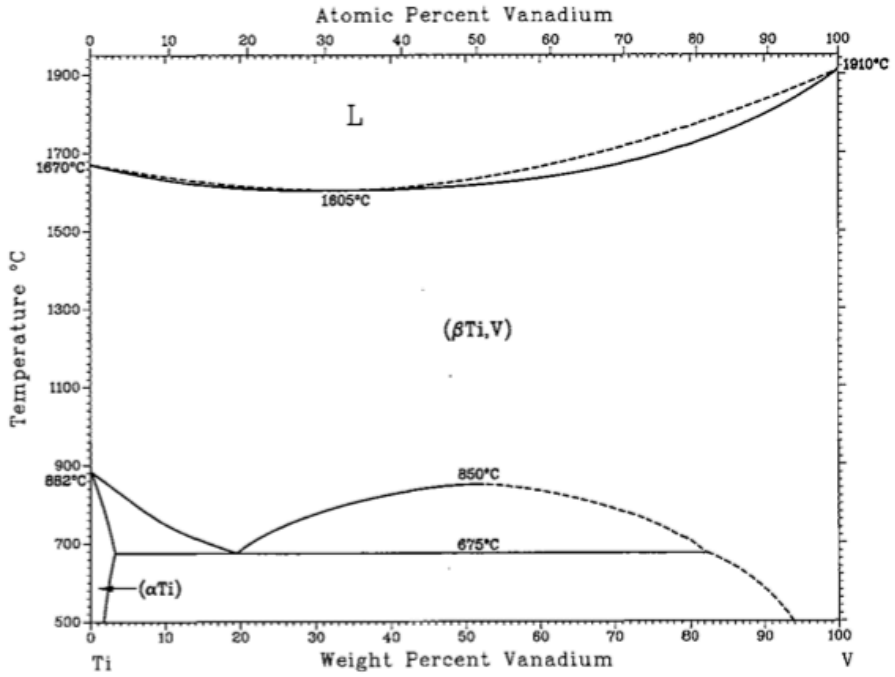

Appendix 2: Titanium vanadium phase diagram. [55]

Appendix 3: Characteristic X-ray energies for a few selected elements. [56]

	$K_{\alpha 1}$ [keV]	$K_{\beta 1}$ [keV]	L_{a1} [keV]	$L_{\beta 1}$ [keV]
N	0.392			
O	0.525			
Al	1.486	1.557		
Si	1.740	1.837		
Ti	4.512	4.933	0.452	0.458
V	4.953	5.428	0.510	0.518
Fe	6.405	7.059	0.705	0.718

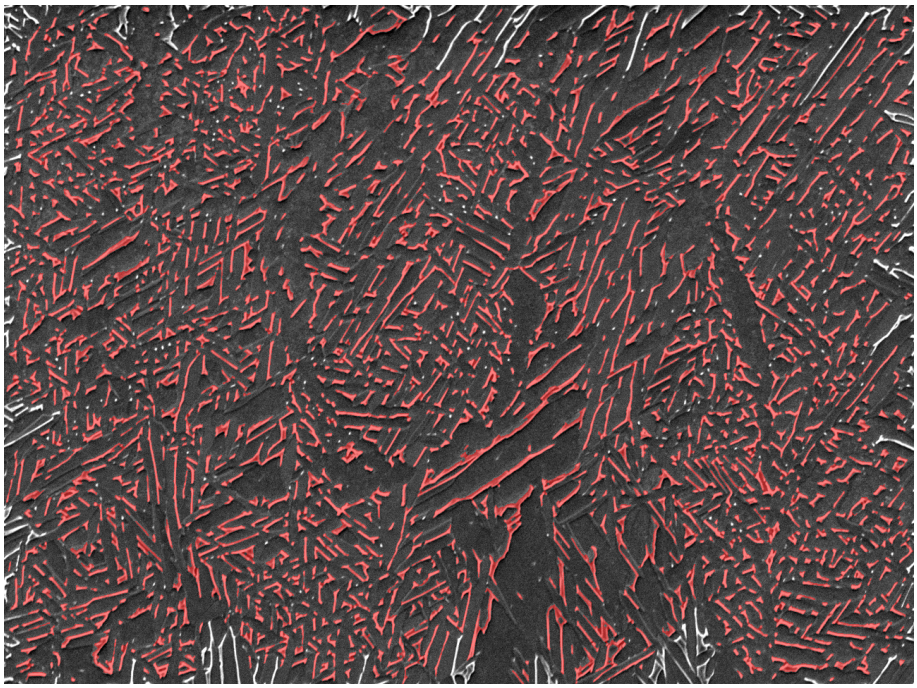

Appendix 4: Result of the segmentation algorithm in Mipar. The red color indicates what the software counts as β-Ti and the white presents the excluded features. The black area represents α-Ti.

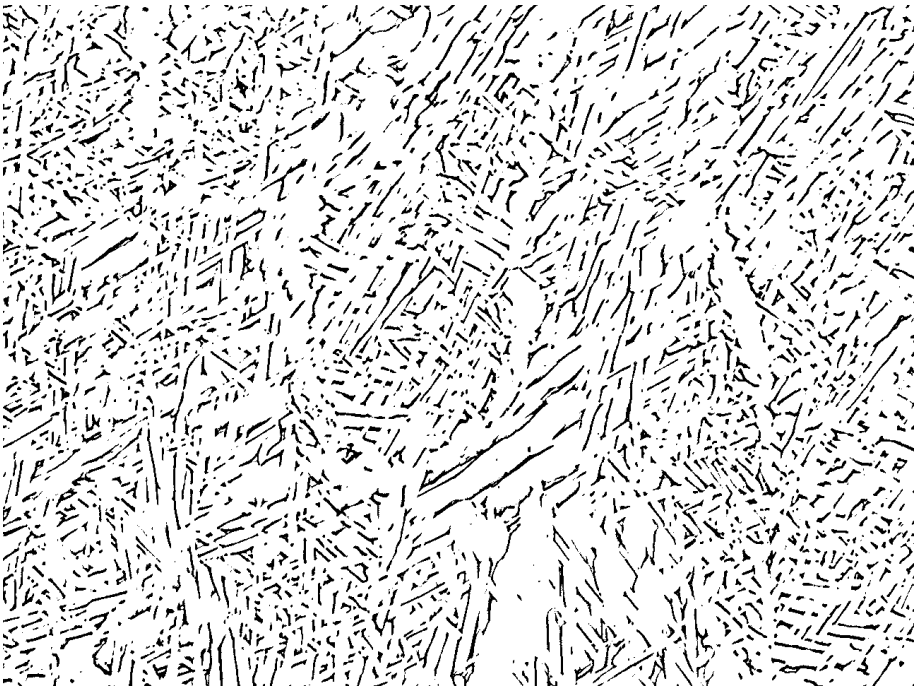

Appendix 5: Thresholding of microstructure by ImageJ to obtain the phase fraction.

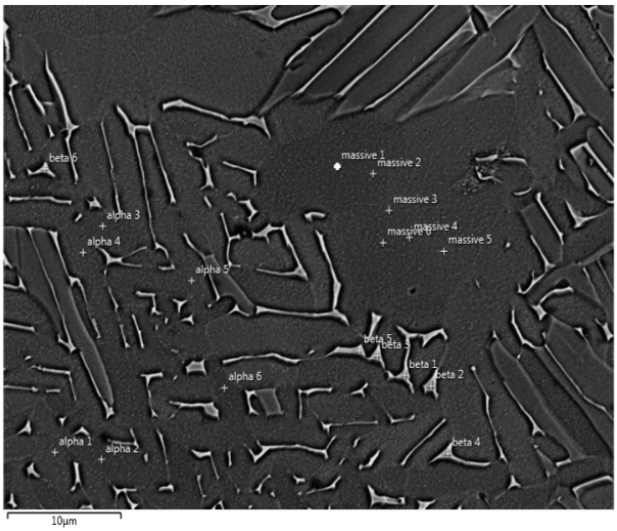

Appendix 6: Site for EDS point analysis of massive phase and location of every recorded spectrum.

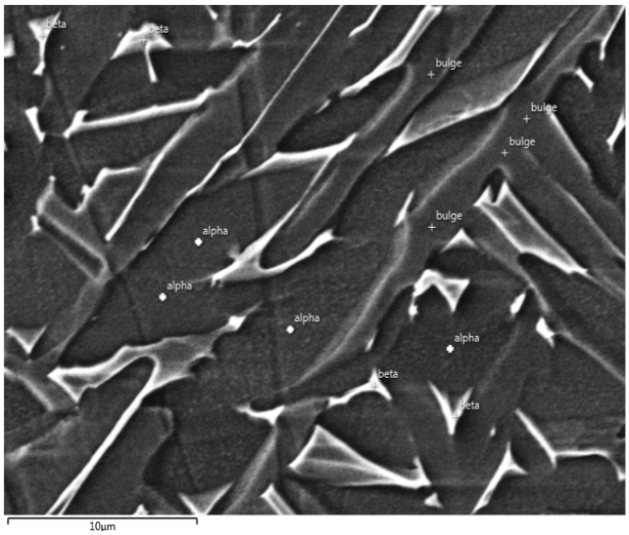

Appendix 7: Site for EDS point analysis of bulges and location of every recorded spectrum.

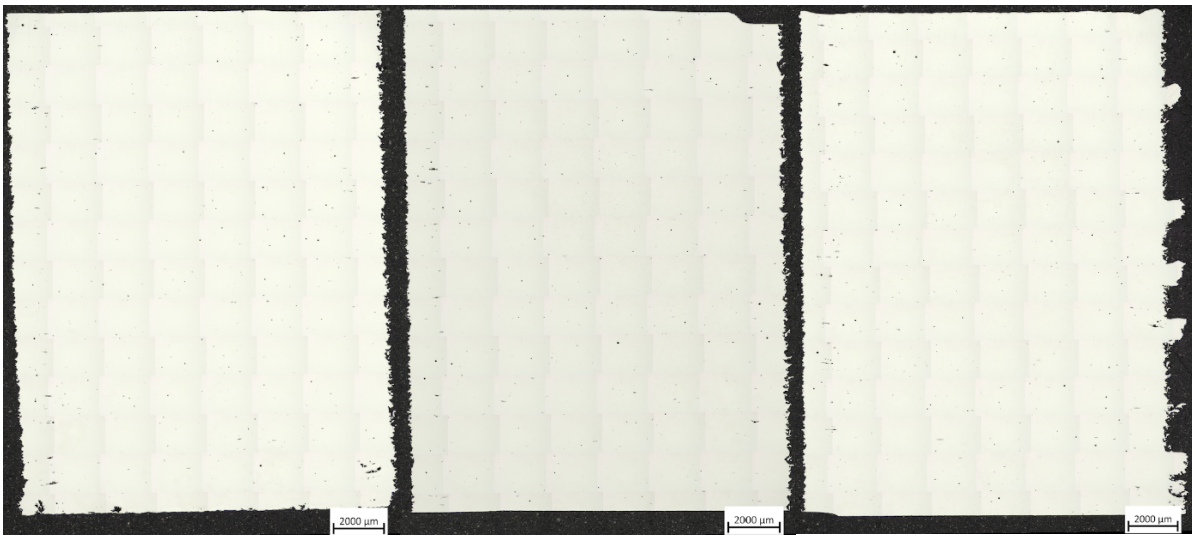

Appendix 8: Stitched OM image of polished surface at 50 × magnification for A3K1 where the building height is increasing from left to right.

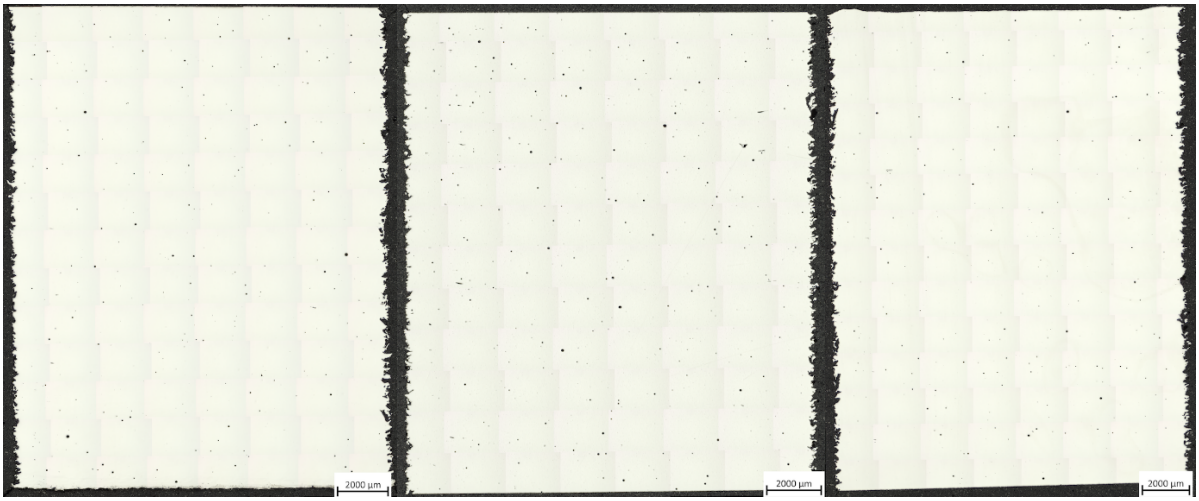

Appendix 9: Stitched OM image of polished surface at 50 × magnification for A3bK1 where the building height is increasing from left to right.

Appendix 10: Stitched OM image of polished surface at 50 × magnification for A3bK85 where the building height is increasing from left to right.